Distribution and pathways of dissolved methane (CH_4) in the water column of the East Greenland shelf

Master-Thesis

im Masterstudiengang (M.Sc.) Geowissenschaften

der Mathematisch-Naturwissenschaftlichen Fakultät

der Christian-Albrechts-Universität zu Kiel

in Zusammenarbeit mit dem

GEOMAR – Helmholtz-Zentrum für Ozeanforschung Kiel

Forschungsabteilung: Marine Biogeochemie

Forschungseinheit: Chemische Ozeanographie

Vorgelegt von:	Daniel Bastian
Matrikelnummer:	1018959
Erstgutachter:	Prof. Dr. Hermann W. Bange
Zweitgutachter:	Dr. Damian L. Arévalo-Martínez

Kiel, im Mai 2021

Table of Contents

List of Figures:

List of Tables:

1 Abstract

Methane (CH_4) is the second most relevant greenhouse gas on Earth. Polar and subpolar regions are highly sensitive to climate change and the increasing melting rates of seasonal and (multi-) annual ice are projected to have severe impacts on their marine ecosystems. However, the knowledge about the distribution and pathways of dissolved CH_4 and how it is affected by melting in these regions is sparse - or particularly for the East Greenland shelf (EGS), non-existent. To shed light on the CH_4 cycling on the EGS, extensive sampling was conducted throughout the area during the melting season in July 2019 onboard the research vessel MARIA S. MERIAN during the cruise MSM85. Enhanced CH_4 saturations (max.: 173 %) were observed in surface waters in connection with meltwater. This resulted in pronounced gradients between the near-shore area and the open ocean. Meltwater associated with amplified CH_4 was characterized by low oxygen uptake, aerated conditions, low Chl-α and N-limitation which reflect the post-bloom phase of water masses influenced by seasonal ice coverage. The surface layer was near equilibrium with the atmosphere for the entire shelf with respect to dissolved CH_4 and the overall mean sea-air CH_4 flux of the EGS was -0.11 ±1.5 µmol/m² s (range: -3.8 – 3.12 µmol/m² s). Therefore, at the time of sampling, the EGS acted neither as a significant sink nor source for atmospheric CH_4, in contrast to most of the global coastal regions where CH_4 is supersaturated with respect to atmospheric equilibrium. Enhanced CH_4 concentrations at depth were mainly found on the shelf (max.: 66.85 nmol/kg) in association with Arctic-derived water of the East Greenland Current (EGC). Open ocean stations were largely undersaturated for CH_4 while coastal locations were near equilibrium or supersaturated, suggesting that the projected rising melting rates could potentially turn the site into a source for atmospheric CH_4.

2 Kurzfassung

Methan (CH_4) ist das zweitwichtigste Treibhausgas auf der Erde. Die polaren und subpolaren Regionen reagieren hochsensibel auf klimatische Veränderungen, sodass aufgrund der steigenden Schmelzraten von saisonalem sowie (mehr-)jährigem Eis massive Auswirkungen auf das marine Ökosystem prognostiziert wurden. Jedoch ist der Wissensstand über die Verteilung und Wege von gelöstem CH_4 als auch seine Einflüsse durch Schmelzwasser dürftig - im Falle des Ostgrönlandschelfs (EGS) sogar nicht existent. Um Aufschluss über den CH_4-Kreislauf der Wassersäule des Ostgrönlandschelfs zu geben, wurden dort während der Schmelzsaison im Juli 2019 auf der Expedition MSM85 an Bord des Forschungsschiffes MARIA S. MERIAN eine extensive Beprobung durchgeführt. Erhöhte CH_4 Sättigungen (max.: 173 %) konnten in Verbindung mit schmelzwasser-beeinflusstem Oberflächenwasser festgestellt werden, die in ausgeprägten Gradienten zwischen den küstennahen Gebieten und dem offenen Ozean resultierten. Schmelzwassereinflüsse in CH_4-angereicherten Wassermassen waren durch niedrigen Sauerstoffverbrauch, belüftete Verhältnisse, niedrige Chl-α-Werte sowie Stickstofflimitierung charakterisiert und spiegeln die Post-Blütenphase von Wassermassen, die durch saisonale Eisbedeckung beeinflusst sind, wider. Für den gesamten Schelf befinden sich die CH_4-Werte in der Deckschicht des Ozeans nahe dem Equilibrium mit der Atmosphäre; insgesamt liegt der Ozean-Atmosphären-Fluss von CH_4 auf dem Ostgrönlandschelf bei -0,11 ±1.5 µmol/m^2 s (Wertebereich: -3,8 – 3,12 µmol/m^2 s). Demzufolge stellt der Ostgrönlandschelf zur Zeit der Beprobung weder eine Quelle noch eine Senke für atmosphärisches CH_4 dar und verhält sich somit gegensätzlich zu den meisten anderen Küstenregionen der Erde, in denen gelöstes CH_4 in Bezug auf das atmosphärische Equilibrium übersättigt ist. Erhöhte CH_4 Konzentrationen über die Tiefe werden hauptsächlich (max.: 66,85 nmol/kg) mit arktischen Wassermassen des Ostgrönlandstroms auf dem Schelf assoziiert. Stationen auf dem offenen Ozean sind hinsichtlich CH_4 überwiegend untersättigt, während küstennahe Standorte nahe dem Equilibrium oder übersättigt sind. Die prognostizierten steigenden Schmelzraten könnten das Untersuchungsgebiet somit in eine potenzielle Quelle für atmosphärische CH_4 umformen.

3 Introduction

Methane (CH_4) is the second most important climate-relevant greenhouse gas following carbon dioxide (CO_2) (Solomon et al., 2007). The radiative forcing per molecule is 28-times higher for CH_4 compared to CO_2 (Intergovernmental Panel on Climate Change, 2014c) while it has a comparably shorter atmospheric residence time of 10.5 ±1.8 years (Mayer et al., 1982) compared to other greenhouse gases, e.g. nitrous oxide (N_2O) with a lifetime of 131 years (Intergovernmental Panel on Climate Change, 2014c). Due to its small quantities in the atmosphere, it is typically referred to as a trace gas (units in parts per billion, ppb). However, CH_4 currently contributes to around 20 % of the total radiative climate forcing for all greenhouse gases (Etminan et al., 2016; Weber et al., 2019).

3.1 Greenhouse Gases and Climate Change

The global climate change attributed to greenhouse gases is prognosticated to be accompanied by a wide variety of consequences for the future (Intergovernmental Panel on Climate Change, 2014b; Malhi et al., 2020). All these consequences also have indirect and direct implications for humankind itself which will be manifested in drastic changes in living conditions such as a reduction of habitable space and insufficient global food production as well as challenges in the health, economy, and security sector (Wilbanks et al., 2007).

The Earth's polar and subpolar regions are highly sensitive to climate change (Solomon et al., 2007). This is manifested in a phenomenon called Polar Amplification which describes the effect that polar regions generally undergo larger changes in temperatures compared to the planetary average (Lee, 2014). For example, from 1970 to 2008 the Arctic warmed at a 2 – 3 times higher pace than the global-mean warming (see fig. 1, Chylek et al., 2009; GISTEMP-Team, 2021; Lenssen et al., 2019). Several factors control this:

(1) The efficiency of ocean circulation by coupling the Antarctic, Equator, and the Arctic through energy exchange (Chylek et al., 2010),

(2) atmospheric heat exchange between the Equator and the Arctic (Lee et al., 2011),

(3) a reduction of albedo following a reduction in sea ice extent (Hansen et al., 1997; Pistone et al., 2019; Singh et al., 2011).

Ice and snow generally display high albedo, reflecting up to 90 % of the incoming solar energy (Drewry, 1986) thus also strongly constricting associated heat exchange with the surface. Conversely, the ice-free surface of the ocean only reflects ~ 6 % of the incoming sunlight.

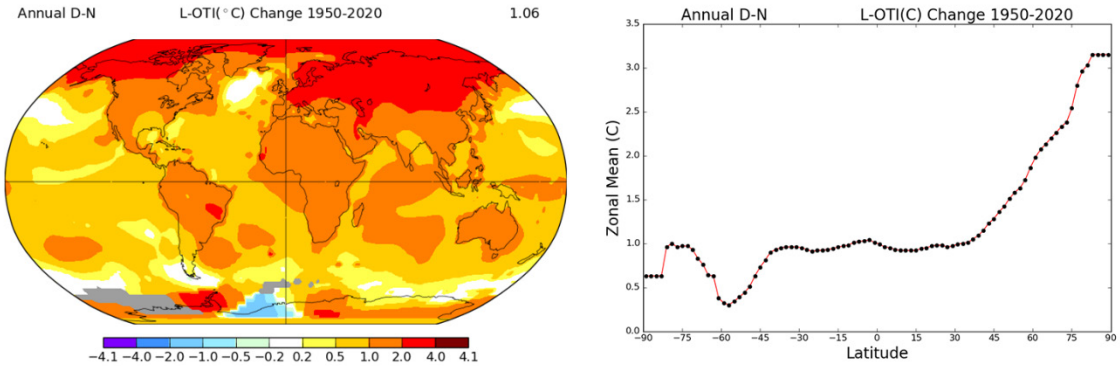

Figure 1: Left: Annual trend of global surface temperature change [°C] from 1950 to 2020. The number at the top right-hand corner is the estimated global mean. **Note**: Gray areas signify missing data. **Right**: Zonal mean surface temperature change [°C] per latitude (°) from 1950 to 2020 (GISTEMP-Team, 2021; Lenssen et al., 2019).

Consequently, albedo and ice are intertwined by a positive feedback loop. When sea-ice extent is high, albedo is high and thus the surface of the polar region experiences less warming and reciprocally low sea ice extent is accompanied by low albedo and amplified surface heating due to higher absorbance of solar energy. Dai et al. (2019) suggest a direct link between Arctic Amplification and sea ice loss.

Already, the retreat of Arctic sea ice extent has been uniformly reported with an overall decrease of -51.1 ±4.1x10³ km²/yr in sea ice extent for the Northern Hemisphere which equals to -4.1 ±0.3 %/10 yrs. For the Greenland Sea, this effect is even more pronounced with a loss of sea ice extent of -9.2 ±1.6 %/10 yrs (see fig. 2; Cavalieri and Parkinson, 2012; Serreze and Stroeve, 2015). Furthermore, Arctic multiyear ice cover experienced a decadal decline of -15.1 % from 1979 to 2011 (Comiso, 2012).

The loss of sea ice introduces a variety of impacts on the Arctic ecosystem. An increase of fresh, buoyant meltwater from ice melt intensifies stratification in the surface layer which in turn inhibits vertical mixing and inherent nutrient supply from the deeper water column. On the other hand, additional nutrients are introduced to the surface layer and the increased light incidence on the now exposed water surface induces short-lived but intense blooms. Furthermore, the habitat for ice algae decreases, ocean circulations are projected to change which would introduce species from lower latitudes and primary production is bound to alter

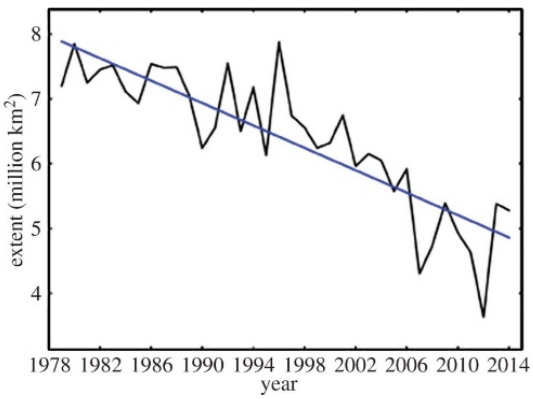

Figure 2: Average September sea ice extent for 1979-2014 and linear least-squares fit based on satellite passive microwave data using the NASA team algorithm (Serreze and Stroeve, 2015; adapted from NSIDC).

among many other impacts (Moline et al., 2008; Qu, 2015; Rahmstorf et al., 2015; Smetacek and Nicol, 2005; Stouffer et al., 2006; Swingedouw et al., 2013).

Another significant contributor to freshwater fluxes to the circumambient ocean of Greenland is the progressing melt of the Greenland Ice Sheet (GrIS) with an annual ice loss of -239 ±23 km³ (from a total of ~ $2.5x10^6$ km³) which is predominantly draining to the East Greenland shelf (EGS)(see fig. 3; Bamber et al., 2012; Chen et al., 2006; Sasgen et al., 2012). Land-derived meltwater has been proposed to alter fjords, near-shore, and shelf areas with regards to the carbon cycle with indirect ecological consequences such as downstream fertilization and stratification or direct consequences such as the release of CO_2 and CH_4 (Oliver et al., 2018; Wadham et al., 2019) as well as severe shifts in biogeochemistry (Hendry et al., 2019). Additionally, positive feedback between sea ice loss and GrIS melt has been proposed (Liu et al., 2016).

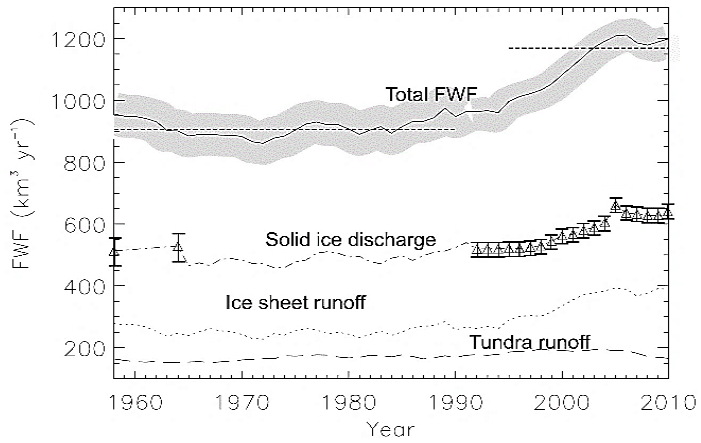

Figure 3: Ice sheet and tundra runoff, discharge, and total freshwater fluxes (FWF) [km³/yr] from Greenland for 1958-2010. The triangles indicate the dates where discharge data were available, and the error bars are the 1-sigma uncertainty discharge. Uncertainty in tundra and ice sheet runoff is 10 and 20 %, respectively (Bamber et al., 2012).

Even though greenhouse gas emissions are the root of all of these ramifications, knowledge about greenhouse gas cycling and inherent changes induced by climate change in the polar and subpolar regions is sparse. Parmentier et al. (2013) display a relationship between sea ice extent, temperature anomalies, and increased CH_4 fluxes to the atmosphere and link it to an increase in sources such as wetlands, subsea permafrost thaw, and release from surface waters (see fig. 4). Furthermore, Rutgers van der Loeff et al. (2014) propose that sea ice extent has a large impact on the gas transfer of greenhouse gases and other biochemically important gases between the sea and atmosphere which is manifested in gas transfer velocities that are 5 - 22 times higher on an ice-free water surface compared to an ice-covered surface, implying that gas transfer velocities are projected to rapidly increase.

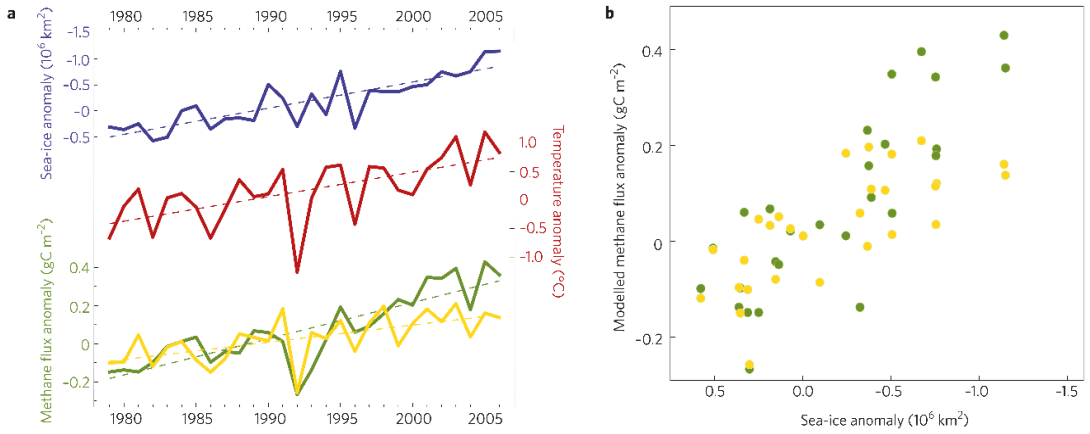

Figure 4: **a**: Time series for the period of June to October from 1979 to 2006, showing: average anomalies in sea-ice extent (blue, plotted inverted), averaged surface-temperature anomalies (red), and total methane anomalies from the LPJ-GUESS WHyMe (green) and TEM6 (yellow). Model runs: 50. **b:** Anomalies in sea-ice extent (inverted) plotted against the modeled methane anomalies. Sea-ice extent data is obtained from ref. 101, and temperature from the CRU TS 3.0 dataset102. Anomalies are calculated from the average over the baseline period 1979–2000. The correlation between the de-trended time series of sea ice and the two methane models is significant at a 95 % level (r = -0.45 and -0.45, p = 0.02 and 0.01 for LPJ and TEM6 respectively) (Parmentier et al., 2013).

Models for greenhouse gas budgets and fluxes are crucial for conceptual strategies to mitigate emissions and impacts on the environment. However, the greatest hurdle in constructing reliable and precise models is the lack of knowledge about the distribution and concentration of these gases, especially for oceanic budgets (Battaglia and Joos, 2018; Saunois et al., 2020; Weber et al., 2019; Wilson et al., 2018; Yang et al., 2020), though recent organizational efforts have been undertaken to challenge this (Bange et al., 2019; Kock and Bange, 2015). This knowledge gap arises from spatial disparities in sampling, temporal biases as well as general undersampling. Particular areas of this circumstance are the polar and subpolar regions where surveys on oceanic CH_4 distributions are sparse or for the subpolar EGS non-existent (MEMENTO database; see fig. 5, Kock and Bange, 2015). Here, sampling biases largely arise from unfavorable working conditions (e.g., ice coverage) which were also encountered during this study as well as lack of sufficient resources to enter the region.

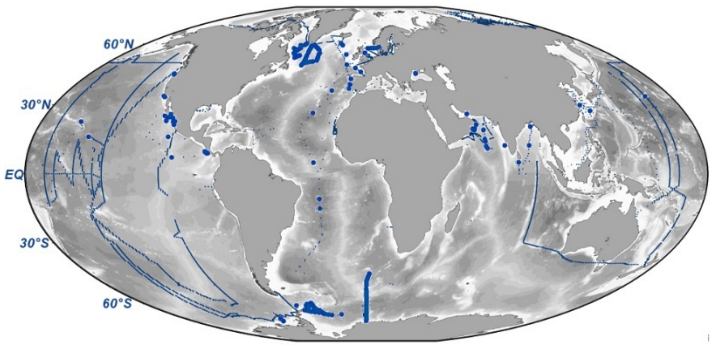

Figure 5: Location of surface and depth profile measurements of CH_4 included in MEMENTO (2014); large dots indicate depth profiles.

3.2 History of Atmospheric CH_4

During the late Quaternary (< 800 kyrs BP), which was largely influenced by alternating glacial and interglacial periods, the atmospheric mixing ratio of CH_4 ranged between 350 and 700 ppb as shown in records of trapped air bubbles in ice cores from Antarctica. Fluctuations of CH_4 during this time were strictly bound to the Milankovitch cycle (see fig. 6). Low atmospheric CH_4 concentrations (~350 ppb) were recorded during glacials and high atmospheric CH_4 concentrations (600 – 700 ppb) were recorded during interglacials (Loulergue et al., 2008). This is most likely due to a reduction of emission sources throughout the coverage of ice shields during glaciation phases (Hopcroft et al., 2017). During the past 650,000 years BP, atmospheric CH_4 concentrations did not exceed 773 ±15 ppb until the time of industrialization in 1750 AD (Spahni et al., 2005), however, during the late Holocene (< 5 kyrs BP) atmospheric CH_4 already started to steadily increase. It is hypothesized that this could be due to a decrease in CH_4 sinks (Reeburgh, 2007) or changes in tropical wetland emissions (Singarayer et al., 2011; Sowers, 2010). Changes in the atmospheric CH_4 isotopic composition also suggest that the gradual release of methane clathrates in higher latitudes could be the source for increasing mixing ratios in the late Holocene (Sowers, 2010). Additionally, Ruddiman (2003) points to early anthropogenic influences and affiliates the start of rice irrigation 5,000 years BP to the rise in atmospheric CH_4.

Between the years 0 to 1750 AD the atmospheric CH_4 concentration grew from 640 - 740 ppb by 100 ppb which is most likely attributed to early anthropogenic emissions (MacFarling Meure et al., 2006). Since the beginning of the Industrial Era, however, the atmospheric mixing ratio of CH_4 increased 2.5-fold from 722 ppb to 1,803 ppb in 2011 AD (Intergovernmental Panel on Climate Change, 2014a). This is an increase of growth of 4.16 ppb/yr in the Industrial Era

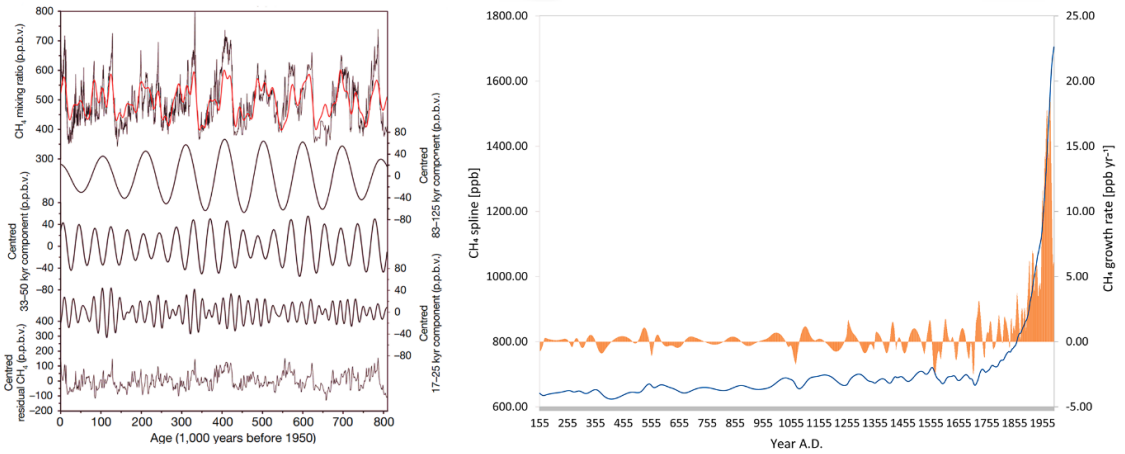

Figure 6: Left: Orbital components and residuals [expressed as ppb] of CH_4 record over the past 800 kyrs. The **red** line combines the three periodicities. Right: In **blue** the revised record of atmospheric CH_4 [spline, in ppb] and in **orange** its growth rate [in ppb/yr] over the last 2 kyrs from Law Dome, Antarctica (Loulergue et al., 2008; Rubino et al., 2018).

compared to 0.06 ppb/yr between the year 0 to 1750 AD. More recently, the growth rate of CH_4 has steadily declined from 1985 to 2008 AD from ca. 14 ppb/yr to 3 ppb/yr. This is debatably ascribed to a reduction in active anthropogenic emitters such as coal mines, gas industries, and/or animal husbandry, especially in countries of the former Soviet Union as well as to variations in the emissions of wetlands and fluctuations of hydroxyl-radicals which are a sink for CH_4 (Chen and Prinn, 2006; Dlugokencky et al., 2003; Intergovernmental Panel on Climate Change, 2014a; Rubino et al., 2019; Savolainen et al., 2009; Simpson et al., 2012). Nevertheless, following the near steady-state of atmospheric CH_4 in the early 2000s, since 2008 the growth rate increased to levels prior to 1985 (Nisbet et al., 2019; Saunois et al., 2020) resulting in a current record-high atmospheric CH_4 mixing ratio of 1892.3 ppb (as of December 2020, see fig. 7; (Dlugokencky, 2021). Furthermore, the current atmospheric mixing ratio of CH_4 is projected to double by 2100 (Meinshausen et al., 2011).

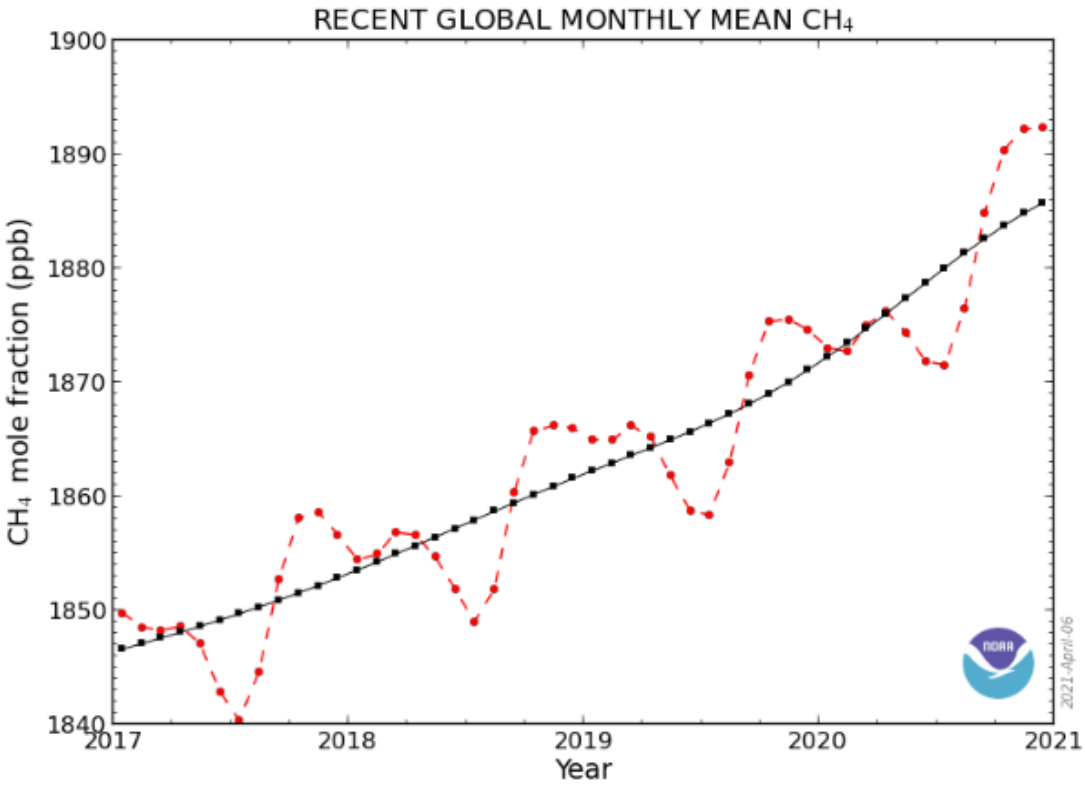

Figure 7: Recent global monthly mean CH_4 [in ppb] in the atmosphere from 2017-2021. **Red** dashed line and circles are globally averaged monthly mean values centered on the middle of each month. The **black** line and squares show the long-term trend where average seasonal cycle has been removed (Dlugokencky, 2021).

3.3 CH_4 Production, Consumption, Transport, and Storage

CH_4 can be formed under oxic and anoxic environments and is produced by biotic as well as abiotic processes.

The latter includes geological processes such as the formation of fossil gas which is released from kerogens by catagenesis during diagenesis of sediments followed by subsequent expulsion, migration, and trapping in reservoirs (Killops and Killops, 2004). Furthermore, CH_4 (and H^+) production has been linked to hydration and serpentinization of exhumed ultramafic rocks at the ocean-seafloor interface and associated hydrothermal systems (e.g. at mid-oceanic ridges or oceanic core complexes; Holm et al. 2015; Klein et al. 2019) through Fischer-Tropsch-type (FTT) synthesis (Huang et al., 2016) at high temperatures (> 200 °C; Johnson et al. 2015). Significant concentrations of CH_4 were found in the form of plumes in the near vicinity of divergent boundaries and active fracture zones which have been attributed to rock-water reactions (Charlou et al., 1998). However, these processes have yet not been successfully replicated experimentally (McCollom and Donaldson, 2016). Moreover, Vitale Brovarone et al. (2020) suggest that deep serpentinization (> 80 km) and associated CH_4 genesis and migration may provide energy for deep sub-seafloor communities. It has been proposed that gas hydrate reservoirs which will be addressed in the following are partly fed by abiotically generated CH_4 from ultraslow-spreading ridges. This process was observed at the Fram Strait (Johnson et al., 2015) which is also subject to this work. Nonetheless, gas hydrate deposits are also fed by other biotic and abiotic sources (MacDonald et al., 2003; Pape et al., 2011).

Gas hydrates are deposits of CH_4 (among other gases) which are bound in the form of cage-like crystalline structures called clathrates at or below the seafloor (Majorowicz and Hannigan, 2000). In the aquatic milieu, these are only stable under a specifically low temperature and high-pressure range which is called the Gas Hydrate Stability Zone (GHSZ) (Wallmann et al., 2012). Wood and Jung (2008) estimated the thickness of the GHSZ at the East Greenland shelf between 150 – 450 m. Lee and Holder (2001) estimated the global CH_4 hydrate reserves at $10{,}000 \times 10^9$ tons which represent 53 % of all fossil fuel reserves on Earth. Numerous findings of gas hydrates have been reported through direct and inferred through indirect measurements for the polar and subpolar Fram Strait, Svalbard, and Barents Sea region (Johnson et al., 2015; Klitzke et al., 2016; Pape et al., 2011; Wallmann et al., 2012, 2018), for the northwest shelf margin (Cox et al., 2021) and the eastern shelf-slope of Greenland (Geissler et al., 2014) as well as on the central-western shelf of Greenland (Mikkelsen et al., 2012). The Arctic geologic CH_4 reservoir with a carbon store of over 1,200 Pg is large when compared with the global atmospheric CH_4 pool of around 5 Pg. Due to this, Earth's climate is sensitive to the escape of even a small fraction of CH_4 to the atmosphere (Walter Anthony et al., 2012).

Moreover, significant amounts of CH_4 are released by lithospheric degassing (e.g. volcanic eruptions) (Etiope et al., 2007; Saunois et al., 2020) and upon combustion of biomass (15 – 21 $TgCH_4$/yr; Saunois et al., 2020).

On the other hand, biological processes are working on much shorter timespans, though play an equally important role compared to geological processes. Naturally, CH_4 is biotically produced via methanogenesis by microbes. Archaea and some bacteria are the only organisms known to produce CH_4 through metabolism (methanogens).

Methanogenesis describes the process of cellular respiration which mostly occurs under anoxic conditions when terminal electron acceptors such as iron (Fe(III)), manganese, nitrate, or sulfate are scarce.

On the opposite, when these substances are abundant, methanogenesis is easily outcompeted by other anaerobic respiration types such as denitrification and sulfate-reduction which have significantly higher energy yields regarding their uptake of cellular carbon for biomass accumulation. Additionally, sulfate-reducers are very effective in their uptake of H_2 and acetate and thus can maintain these at concentrations too low for methanogens to function (Reeburgh, 2007). During methanogenesis, substrates are converted to CH_4 during chemiosmosis across the cytoplasmic membrane and subsequent ATP synthesis for cellular energy conservation. The substrates are either H_2 + CO_2 (or formate) (hydrogenotrophs) which is most common and where CO_2 is sequentially reduced to CH_4 while H_2 acts as the electron donor, as well as methylated compounds (methylotrophs) and acetate (acetotrophs) (Rother, 2010):

$$CO_2 + 4H_2 \rightarrow CH_4 + 2H_2O$$

$$CH_3COOH \rightarrow CH_4 + CO_2$$

Typical aquatic domains where methanogenesis is abundant are anoxic sediments (Barnes and Goldberg, 1976). These develop when dissolved oxygen (DO) in sedimentary porewater is depleted due to aerobic respiration and associated remineralization of organic matter which is mainly composed of detritus falling from the upper layers of the water column. When other substrates with higher energy yields (e.g., nitrate and sulfate) are subsequently depleted, CH_4 production rates typically arise. CH_4 saturated porewater is then expelled into the water column and eventually into the atmosphere at the sea-air interface through diffusion.

Another prominent production zone for CH_4 in the water column is the surface mixed layer. While in some surface layers oxygen levels are entirely depleted resulting in anoxia which then mediates anaerobic methanogenesis, the vast majority of the ocean water column is well oxygenated. However, even in oxygen-rich waters, CH_4 supersaturation has been observed. This seemingly contradictory phenomenon is the so-called “ocean methane paradox” (Reeburgh, 2007). A wide variety of processes have been proposed to explain this circumstance. Sinking or suspended

organic aggregates (e.g. fecal pellets) might serve as anoxic micro-niches where methanogenesis could be mediated (Sasakawa et al., 2008). Additionally, the digestive tracts of zooplankton have been proposed to serve as mediators (de Angelis and Lee, 1994; Schmale et al., 2018).

Additionally, methanogenesis can occur directly in the water column, especially in eutrophicated water bodies that reach succeeding anoxia. However, CH_4 production can be inhibited by the presence of sulfate which is ubiquitous in the global marine environment (Lovley et al., 1982). Nevertheless, the co-existence of methanogenesis and sulfate reduction has been reported for sediments (Sela-Adler et al., 2017).

However, aerobic pathways during microbial cycling of dissolved organic matter (DOM) for CH_4 have been suggested as well. Florez-Leiva et al. (2013) infer a relationship between the presence of dimethylsulfide (DMS) and CH_4 in the mixed layer. DMS degradation by methanogens has been reported for anoxic freshwater sediments in sulfate-deprived conditions where methanogens were dominantly degrading DMS and in sulfate-enriched conditions where methanogens and sulfate-reducers competed (Lomans et al., 1999). A relationship between methanogenesis during austral summer phytoplankton bloom and Dimethylsulfoniopropionate (DMSP) – a DMS (and methanethiol) precursor molecule – has been described for the oxygenated mixed layer of the Arctic shelf. Here, DMSP could act as a potential substrate for methylotrophic methanogenesis (Damm et al., 2008). Furthermore, DMS production by algae has been linked to sea ice coverage with subsequent release of DMS during melt season (Levasseur et al., 1994; Tison et al., 2010; Trevena and Jones, 2006). Damm et al. (2010) suggest that DMSP is used as a carbon source for methanogens. Another aerobic pathway is the degradation of methyl phosphonate (MPn). Under phosphate-limiting conditions, MPn is degraded during phosphorous assimilation. CH_4 is released as a byproduct during degradation. This process seems to be enhanced in nitrogen-fixation-enhanced marine habitats (Karl et al., 2008). The main way of transport for the processes mentioned above is diffusion either in the water column or at the sea-air interface into the atmosphere. The global diffusive CH_4 flux to the atmosphere was estimated by Weber et al. (2019) to be 2 – 6 $TgCH_4/yr$.

Aside from diffusion, another pathway for CH_4 from the sediments to the water column (and subsequently partially to the atmosphere) is ebullition (Weber et al., 2019). It describes the process of expulsion of gaseous bubbles from a porous medium (e.g. cold seeps (Mau et al., 2020) or mud volcanos (Feseker et al., 2014)) into the water column where it rises to the atmosphere due to buoyancy differences to the surrounding water. Ebullition is the most effective way to transport CH_4 from aquatic sediments to the atmosphere (DelSontro et al., 2015). During their ascent, the gas inside the bubbles is dissolved into the water column which then causes the bubbles' hydrostatic pressure to decrease and the size of the bubble to expand (DelSontro et al., 2015). This creates an even larger surface area for dissolution which in turn increases even more.

Additionally, bubbles often merge during their ascent which is most prominent at sites with high expulsion rates. This shows that CH_4 transfer through ebullition is largely dependent on bubble size and the intensity of bubble release from the seafloor. As a result, ebullition influence on the atmosphere is exclusively restricted to shallow waters as even the largest bubbles rise to an altitude of a maximum of 100 m and thus in the marine environment it is confined to the continental shelf area (Weber et al., 2019). Weber et al. (2019) used machine-learning models to estimate the global oceanic CH_4 emissions at 6 – 12 $TgCH_4$/yr and conclude that the global flux is dominated by shallow near-shore environments where short CH_4 travel distances outweigh oxidation rates.

The dominant sink for CH_4 is the atmosphere where > 80 % of CH_4 (440 ±52 $TgCH_4$/yr) is converted by chemical reaction with hydroxyl radicals in the troposphere (Prather et al., 2012; Worthy et al., 2015):

$$OH^- + CH_4 \rightarrow H_2O + CH_3^+$$

$$CH_3^+ + O_2 \rightarrow CH_3O_2$$

CH_4 may also be removed near the surface over oceans by chemically reactive chlorine (25 ±12 $TgCH_4$/yr) or uptake by CH_4-consuming bacteria in dry soils (25 – 40 $TgCH_4$/yr) (Worthy et al., 2015).

On the other hand, 90 % of dissolved oceanic CH_4 produced in marine sediments is consumed by anaerobic oxidation either in the sediments or the water column (Reeburgh, 2007). This process is commonly referred to as Anaerobic Oxidation of Methane (AOM) and is a form of oxidation that is mediated by various archaea as well as sulfate-reducing bacteria:

$$CH_4 + SO_4^{2-} \rightarrow HCO_3^- + HS^- + H_2O$$

It was also reported to be coupled to nitrate and nitrite reduction (Haroon et al., 2013).

Furthermore, CH_4 in aerated sediments, as well as the water column, may be oxidized by aerobic bacteria and is commonly called the Aerobic Oxidation of Methane (Hanson and Hanson, 1996; Murrell, 2010):

$$CH_4 + 2O_2 \rightarrow CO_2 + 2H_2O$$

The rate of oxidation depends on the microbial community as well as the amount of dissolved CH_4 present (Murrell, 2010).

3.4 Oceanic CH_4 in the Polar and Subpolar Latitudes

Reports of dissolved CH_4 in the western Arctic shelf and open ocean (Canada Basin, Chukchi Sea, and Bering Strait) show supersaturation with respect to the atmospheric equilibrium and concentrations of up to 10.3 nmol/kg in the surface layer of the shelf as well as anomalously high concentrations of up to 55.9 nmol/kg at the bottom layer of the shelf (Kudo et al., 2018). Shakhova et al. (2005) discovered that the average concentration of dissolved CH_4 in the surface layer was 10.5 nM (range: 2.1 – 28.2 nM) and 13.5 nM (maximum: 110 nM) in September 2003 and 2004, respectively, for the East Siberian shelf. The Beaufort Sea displays CH_4 concentrations in the range of 1.18 – 67.2 nM with elevated values near the coast (5.5 – 44.4 nM), 67.2 nM at 50 m water depth on the Chukchi shelf as well as 28.8 nM at the North Pole. Near-surface CH_4 concentrations were in the range of 2.46 – 13.7 nM (range from undersaturation to supersaturation) in September 1993. Measurements in the same area from 1992 to 1995 revealed maximum CH_4 concentrations from ice-free water between 5 – 56 nM and significantly higher concentrations under ice-coverage in the range of 12 – 275 nM with typically highest concentrations near the bottom. The authors point to river discharge and sedimentary sources for CH_4 input attributable to seepages of microbial and thermogenic origin (Lorenson et al., 2016). Fenwick et al. (2017) find that surface CH_4 concentration in the Bering and Chukchi Sea and Canada Basin ranged from 3.0 – 7.3 nM (95 – 220 % saturation) and conclude that their study site is a weak source for atmospheric CH_4 with estimated sea-air fluxes of 1.3 µmol/m²/d (range: -0.4 – 4.9 µmol/m²/d). Additionally, they claim that CH_4 concentration depends on the origin of different water masses and point towards an influence of freshwater on enhanced CH_4. CH_4 profiles in the Labrador Sea in late May to early June display concentrations of 2 – 4 nM at depth and higher concentrations of up to 6 nM in the surface layer. Surface saturations were in equilibrium or supersaturated with respect to atmospheric equilibrium (100 – 140 %; Kock, 2007). In October 2011, the West Greenland shelf displayed saturations of 178 – 224 % in near-bottom water and near atmospheric equilibrium near the surface (98 – 127 %). Average CH_4 sea-air fluxes for the entire study site (Davis Strait) were 1.6 µmol/m²/d (range: -0.3 – 9 µmol/m²/d). The authors suggest riverine input, contemporary methanogenesis in anoxic organic rich environments and gas seeps as potential sources of CH_4 and argue that freshwater shows no distinctive influence on CH_4 (Punshon et al., 2014). Despite the aforementioned relatively low fluxes, regional oceanic hotspots have also been reported, e.g. north of Svalbard with rates of 26 nmol/m²/s (Platt et al., 2018). Additionally, surface CH_4 concentration during a sampling campaign in May to August 1997 showed that surface waters south of Greenland were largely in equilibrium with atmospheric partial pressure, and distribution is mainly controlled by microbial oxidation and the respective water mass history (Rehder et al., 1999). Damm et al. (2011) measured Fram Strait water in the range of 2 – 7 nM in the surface and a maximum of 9 nM at

depth in an oxygenated, nitrate-stressed and melt-water influenced environment and point towards a relationship with DMSP concentrations. Oceanic emissions of CH_4 for West Svalbard were determined to be a maximum of 2.5 nmol/m²/s (Pisso et al., 2016). Current atmospheric emissions from the Arctic Ocean are in the range of 1 – 17 $TgCH_4$/yr. This large range illustrates that CH_4 flux estimates are highly uncertain (Worthy et al., 2015) and need to be undergirded by additional as well as more frequent, and spacious measurements.

4 Objectives

The scientific procedures which were conducted in this work are centered around the leading question:

"What are the extent and spatial distribution of the concentration of dissolved CH_4 throughout the water column of the subpolar East Greenland shelf and what are the processes that caused the encountered situation?".

Furthermore, in the light of a projected increase in melting rates with respect to their influence on the subpolar/polar domain as well as its possible impact on global climate I focus on the question:

"How and to what extent does melt-water from land- and sea-derived sources influence the CH_4 distribution throughout the study site?"

To answer these leading questions, the following objectives were set:

(1) identify the distribution of CH_4 on the EGS and compare differences within the study site as well as compare it to other polar/subpolar regions to put it in relation with the local and global setting,

(2) identify links to biogeochemical parameters to infer possible sources or sinks,

(3) elaborate on the water masses on the EGS to infer possible fates of dissolved CH_4,

(4) quantify the interaction of CH_4 between the ocean and atmosphere to infer possible relationships with atmospheric CH_4 cycling.

A thorough understanding of the CH_4 cycling on the EGS is crucial for future implications and measures regarding climate change as CH_4 is a strong contributor to the global budget of climate-relevant trace gases. This importance is furtherly supported by the fact that as of now, knowledge about the distribution and processes that drive CH_4 production in the water column of high-latitude regions is sparse, or particularly for the EGS, non-existent. However, these regions are

extremely sensitive to climatic changes, and the projected increase in melting of the Greenland Ice Sheet as well as (multi-)annual sea ice is predicted to have severe consequences for the aquatic ecosystem as well as the global environment.

To shed light on the CH_4 cycling on the EGS, extensive sampling throughout the study site was conducted during the melt season (July-August 2019) onboard the RV MARIA S. MERIAN during the research cruise MSM85. The objective of this study was to identify the spatial distribution and concentration of CH_4 through seawater sampling. Additionally, numerous physical and chemical parameters were recorded during this cruise which was correlated with CH_4 and thus possible coherences were identified. These parameters will be addressed in the following.

5 Methodology

During the research cruise MSM85, discrete CH_4 water samples were taken from 24 CTD rosette casts as well as 17 underway samples (UW). Overall, seven transects (A, B, C, D, E, F, G) between ~ 63.6 °N to ~ 77.5 °N were navigated perpendicular to the coast of East Greenland (see fig. 8). For each transect, three CTD rosette casts were carried out for CH_4 with one station nearest to the coast, one station on the shelf break, and one station in the open ocean. The CTD casts covered the entire water column at each position. Additionally, to these sections, two individual depth profiles were taken between Greenland and Svalbard at the northernmost position of the cruise track (166, 168).

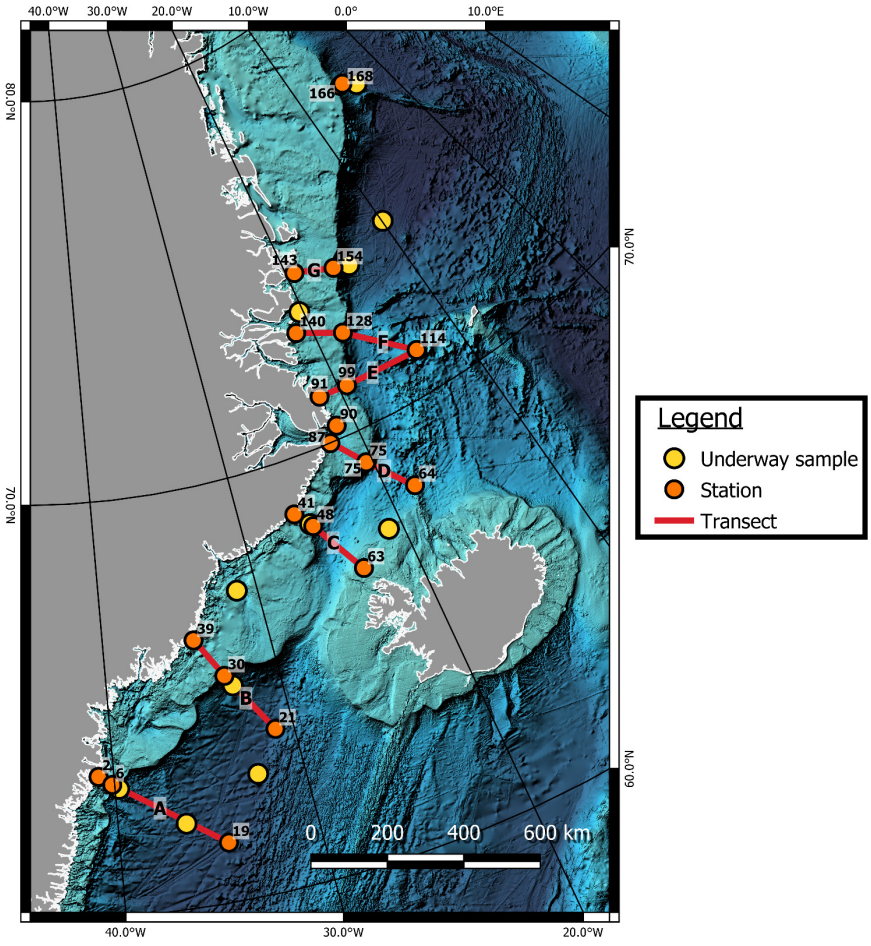

Figure 8: Map of the study site (East Greenland shelf). The **red** line and letters mark the transects. **Orange** dots and numbers mark CH_4 stations and **yellow** dots CH_4 underway sampling locations. Bathymetry constructed by GEBCO 2020 Grid (GEBCO-Compilation-Group, 2020), coastline data provided by GSHHG, SOEST (Wessel et al, 1996).

5.1 Regional Setting

The study site of the EGS is located in the subpolar latitudes and is heavily influenced by the cryosphere.

5.1.1 Oceanographic Setting

The most prominent hydrographic feature of the EGS is the East Greenland Current (EGC, see fig. 9) which is comprised of Arctic Water that is either Atlantic-derived water with contributions from returning Atlantic Water (RAW) and Atlantic-derived Arctic or Pacific-derived Arctic water or a combination of both (AW). RAW is mostly characterized by warm and saline water with a density range of σ_T 27.97 – 30.44. AW on the other hand is cold and less saline and thus shows a lower density interval of σ_T 27.7 – 27.97 (Rudels et al., 2002). The EGC is confined to the intermediate shelf area as well as the shelf break. It flows southbound through the Fram Strait and the Denmark Strait and then bends around Cape Farewell in South Greenland into the Labrador Sea and the Atlantic to form the West Greenland Current (WGC). The volume flux of the EGC is in the order of 1 – 4 Sv (1 Sv = 10^6 m³/s or 10^9 L/s) and it flows with a speed of 20 – 30 cm/s in the upper water column over the continental slope and 5 – 10 cm/s over the shelf (Aagaard and Coachman, 1968; Foldvik et al., 1988; Schlichtholz and Houssais, 1999).

As described in Håvik et al. (2017), the EGC consists of three horizontal and vertical components. The three components are described as follows (see fig. 10): the surface layer consists of Polar Surface Water (PSW). This layer is characterized by a thickness of 120 – 200 m and distinctively high freshwater content due to its origin in the Arctic Ocean and contributions from in-situ seasonal ice melt situ as well as input form the Nordic Seas and the Fram Strait. Furthermore, this layer is comparatively warmer due to summer insolation. Below the surface layer, AW follows with a thickness of roughly 500 – 700 m. It can be distinguished into two components: (1) recirculating water originating directly from the West Spitsbergen Current (WSC) in the Fram Strait and (2) colder and less saline Arctic Atlantic Water which is WSC or Barents Sea water that was modified while flowing through the Arctic Ocean and exits via the Fram Strait into the EGC. The third layer is a deeper water mass that is denser than AW and is increasing in thickness towards the southern shelf, especially south of the Denmark Strait. However, information by the authors about this layer is limited due to low sampling resolution. Horizontally, the EGC can be divided into three components as well. (1) The outer EGC on the shelf-slope diverts significant volumes of water into the Nordic Seas at the Jan-Mayen Fracture Zone as well as north of the Denmark Strait. (2) The shelf break EGS follows the contour of the transition between shelf and slope, as well as (3) a PSW jet along the coast which is heavily influenced by meltwater inflow.

Another prominent feature of the EGC is the East Greenland Coastal Current (EGCC) which is a fast-flowing (peak currents of ~ 1 m/s) water mass flowing parallel to the EGC and wedges against the shoreline of Greenland (Bacon et al., 2002). This water mass is analogous to the PSW jet described above. The authors estimate a transport volume of ~ 0.8 Sv. Sutherland and Pickart (2008) report that freshwater sources from Greenland are in the order of 27.5 mSv. The authors believe that the EGCC originates from a bifurcation of the EGC south of the Denmark Strait due to the bathymetry and contest the existence of the EGCC in the Northern EGS. However, Foukal et al. (2020) claim, that the EGCC exists throughout the entire EGS and report that the northern part of the EGCC supplies around half of the transport south of the Denmark Strait. They suggest that only little input is sourced from the GrIS but is mostly sourced from Arctic-sourced fresh water. In the south, the EGCC and EGC most likely merge due to the narrowing of the shelf here.

De Steur et al. (2009) estimate the annual mean liquid freshwater flux in the EGC on the Western Fram Strait to -40.4 ±14.4 mSv but report that the total volume of transport of the EGC has more than doubled between 2001 and 2008 and attribute it to an increase of deep ocean water transport. This amount of freshwater transported in the EGC accounts for 50 – 75 % of liquid freshwater and sea ice from the Arctic Ocean (Aagaard and Carmack, 1989; Dodd et al., 2009; Serreze et al., 2006) with 63 – 95 mSv of freshwater (Dickson et al., 2007; Meredith et al., 2001) and 59 – 92 mSv of sea ice (Dickson et al., 2007; Kwok et al., 2004). 10 mSv of the latter melts into the EGC while the rest is unaccounted for and either drifts into the Nordic Seas or accumulates over the EGS during summer (Dodd et al., 2009). Aagaard and Carmack (1989) estimated the southbound overall ice export (e.g., ice floes, icebergs) to be 2790 km^3/yr.

South of the Denmark Strait, some of the EGC bottom water exits the shelf break and flows down the continental slope into the Irminger and the Labrador Sea. This so-called East Greenland Spill Jet advects intermediate density water equatorward with an estimated volume transport of 3.3 ±0.7 Sv (von Appen et al., 2014). However, it should be noted that the given estimates for the EGC and the East Greenland Spill Jet are somewhat contradicting as the Spill Jet would advect over 75 % of the EGC which is unlikely. This contradiction most likely stems from measurement uncertainties and fluctuations of EGC transport due to seasonality.

The open ocean adjacent to the EGS is comprised of the Greenland and Iceland Seas between Iceland and Svalbard, as well as the Irminger Sea with the immanent Irminger Current (IC) forming the Irminger Gyre south of Iceland. The IC is a branch of the North Atlantic Current characterized by warm, saline water with $\sigma_T < 27.7$. It bifurcates northward to flow into the Iceland Sea gyre and southbound flowing parallel to the EGC. The potential temperature range of the Irminger Sea in the upper 1000 m is between 3.5 – 12 °C while below this, the temperature range is typically between 1 – 3.5 °C. The surface layer of the Irminger Sea displays a salinity excursion < 34.83, while the deeper water column is typically above this (Våge et al., 2011). The

Greenland Sea surface layer is characterized by a temperature range of 4 – 9 °C whereas temperatures at depth (200 m) are typically between -1 – 4 °C (Quadfasel and Meincke, 1987). The upper 150 m of the Iceland Sea are typically in the range of -1 – 8 °C (Pálsson et al., 2012).

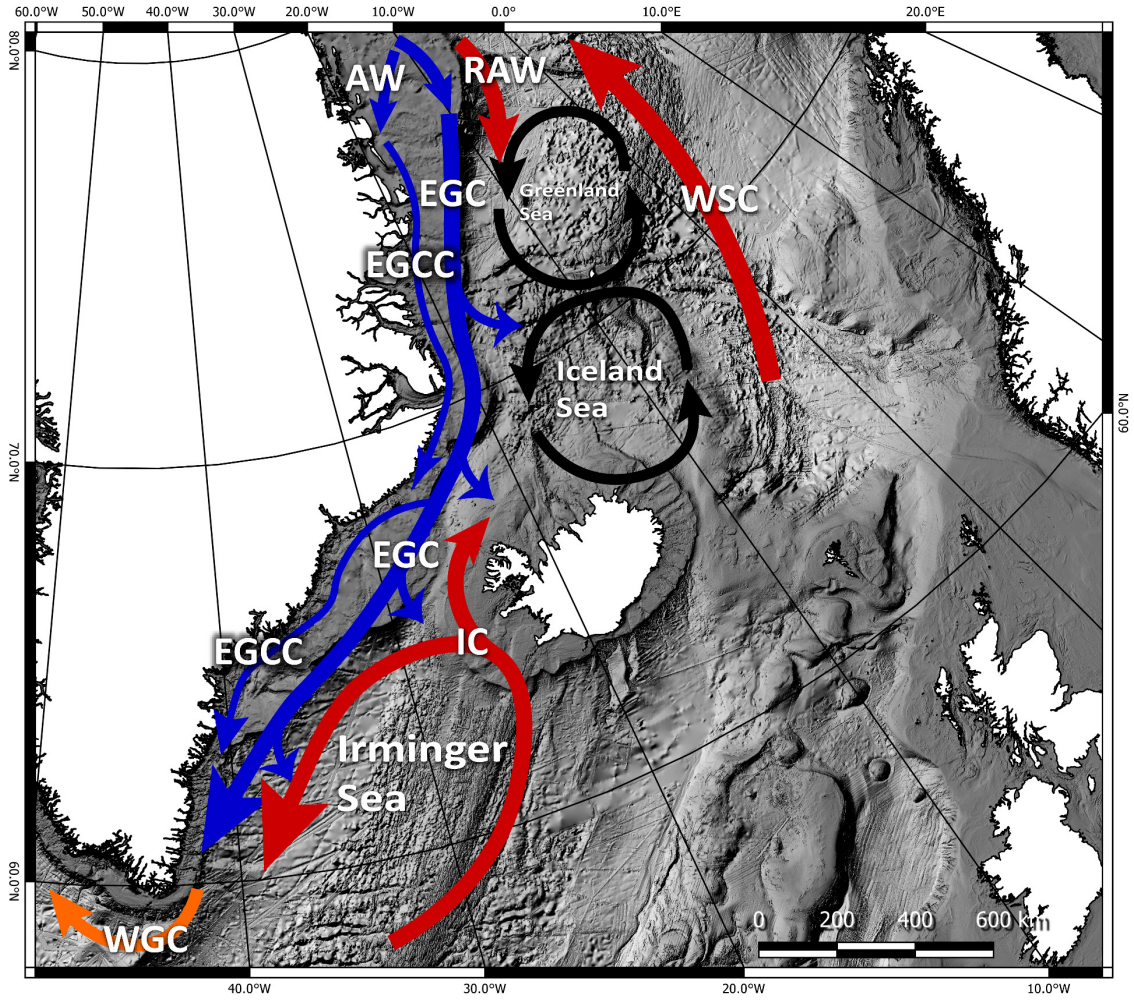

Figure 9: Map of ocean currents and seas adjacent to East Greenland. **Blue** arrows indicate cold, fresher currents. **Red** arrows indicate warm, saline currents. **Black** circles indicate gyres. AW: Arctic Water; EGC: East Greenland Current; EGCC: East Greenland Coastal Current; IC: Irminger Current; RAW: Returning Atlantic Water; WGC: West Greenland Current; WSC: West Spitsbergen Current (information about currents taken from Håvik et al., 2017, Rudels et al., 2002, Sutherland & Pickard, 2008).

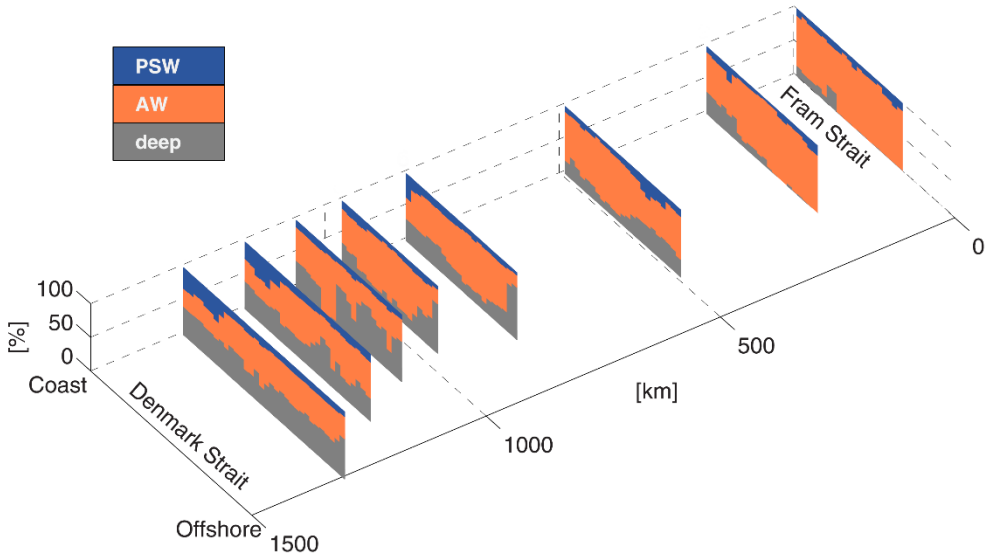

Figure 10: Percent contribution of the water mass end-members of the East Greenland Current (EGC) at different sections along the East Greenland shelf. The x axis displays the distance from the shore [km]. The y axis displays the relative fraction [%] of the end-member contributing to the EGC. The Y-axis shows the distance [km] between each transect relative to their along-stream distance from the Fram Strait and the Denmark Strait. PSW: Polar Surface Water; AW: Atlantic-origin water; deep: deeper water mass (modified after Håvik et al., 2017).

5.1.2 Environmental Conditions during the Cruise

From transect C northward, drift ice and ice floe fields were pervasive (see fig. 11), however, they were largely confined to the coast and the shelf. Additionally, large amounts of icebergs and growlers were frequently encountered from transect A onwards. Surface shelf waters show freshwater influence attributed to both glacial and precipitation run-off from Greenland and sea ice melt with the lowest salinities closest to the coast (see fig. 12; ~ 28 g/kg). Open ocean surface water in the Greenland Sea, North of Iceland, and in the Irminger Sea was nearly at 35 g/kg. Cold surface water was found on the shelf and mainly confined to the north of the study site where the surface water temperature was between 0 – 3 °C. Open ocean surface temperatures in the Greenland Sea and the Iceland Sea were between 5 – 7 °C, the Irminger Sea reached up to 12 °C.

Indeed, the vertical components of the EGC were also encountered during this study (see fig. 13). A fresh, decoupled surface layer resemblant for the PSW was identified. However, the depth did not reach deeper than 30 m. The intermediate water column was characterized by a water mass between 10 – 200 m which displayed a temperature range between -1 – 0 °C and salinities between 32 – 34 g/kg. The negative temperature anomaly of this water mass could either stem

from a higher inflow of the Arctic-derived component during the sampling campaign or could even still resemble PSW as it was described to have a thickness comparable to the thickness of the intermediate water mass found in this study. Below this, a bottom current displays a temperature range between 0 – 3 °C and salinities > 34.5 g/kg. It is narrow in the south and significantly thickens south of the Denmark Strait and therefore, is at par with the aforementioned reports.

A difference in horizontal components could not be observed and thus a horizontal differentiation of the EGC could not be made in this study.

On the northern shelf, the EGC extends along the entire shelf and even partly reaches onto the slope. However, on the southern shelf, south of the Denmark Strait, the EGS progressively narrows and is mainly nestling to the shoreline.

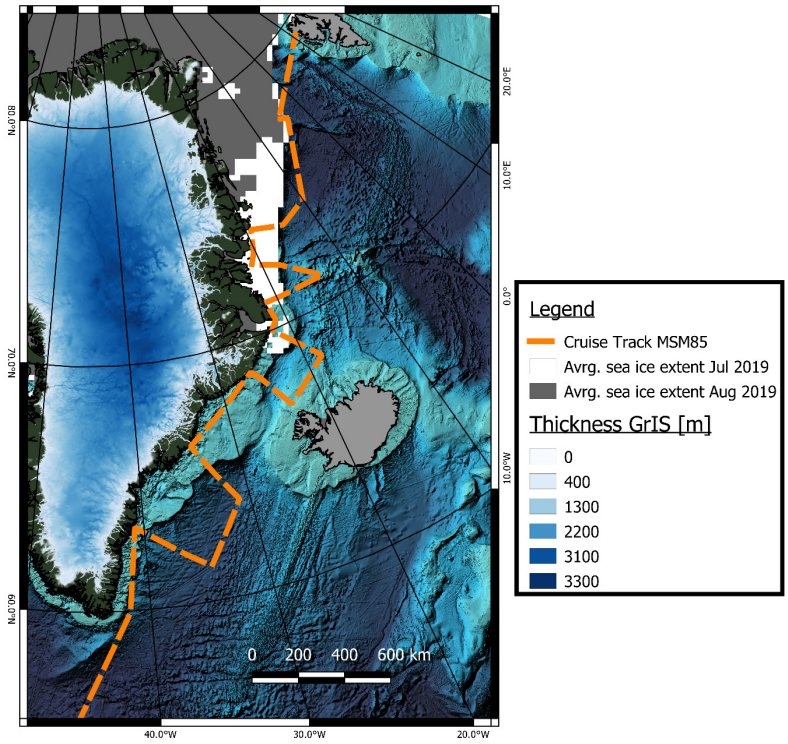

Figure 11: Map of the study site on the EGS. The **orange** line displays the cruise track. The **white** area shows the average sea ice extent in July 2019 and the **grey** area shows the average sea ice extent in August 2019. The modeled thickness of the GrIS is shown in **light blue** gradients (BedMachine v3, Morlighem M. et al., (2017)). Bathymetry constructed by GEBCO 2020 Grid (GEBCO-Compilation-Group, 2020), coastline data provided by GSHHG, SOEST (Wessel et al, 1996).

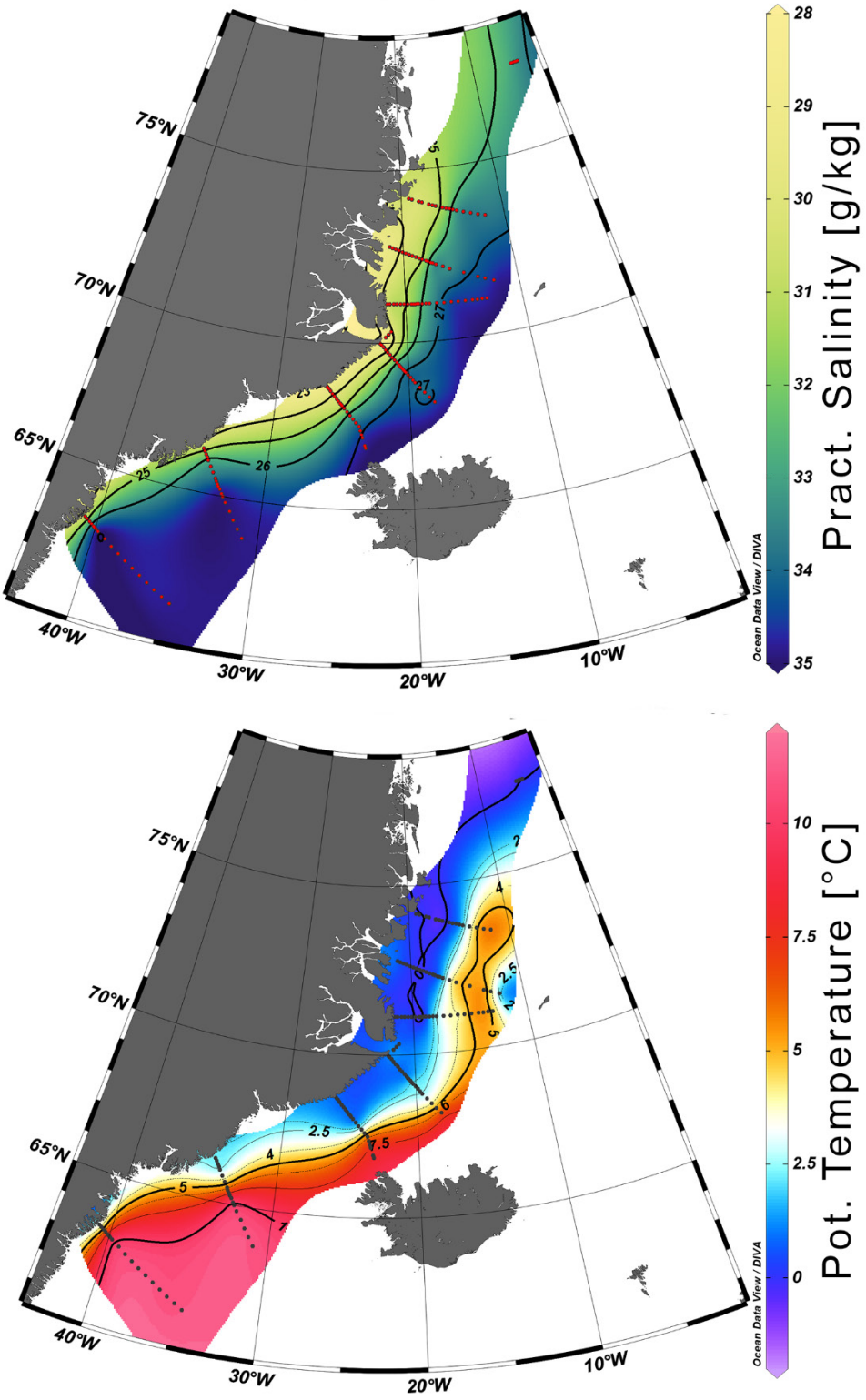

Figure 12: **Top**: Practical salinity distribution [g/kg] (isolines indicate σ_T) and **bottom**: Potential temperature distribution [°C] (isolines are isotherms) in the surface layer of the EGS between July and August 2019.

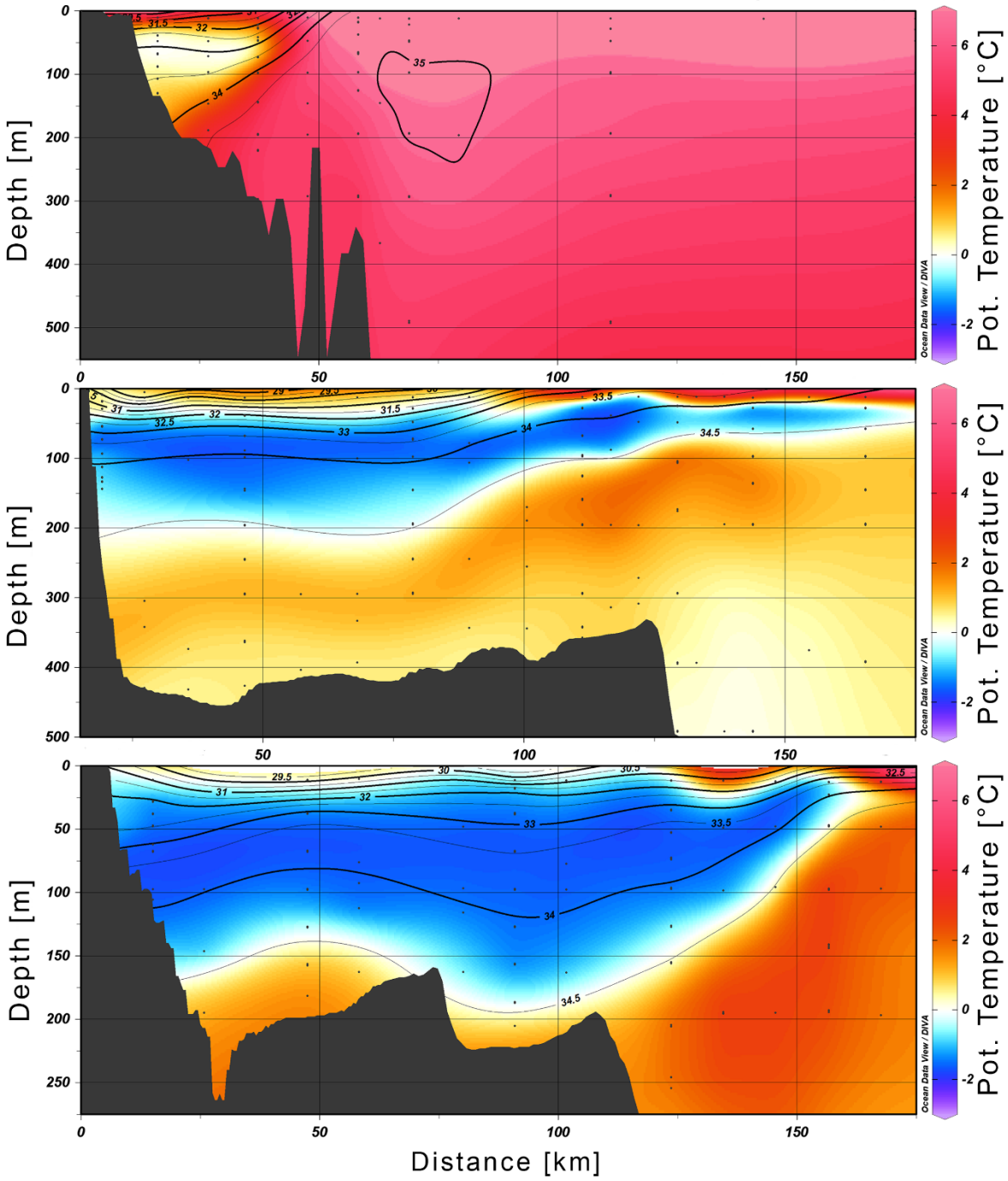

Figure 13: Potential temperature distribution [°C] on the EGS. Isolines display haloclines [g/kg]. Order from south to north. **Top**: transect A, **middle**: transect C, **bottom**: transect G.

5.2 Sampling

The data collection took place from 23rd of July to 13th of August 2019 during melt season where vast amounts of freshwater enter the shelf from surface run-off, sea ice, and ocean currents. The transects were sailed from south to north, trailing the retreating marginal ice zone (MIZ).

For seawater sampling, an SBE CTD rosette was used which was equipped with 22 12 L Niskin bottles, a hydrophone, and a CTD profiler (SeaBird Electronics, Inc. SBE911plus). The profiler was modulated with two temperature probes, two conductivity probes, a Digiquarz pressure sensor, an SBE 43 oxygen sensor, a WET labs ECO-AFL/FL fluorometer, a Wet Labs C-Star transmissometer as well as an altimeter. The sensors are connected to the CTD control room via cable connection where measurements of the sensor's parameters are live-viewed and recorded. The SeaBird module measured salinity, temperature, pressure from which it calculates depth, chlorophyll-α (Chl-α), DO, and turbidity.

At each station, the CTD rosette was lowered with opened Niskin bottles through the water column and halted at an approximate distance to the seafloor (bottom depth). During descent, the CTD parameters were analyzed, and closure depths were determined at distinct anomalies (Chl-α maximum, salinity minimum, temperature minimum, oxygen minimum) as well as at standardized depths (surface, bottom depth, 10 m above bottom depth) to cover the entire water column. Overall, 10 to 11 depths were taken for each station, respectively. Therefore, data resolution was dependent on the water depth. During ascend of the CTD rosette, the Niskin bottles were closed at the desired depth and subsequently, heaved onto the ship deck.

For the Scoresbysund profile (D.2) the overall number of samples taken over depth were reduced to five and seven, respectively, due to lack of time and precarious sea and ice conditions.

Afterward, the water samples were filled into 20 ml glass vials free of any bubbles and with an overflow threefold the volume of the vials. The glass vials were then closed with butyl-rubber stoppers and sealed off with crimped aluminum caps. For each depth, triplicates were taken for the calculation of a mean CH_4 concentration. To conserve the CH_4 concentration and halt any biological activity inside the samples, 50 µl of a mercury chloride solution ($HgCl_{2(aq)}$) was added to each sample with a 1 ml glass syringe immediately after sampling. Poisoning with $HgCl_2$ is an established method for conserving seawater samples (Crabeck et al., 2014; Gülzow et al., 2014; Wilson et al., 2018). During the addition of the $HgCl_2$ solution, an additional open syringe was inserted into the samples to compensate for the added volume in the vials. Subsequently, the vials were shaken for approximately 3 to 5 minutes to distribute the $HgCl_2$-solution evenly. At the end of the expedition, the collected samples were shipped to the Chemical Oceanography Department

of the GEOMAR Helmholtz Centre for Ocean Research Kiel, Germany via air cargo for succeeding measurements. Cold and dark storage conditions were ensured continuously.

For underway (UW) sampling, surface seawater was collected from the vessel's moonpool and transferred onto the ship via a LOWARA submersible pump (Xylem, Germany). The pumped water was subsequently extracted from a tap and filled into 20 ml vials, free of any bubbles and an overflow threefold the volume of the vials. Thereafter, the samples were conserved and stored as well, as mentioned for the CTD sampling. During UW sampling, the position of the ship, surface salinity, and surface temperature were taken from the vessel's data.

5.3 Measurements

The seawater samples were analyzed using an established static headspace (HS) procedure (Kock, 2007). For this, the samples were inspected for any bubbles inside the vials. If any bubbles were present, their size was estimated and noted. Following this, the vials were injected with a headspace consisting of 10 ml CH_4-free helium gas (99.9999 %, AirLiquide, Düsseldorf, Germany) via a gas-tight glass syringe (VICI Precision Sampling, Baton Rouge, USA). Before this, a regular open syringe (BD Plastipak^{TM}, New Jersey, USA) was inserted to compensate for pressure gradients to ensure the integrity of the glass vials. The samples were then shaken vigorously for approximately 30 seconds to reduce gas equilibration time using a test tube shaker (Vortex-Genie 2, Scientific Industries, New York, USA), and left for equilibration for at least two hours. During equilibration, the dissolved CH_4 partially degassed into the HS following Henry's law. After equilibration time, 9 ml of HS was then extracted from the glass vials using, again, a gas-tight glass syringe and injected into a gas chromatograph. During extraction, the temperature of the samples water phase was noted.

The gas chromatographic analysis was carried out using a Hewlett Packard 5890 Series II (Hewlett Packard, Palo Alto, USA) coupled with a flame-ionization detector (FID).

The Gas chromatograph is equipped with a side-port for sample injection which is linked with a 12-port Valco valve (Valco Instruments, Houston, USA). The injection port consists of a metal tube that is sealed off from the surrounding atmosphere with a rubber septum which is penetrated during injection of the HS as well as a dry trap filled with phosphorus pentoxide (SICAPENT®, E. Merck, Darmstadt, Germany) to prevent any humidity from entering the system. The Valco valve can be switched between two positions ('load', 'inject') with a manual handle. While in 'load'-position, the Valco valve is connected to a sample collector tube which, in this position, vents to the outside of the chromatograph. While in 'inject'-position the Valco valve connects the collector tube to a sample loop and a capillary column which in turn are connected to the FID.

The sample loop and column are attached inside an oven which heats up to 60 °C and is continuously perfused with an inert carrier gas (He or Ar). The carrier gas advects the sample from the injector port to the FID unit and thus acts as a mobile phase in the system. The inner tubing of the column is packed with washed mole sieve (mesh 80/100; Alltech GmbH, Germany; stationary phase). Additionally to these units, the chromatograph is equipped with a user interface panel, an electronic data processing unit, as well as a connection to a computer device.

For measurements, the Valco valve is switched to the 'load'-position and the sample is injected into the side port which loads it into the collector tube. Prior to every sample injection, the collector tube is flushed with approximately 10 ml of helium to purge it from any contamination. After injection, the sample is conveyed to the column where it comparts into its specific compound. After passing the sample loop, the comparted substances are propelled into the FID unit discretely from each other, where they are thermally ionized during combustion in an oxyhydrogen ($H_2 + O_2$) flame (approximately 2,000 °C). The electric conductivity of the flame is measured by two electrodes. During ionization of a measured substance, the released electrons alter the electric current and thus in turn create a peak that represents a Gaussian distribution curve. The data is processed and recorded as chromatograms on a computer device using the ChromStar 6.3 software (SCPA, Weyhe-Leeste, Germany).

To calibrate the measurements and convert the recorded data into concentrations of the measured compound, standard calibration gases are measured prior to or after the actual sample measurements. These calibration gases each have a specific mixture of gaseous compounds in highly accurately defined amounts (see table 1).

Table 1: Internal ID of the standard gases used for calibration as well as their respective mole fractions [ppb].

Internal Standard ID	**Mole fraction [x_{CH4}, in ppb]**
5B	110.466
14	2025.297

All gas mixtures have been calibrated against NOAA-PMEL primary standards (Wilson et al., 2018). The calibration gases were picked so that the concentration of the samples CH_4 lies in the concentration range of CH_4 concentrations of the standard gases. To account for the entire range CH_4 concentrations the standard gas 14 was measured undiluted as well as diluted. The dilution factor was 0.33 resulting in a mole fraction of 675.1 ppb. For gas dilution, a volume of 9 ml of standard 14 was extracted from the gas bottles via a gas-tight glass syringe, which was then diluted

with helium (99.9999 %, AirLiquide, Düsseldorf, Germany) to the desired volumetric factor of 0.33 using a gas collecting tube which was priorly decompressed to be at atmospheric pressure and ensure a correct dissolution factor inside the syringe.

5.4 Concentration Calculation

For data processing, the areas of the peaks of the HS samples and calibration gases are integrated using the aforementioned software. The calculated areas of the calibration peaks are converted to concentrations using the known concentration of the standard gas mixtures. Using the offset, the slope of the regression curve from the calibration as well as the peak area of each sample the molar fraction of CH_4 in the HS (X_{CH4}, in ppb) is calculated:

$$X_{CH4} = \frac{PA - o}{\frac{1}{m}}$$

Where:

X_{CH4}: Mole fraction of CH_4 in HS [ppb]

PA: Integrated peak area [-]

o: Offset of regression line [ppb]

$1/m$: The slope of regression line [-]

Afterwards, using Henry's law, the CH_4 concentration of the HS (C_{CH4_HS}, in nmol/L) is calculated using the following formula (Henry and Banks, 1803):

$$C_{CH4\_HS} = \frac{p * X_{CH4}}{\frac{R*T}{1000*(\frac{V_W}{V_{HS}})}}$$

Where:

C_{CH4_HS}: Concentration of CH_4 in HS [nmol/L]

p: Partial pressure [bar]

X_{CH4}: Molar fraction in HS [ppb]

R: Gas constant $\left[\frac{kg*m^2}{s^2*mol*K}\right]$

T: Sample equilibration temperature converted from °C to [K]

V_W/V_{HS}: Ratio of volume in the water phase and volume in HS [-]

For this work, the vials' exact volumes were determined. For this, a set number of vials (n = 20) from the batch used in this work were selected, closed with butyl rubber stoppers, and weighted using a precision scale. After that, the vials were filled with ultra-pure water (MilliQ, E. Merck, Darmstadt, Germany) which equilibrated to room temperature prior to this. The filled vials were weighted again. Subsequently, the mass of the water was determined by the following:

$$m_{\mathrm{w}} = m_{\mathrm{b_f}} - m_{\mathrm{b_e}}$$

Where:

m_w: Mass of water inside the vials [g]

m_{b_f}: Mass of the filled bottles [g]

m_{b_e}: Mass of the empty bottles [g]

From this, the volume of the vials was determined with:

$$V_{\mathrm{v}} = \frac{m_{\mathrm{w}}}{\rho_{\mathrm{w}}}$$

Where:

V_v: Volume of vials [ml]

ρ: Density of pure water at 25 °C [0.997 g/cm³]

The average volume of the vials was determined to be 22.03 ml through which the ratio between the volume of the water phase (V_w) and the volume of the HS (V_{HS}) (V_W/V_{HS}) was calculated.

Following this, the equilibrium concentration in the water (C_{CH4_W}, in nmol/L) was calculated using the molar fraction in the HS, the samples specific Bunsen equilibrium solubility of CH_4 with their respective coefficients (see table 2, Wiesenburg and Guinasso, (1979)):

$$S_{\mathrm{eq}} = e^{\left(A1+A2*\left(\frac{100}{T}\right)\right)+A3*\ln\left(\frac{T}{100}\right)+A4*\left(\frac{T}{100}\right)+S‰*\left(B1+B2*\left(\frac{T}{100}\right)\right)+B3*\left(\frac{T}{100}\right)^2}$$

Where:

S_{eq} = Equilibrium Solubility [nmol/L atm]

$S‰$ = Salinity [g/kg]

Table 2: Constants for Calculation of CH_4 Solubilities in nmol/L from Moist Air at 1 Atm Total Pressure (Wiesenburg and Guinasso, 1979).

A1	*A2*	*A3*	*A4*	*B1*	*B2*	*B3*
-415.2807	596.8104	379.2599	-62.0757	-0.05916	0.032174	-0.0048198

and

$$C_{\mathrm{CH4\_w}} = \frac{\left(X_{\mathrm{CH4}} * S_{\mathrm{eq}}\right)}{10^9}$$

Where:

$C_{\mathrm{CH4\_w}}$: Equilibrium concentration in the water phase [nmol/L]

Subsequently, the CH_4 concentration in the HS was added to the equilibrium concentration of CH_4 to calculate the resulting total CH_4 concentration in the sample.

$$C_{\mathrm{CH4\_nmol/L}} = C_{\mathrm{CH4\_HS}} + C_{\mathrm{CH4\_w}}$$

Where:

$C_{\mathrm{CH4\_nmol/L}}$: Total CH_4 concentration of the sample [nmol/L]

Mean CH_4 concentrations, as well as standard deviations, were calculated using the triplicates' total concentrations. Furthermore, CH_4 concentrations in nmol/L were standardized to nmol/kg using the in-situ density of each sample (kg/m³) to account for varying volumes due to variations in salinity and temperature in the seawater sample.

$$C_{\mathrm{CH4}} = \frac{C_{\mathrm{CH4}_{\frac{\mathrm{nmol}}{\mathrm{L}}}} * 1000}{\rho}$$

Where:

ρ: In-situ density [kg/m^3]

For a complete list of calculated CH_4 concentrations see *appendix A table 3*.

5.5 Air-Sea Flux Calculation

Net air-sea flux calculation of CH_4 on the EGS was carried out using the gas exchange parameterization by Wanninkhof (2014):

$$F_{\mathrm{CH4}} = k * \left(C_{\mathrm{CH4sw}} - C_{\mathrm{CH4eq}}\right)$$

Where:

F_{CH4}: Net flux of CH_4 between sea-air-interface [nmol/m²*h]

k: Gas transfer velocity [cm/h]

C_{CH4sw}: Concentration of CH_4 [nmol/kg]

C_{CH4eq}: Equilibrium concentration of CH_4 [nmol/kg]

Gas fluxes were first calculated for each station and then subsequently averaged for the entire study site. The values were then converted to the unit [µmol/m²/s].

k was calculated using:

$$k = 0.251 * u^2 * \left(\frac{Sc}{660}\right)^{-0.5}$$

Where:

u^2: Averaged and squared instantaneous windspeeds u [m/s]

Sc: Schmidt's Number

Wind speeds were recorded by an ultrasonic anemometer (Thies CLIMA, Göttingen, Germany), every minute at a height of 31.5 m. For each station all wind speed records within a 60 km radius were averaged and subsequently normalized for a height of 10 m above the sea surface using (Justus and Mikhail, 1976):

$$U_{10} = u * \left(\frac{Z_{10}}{Z_{\mathrm{ws}}}\right)^{af}$$

Where:

u_{10}: Averaged zonal windspeed normalized to 10 m above sea surface [m/s]

u: Averaged zonal wind speed [m/s]

Z_{10}: Height of 10 m [m]

Z_{ws}: Height of shipboard wind sensor's [m]

af: Atmospheric stability factor

The atmospheric stability factor was calculated using the following formula (Justus and Mikhail, 1976):

$$af = \left(\frac{0.37 - 0.0881 * \ln(u)}{1 - 0.0881 * \ln\left(\frac{Z_{\mathrm{ws}}}{10}\right)}\right)$$

Schmidt's Number (Sc) was determined using (Wanninkhof, 2014):

$$Sc = \frac{\nu}{D}$$

Where:

ν: Kinematic viscosity of the water [m²/s]

D: Diffusion coefficient of the gas [m²/s]

Diffusion coefficients were adopted from Jähne et al. (1987).

And v was calculated using:

$$\nu = \frac{\mu_{sw}}{\rho}$$

Where:

μ_{sw}: Molecular viscosity of seawater [Pa*s] or [kg/m*s]

And μ_{sw} after (Sharqawy et al., 2010):

$$\mu_{sw} = \mu_{pw}(1 * A * (Cl^{0.5}) + B * Cl$$

Where:

μ_{pw}: Molecular viscosity of pure water [Pa*s] or [kg/m*s]

Cl: Volumetric chlorinity [g/kg]

A was calculated using (Sharqawy et al., 2010):

$$A = (5.185 * 10^{-5}) * T + (1.0675 * 10^{-4})$$

B was calculated using (Sharqawy et al., 2010):

$$B = (3.3 * 10^{-5}) * T + (2.591 * 10^{-3})$$

Volumetric chlorinity was calculated using (Sharqawy et al., 2010):

$$Cl = \frac{\rho * S‰}{1806.55}$$

And μ_{pw} was calculated using (Dorsey, 1940):

$$\mu_{pw} = (4.2844 * 10^{-5}) + (0.157 * ((T + 64.993)^{2-91.296})^{-1})$$

5.6 Uncertainty Estimate

To ensure the correctness and integrity of the hypotheses claimed in this work, a critical quality assessment was carried out for the measured data.

The overall mean of all triplicate concentrations was 3.92 ±1.14 nmol/kg with a mean coefficient of variation of 0.31.

Generally, static HS measurements of dissolved CH_4 are error-prone due to the relatively high CH_4 concentration in the atmosphere (1.8 ppm) compared to the molar fraction of CH_4 in the equilibrated HS (~ 0.14 ppm in this study).

Sources for contamination are various. During sampling, bubbles easily get trapped inside the vial during the closure with the butyl-rubber stoppers. When the samples are stored in the ship's laboratory, temperature differences and associated volumetric changes of the water inside the samples can lead to leakages and contaminations of the samples. However, this problem is more significant for warm water samples than the laboratory's room temperature as their volume decreases over time creating a lower pressure inside the vial than the surrounding atmosphere. Nonetheless, cold samples increase in volume when stored at room temperature and thus create overpressure inside the vials which potentially can lead to bursting vials. The mean sample temperature in this study was 2.4 °C. During temperature equilibration to room temperature in the ship's laboratory (20 °C), this would result in a volumetric increase of less than 0.5 %. To avoid any disturbances by over-pressurization, selected samples that showed signs of overpressure were pressure balanced by inserting a thin needle into the butyl-rubber stoppers for a second.

During measurements, all noticeable problems were protocolled and subsequently flagged to be able to put data points with high standard deviations into better context during the assessment. General flag criteria were:

(1) incorrect or late switching of the injection valve during measurements,

(2) humidity in the syringe (as humid air distorts CH_4 values),

(3) noticeable air contaminations during the extraction of the HS,

(4) the size of bubbles if some were present or

(5) whether the volume of the HS was lower or higher than the targeted 9 ml. Also,

(6) whether the dry trap was tight,

(7) whether any aluminum cap was damaged,

(8) whether any peak was superimposed by a contamination peak, or

(9) when the measurements were apparently below the detection limit of the measuring device. Other noticed problems were categorized as “other”.

One of the 724 measurements was flagged with incorrect or late switching of the injection valve. However, this sample did not show any anomalous standard deviation and thus was used for data interpretation. 8/724 measurements were influenced by humidity in the syringe. Six of these measurements were discarded. The remaining two were kept as standard deviation did not show any anomalies. 4/724 measurements had noticeable air contaminations during the extraction of the HS. All of these samples were discarded. The number of bubbles inside the vials was generally low, as only 24 of 724 samples contained bubbles. Five of which were discarded due to high standard deviations. These samples, however, were also apparently falling below the detection limit. Five of all samples were flagged with having a HS volume lower than 9 ml and 17 with having a HS volume higher than 9 ml. Out of these 22 samples, all the low HS volume samples, and eleven of the high HS volume samples, were discarded due to high standard deviations. 6/724 were flagged as “other”, which included empty sample vials. This resulted from human error during sample collection. Some samples under this category were also flagged due to clogged syringes during extraction of the sample or injection into the injection port. No samples with the “other”-flag resulted were measured. Out of all samples, 250/724 showed negative values. All these samples were discarded. As a result, this heavily decreased the spatial resolution of some profiles and even led to the loss of several stations. Negative values most likely result from a combination of in-situ values which undercut the detection limit, as well as fluctuations of the operational conditions of the gas chromatograph over time which resulted in a varying precision. The first is assumed as concentrations were generally low in the entire study site and especially low for open-ocean stations (see chapter “Results and Discussion”). Most negative values were found at open-ocean stations or at the entrance of the Scoresbysund where concentrations were generally low or displayed a high range, respectively. Magen et al. (2014) report a detection limit of 0.74 nmol/L for an analogous but improved headspace measurement technique for CH_4 determination, indicating that values from this study were indeed close to or below the detection limit. Variations in mean peak area show the same variation pattern over time (see *appendix A, fig. 26*). This figure also shows that numerous samples fall below the lowest used standard.

In the following, only stations which displayed a coefficient of variation of < 80 % are elaborated.

Prior to every measurement series, the dry trap was controlled, and the aluminum caps integrity was inspected. No caps showed signs of damage or corrosion.

Naturally, measurements are subject to human error, however this study was conducted with the goal to keep this factor to a minimum.

6 Results and Discussion

In the following, three distinct regions are analyzed regarding the distribution of dissolved CH_4 in the surface layer and the water column of the EGS. First, the coastal waters which are in the direct vicinity of the shoreline of Greenland are analyzed, followed by the shelf break where usually large fluctuations in oceanographic parameters occur as it marks the transitional zone between the shallow shelf area and the open ocean. The third analyzed area is the open ocean which here refers to the entire area beyond the shelf break.

6.1 Surface CH_4 Distribution

Overall, the mean concentration of dissolved CH_4 in the surface layer of the EGS water column was 3.74 ±2.35 nmol/kg (see fig. 14; range: 0.59 – 12.34; 5^{th} to 95^{th} percentile: 1.26 – 6.12 nmol/kg) and thus is in a similar order as CH_4 from other Arctic shelfs as described in *3.4 Oceanic CH_4 in the Polar and Subpolar Latitudes*.

To decipher any possible meltwater effects from retreating sea ice and land-derived meltwater, the study site was divided into two regions:

(1) The southern site which in the following will be referred to as the South-eastern shelf (SEAS; < 69 °N) and,

(2) the northern site which will be referred to as the North-eastern shelf (NEAS; > 69 °N), where sea ice was ubiquitous.

SEAS includes transects A, B, C and thus represents the region north of Cape Farewell up to the Denmark Strait. The NEAS includes transects D, E, F, G and consequently represents the region between the Fram Strait and the Denmark Strait.

The NEAS displayed a mean surface CH_4 concentration of 3.56 ±1.6 nmol/kg (range: 0.59 – 6.17; 5^{th} to 95^{th} percentile: 1.08 – 5.9 nmol/kg), while the SEAS displayed slightly higher values of 4.21 ±3.23 nmol/kg (range: 1.45 – 12.34; 5^{th} to 95^{th} percentile: 1.8 – 9.3 nmol/kg). SEAS mean values were considerably raised by one near-surface CTD sample (station 30) where concentrations of 12.34 nmol/kg were recorded. Excluding this station lowers the southern surface concentrations to a mean of 3.3 ±1.2 nmol/kg (range: 1.45 – 5.5; 5^{th} to 95^{th} percentile: 1.77 – 4.93 nmol/kg). As these anomalous high concentrations of station 30 (surface sample) were more than three times higher than the average CH_4 concentration of the study site and no additional anomalies were found in analogical magnitudes, regional effects most likely play a role at this station. Nonetheless, standard deviations met the quality control criteria of this dataset, and

therefore the results are depicted with and without this local anomaly as this station greatly distorts the averaged values. The highest concentrations of dissolved CH_4 in the surface layer on the NEAS were found at the southside of the outlet of the Scoresbysund (5.69 ±0.78 nmol/kg) and in coastal waters of glacier outlets in the King Christian X. land (4.83 ±0.4 and 6.17 ±0.01 nmol/kg).

The coastal stations displayed average concentrations of 4.59 ±1.16 nmol/kg (range: 2.9 – 6.17; 5th to 95th percentile: 3.06 – 6 nmol/kg) while the shelf break was at 5.24 ±3.72 nmol/kg (range: 1.45 – 12.34; 5th to 95th percentile: 1.46 – 9.82 nmol/kg) and the open ocean at 1.93 ±0.7 nmol/kg (range: 1.23 – 2.77; 5th to 95th percentile: 1.28 – 2.69 nmol/kg), respectively. Excluding the surface sample of station 30, the average CH_4 concentration at the shelf break was at 2.87 ±1.13 nmol/kg (range: 1.45 – 3.93; 5th to 95th percentile: 1.46 – 3.89 nmol/kg). Considering this, the surface CH_4 concentration displayed a distinct progressively increasing gradient towards the coast and a slight downward gradient from north to south (excluding station 30).

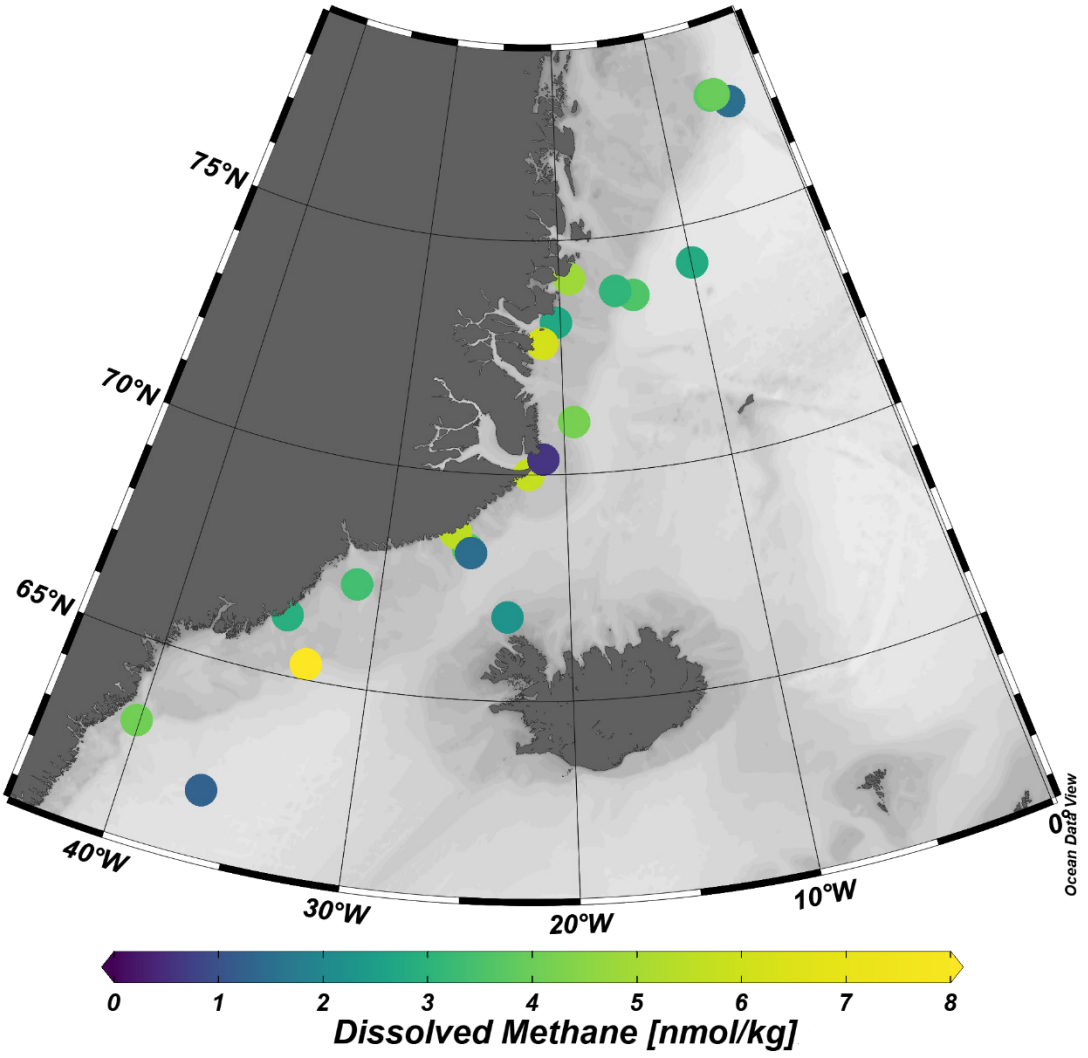

Figure 14: Distribution of dissolved CH_4 [nmol/kg] in the surface layer in the water column of the EGS.

6.2 Sea-Air CH_4 Fluxes

To solidify knowledge about the system interaction between the upper ocean and the atmosphere in the subpolar region of the EGS, CH_4 saturations and sea-air fluxes were calculated.

Overall, the EGS was nearly at equilibrium with the atmosphere. The saturation of dissolved CH_4 for the entire study site was at 101.18 % and thus it represented a minor source for CH_4 to the atmosphere. A comparison of the NEAS and the SEAS showed no major gradients. While the SEAS (< 69 °N) displayed a saturation of 100.35 %, the NEAS (> 69 °N) was at 101.87 %. However, a strong gradient from coast to open ocean was observed where the highest saturations were found at the coast with 116.66 % (range: 16.46 – 173.26 %), 94.31 % (range: 41.12 – 116.62 %) at the shelf break, and 65.09 % (range: 41.92 – 92.85 %) in the open ocean. Additional to the saturation gradient, it was prominent that the range of the saturations also decreased with increasing distance to the coast. This is most likely attributed to the fact that the coastal regions are more dynamic regarding the fluctuation of meltwater input and surface run-off.

These conditions caused an overall CH_4 flux of -0.11 ±1.52 µmol/m²/s or -9487.13 µmol/m²/d. The discrepancy between the slight supersaturation and the negative flux arises from uncertainties introduced by the calculation and the fact that this system is in near equilibrium. North-south trends of CH_4 fluxes were in a similar order. While the NEAS (> 69 °N) showed fluxes of -0.06 µmol/m²/s, the SEAS (< 69 °N) was at -0.17 µmol/m²/s. The slight differences in fluxes were mainly attributed to a higher gas transfer velocity in the SEAS due to a storm event between Greenland and Iceland with averaged wind speeds of 7 – 8 bft (see fig. 15). Additionally, Damm et al. (2015a) argue, that a partial sea ice coverage, which was present on the northern shelf, effectively reduces turbulences in the surface layer and thus restricts gas transfer to the atmosphere.

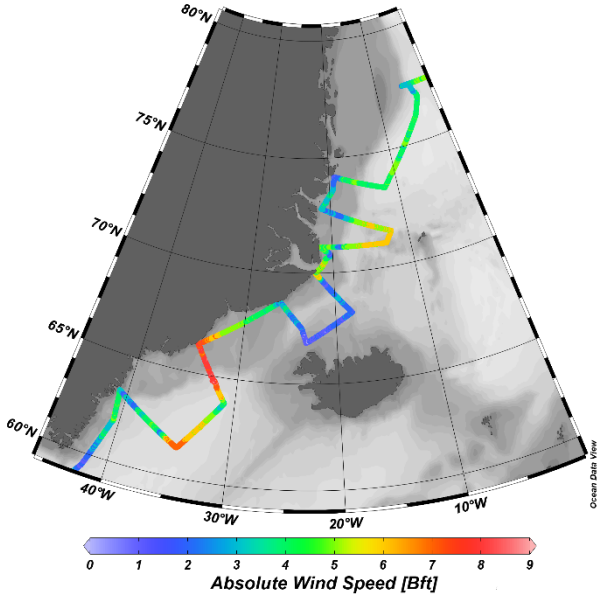

Figure 15: Absolute near surface wind speed [bft] distribution on the EGS between July and August 2019.

6.3 CH_4 Water Column Distribution

Overall, at depth, dissolved CH_4 averaged 3.92 ±6.85 nmol/kg (range: 0.01 – 66.85; 5th to 95th percentile: 0.26 – 11.99 nmol/kg). On the shelf, CH_4 was more than 2 – 4 times higher compared to the open ocean. The highest average CH_4 concentrations were found closest to the coast with a value of 7.77 ±11.52 nmol/kg (range: 0.22 – 66.85; 5th to 95th percentile: 0.39 – 26.21 nmol/kg) (see fig. 16). However, the average was strongly influenced by station 2 which showed significantly higher CH_4 concentrations (maximum: 66.85 nmol/kg). Without this station, the average coastal CH_4 concentration dropped to 3.57 ±3 nmol/kg (range: 0.22 – 11.1; 5th to 95th percentile: 0.37 – 10.2 nmol/kg) which was analogous to the average CH_4 concentration on the shelf break with 3.24 ±2.45 nmol/kg (range: 0.54 – 12.34; 5th to 95th percentile: 0.63 – 7.34 nmol/kg) and thus is roughly uniform for the entire shelf. Compared to this, the average CH_4 concentration on the open ocean was 1.81 ±1.73 nmol/kg (range: 0.14 – 6.39; 5th to 95th percentile: 0.29 - 6 nmol/kg).

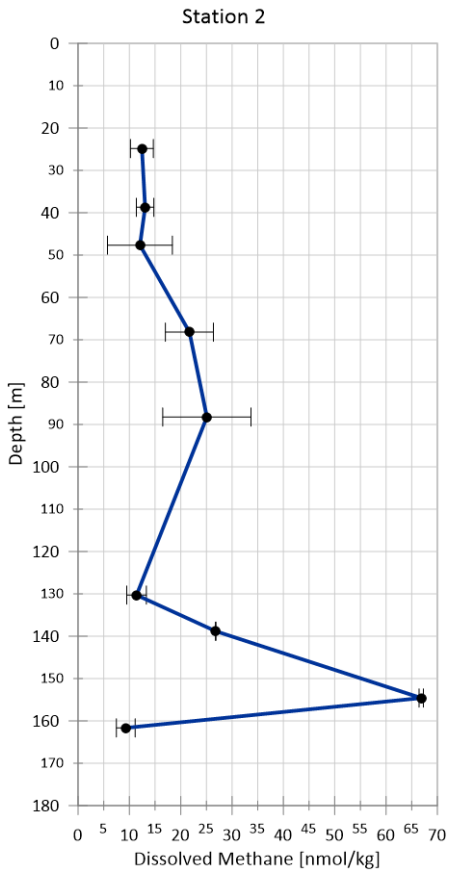

Figure 16: CH_4 [nmol/kg] depth [m] profile of station 2. Error bars indicate standard deviation.

Similar to the surface distribution, CH_4 at depth also displayed regional variability. The NEAS exhibited an overall average CH_4 concentration of 1.8 ±1.42 nmol/kg (range: 0.01 – 6.17; 5th to 95th percentile: 0.24 – 4.19 nmol/kg) while the SEAS was at 6.2 ±9.29 nmol/kg (range: 0.14 – 66.85; 5th to 95th percentile: 0.41 – 21.86 nmol/kg). However, the latter was again considerably raised by station 2. Without it, the average concentration showed a value of 3.73 ±3 nmol/kg (range: 0.14 – 12.34; 5th to 95th percentile: 0.4 – 10.56 nmol/kg).

Generally, the distribution pattern of dissolved CH_4 at depth can give information about its pathways and will be described in the following.

6.3.1 Upper Water Column

The upper water column (0 – 100 m) universally displayed two distinctive features (see fig. 17): (1) A strict upward increasing gradient and (2) a CH_4 maximum in the depth between 18 – 50 m. The first was observed at stations 30, 90, 91 99, 128, 140, 143, 154, 166, 168 and thus was mainly situated in the NEAS. The latter was observed at stations 6, 39, 41, and 48 and thus is mainly confined to the SEAS. For the first scenario section, *6.1 Surface CH_4 Distribution* describes the concentration ranges for the surface layer. For the second scenario, the CH_4 maximum typically ranged between 4.52 – 11.86 nmol/kg. Stations 41 and 48 (both transect C) showed comparatively broader CH_4 maximums. Strict upward gradients are indicative of a CH_4 source at the interface between the ocean and the atmosphere. These sources could be diffusive fluxes from the atmosphere, processes involving sea ice, in-situ CH_4 generation in the upper surface layer, or advection of CH_4 saturated water masses to the study site. Considering that the NEAS surface saturation of CH_4 is in near equilibrium with the atmosphere, gradient-driven fluxes between the atmosphere and the ocean are unlikely which is also reflected in the marginal fluxes presented in *6.2 Sea-Air CH_4 Fluxes*. On the other hand, CH_4 maxima in the lower surface mixed layer are indicative for either in-situ production or advection of CH_4-laden water masses by either vertically or horizontal transport.

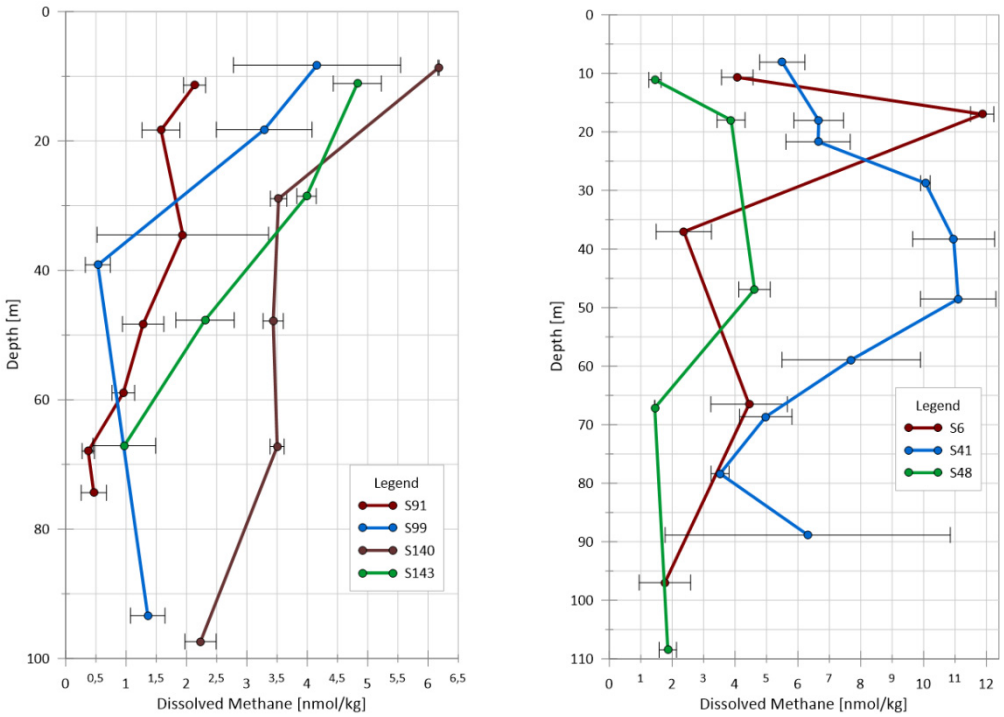

Figure 17: **Left**: Exemplary selection of CH_4 [nmol/kg] depth [m] profiles which display an upward increasing gradient towards the surface; **right**: Exemplary selection of CH_4 [nmol/kg] depth [m] profiles which display a CH_4 maximum in the deeper mixed layer. Error bars indicate the standard deviation [nmol/kg]. Note that the lower data limits displayed in these graphs are not the lower data limits of all shown stations (e.g., bottom depth) but rather display the topmost 100 m of the water column.

6.3.2 Intermediate Water Column

The intermediate water column (100 – 400 m for the shelf as well as 100 – 2000 m for the continental slope and open ocean) is commonly characterized by a CH_4 minimum which is present in nearly every depth profile. Here, concentrations often reached below the detection limit.

6.3.3 Lower Water Column

Enhanced CH_4 near the bottom was a frequent feature for shelf profiles and was found at stations (see fig. 18): 2, 6, 30, 39, 41, 87, and 140 with a range of 1.3 – 9.3 nmol/kg and thus was present on the entire extent of the shelf but more frequently in the SEAS. The following three pathways can lead to this situation: (1) diffusive fluxes which indicate a sedimentary source, (2) bottom currents with enhanced CH_4 which indicate an allochthonous source for CH_4, (3) solution of CH_4 from ebullition fluxes which is also indicative for a sedimentary source. The first pathway can be distinguished from the latter two as purely diffusive fluxes strictly display a decreasing upward gradient. However, the sampling resolution of this study is not sufficient to further distinguish between the specific pathways.

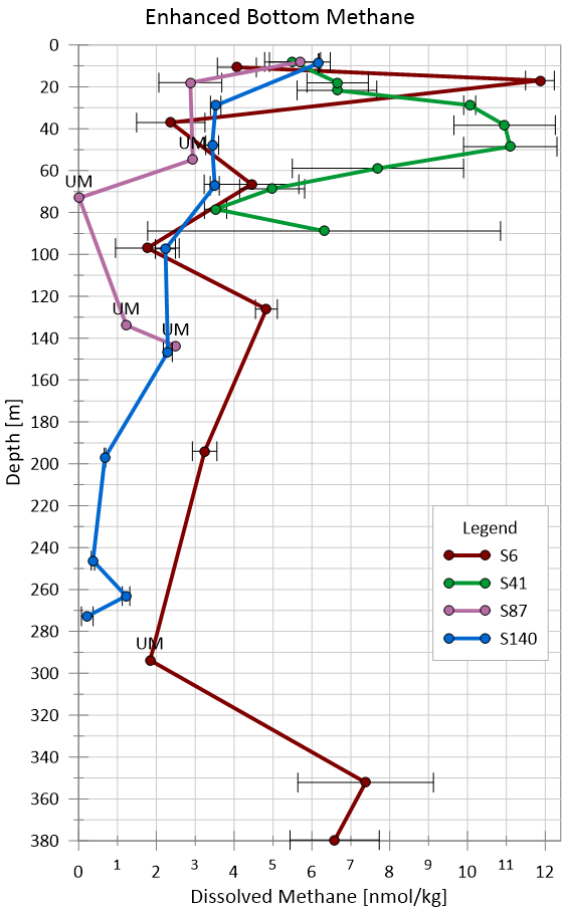

Figure 18: Exemplary selection of CH_4 [nmol/kg] depth [m] profiles which display increased CH_4 near or at the bottom.

Mean CH_4 concentrations over depth of coastal station 2 featured the highest values of the study site with 23.48 ±5.99 nmol/kg which is 6 times higher than the average for the entire site. Despite the evidently enhanced concentration of CH_4 of this station compared to all other stations, it displayed no distinct correlations regarding temperature, salinity, DO, AOU, turbidity, Chl-α or dissolved and particulate organic matter (which are discussed in the following). Thus, the origin of this anomaly cannot be distinguished within the context of this work. However, the lack of connection to any of the parameters above suggests a direct insertion of CH_4 which could be mediated by ebullition although this pathway cannot be explicitly differentiated due to the limited resources of this study.

6.4 Analysis with Biogeochemical Parameters

6.4.1 Temperature and Salinity

To differentiate between sea water which is under a strong influence of meltwater and sea water which tends towards the average global salinity (~ 35 g/L), the first will be referred to as meltwater-influenced water (MIW) and reflects water masses that display salinities below 34.5 g/kg, whereas the latter will be referred to as higher-salinity water (HSW) and displays water masses with a salinity greater than 34.5 g/kg (see fig. 19).

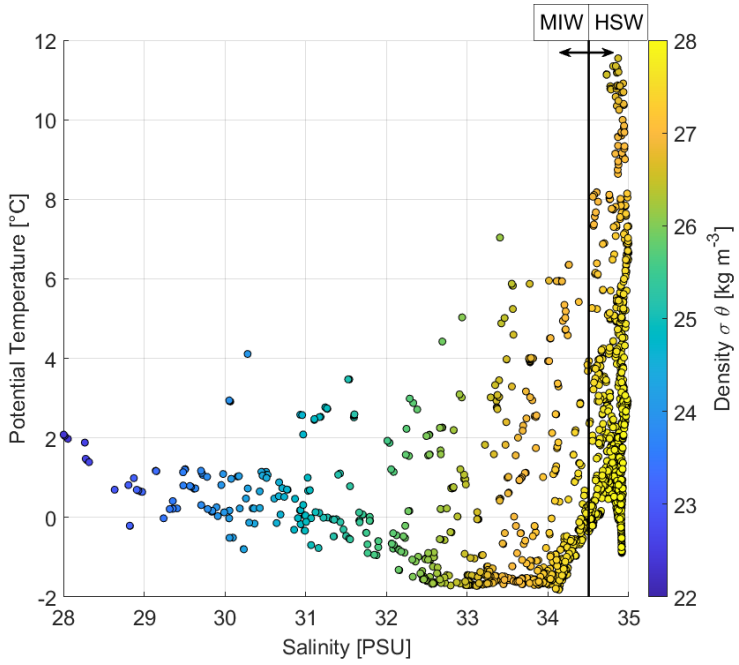

Figure 19: Scatterplot of the practical salinity and potential temperature [°C] with density anomaly distribution [kg/m³] of all data points taken during MSM85 of the EGS water column. MIW: meltwater-influenced water, HSW: higher-salinity water.

Throughout the water column, HSW featured a temperature range from -0.42 – 11.35 °C. Contrarily, MIW did not exceed temperatures of 3 °C and displayed an average temperature of -0.13 °C, indicating that the influence of meltwater is not bound to the surface layer. Prominently, as for the surface, enhanced CH_4 is associated with MIW at depth. The HSW masses showed average CH_4 concentrations of just 2.29 ±2.46 nmol/kg (range: 0.01 – 12.34; 5^{th} to 95^{th} percentile: 0.17 – 6.56 nmol/kg) compared to the fresher water which displayed an average of 5.72 ±9.31 nmol/kg (range: 0.01 – 66.85; 5^{th} to 95^{th} percentile: 0.467 – 22.03 nmol/kg). Additionally, the standard deviation, range, and percentile fraction exhibit more pronounced variabilities for CH_4 in meltwater.

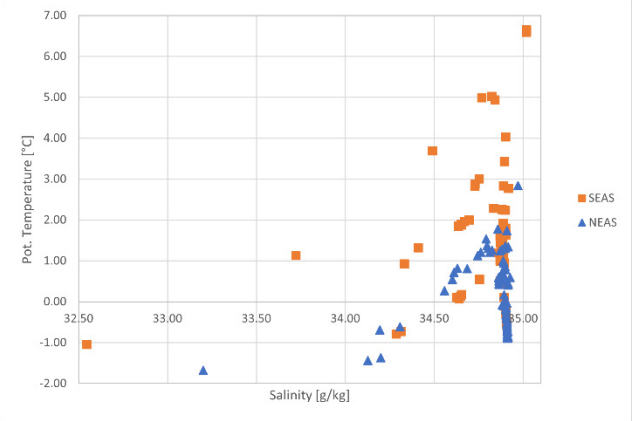

Figure 20: Scatterplot of the practical salinity and potential temperature [°C] of the bottom water on the North-eastern Shelf (NEAS) and the South-eastern Shelf (SEAS) of the EGS.

Bottom water temperatures of the SEAS and NEAS show significant disparities between each other (see fig. 20). While the SEAS displays an average bottom water temperature of 1.82 ±2.23 °C with a comparatively higher variability, the NEAS is at 0.52 ±0.6 °C. As enhanced bottom water temperatures and enhanced bottom CH_4 concentrations coincide in the SEAS, this could be indicative for either enhanced microbial activity and respectively enhanced methanogenesis in the sediments or release of CH_4 through a thawing permafrost cap.

6.4.2 DO and AOU

As methanogens thrive under anoxic conditions, high amounts of dissolved CH_4 are typically found in low-oxygenated waters. In this study, DO range between 261 and 400 µmol/kg with an average of 320.7 ±34.2 µmol/kg, showing that even at depth the redox conditions can be considered oxic. Even though the lowest oxygen levels encountered at station 30 were lower compared to most other stations (261 µmol/kg), they were still too high to be considered anoxic (DO: 0 µmol/L), or even suboxic (DO: 0 – 9 mg/L) or dysoxic (DO: 9 – 90 µmol/L) (Tyson and Pearson, 1991).

In the water column, the trend of lower salinities (and respectively enhanced CH_4) on DO was pronounced (see fig. 21, r^2 = -0.84). While HSW water displayed average values of 294 µmol/kg (DO) and 2.29 nmol/kg (CH_4), MIW water masses were at 352.1 µmol/kg (DO) with enhanced CH_4 of an average of 5.7 nmol/kg. This was also reflected in the average AOU (see fig. 22). While the HSW showed an average AOU of 27.5 µmol/kg, the MIW with enhanced CH_4 only displayed AOU of 8.6 µmol/kg, indicating higher respiration rates in HSW. This points towards a link between meltwater, productivity, and CH_4 concentration. However, DO was in a range where high methanogenic outputs would not be expected as anaerobic methanogenesis is inhibited at such oxygen levels (Jarrell, 1985; Zitomer and Shrout, 1998).

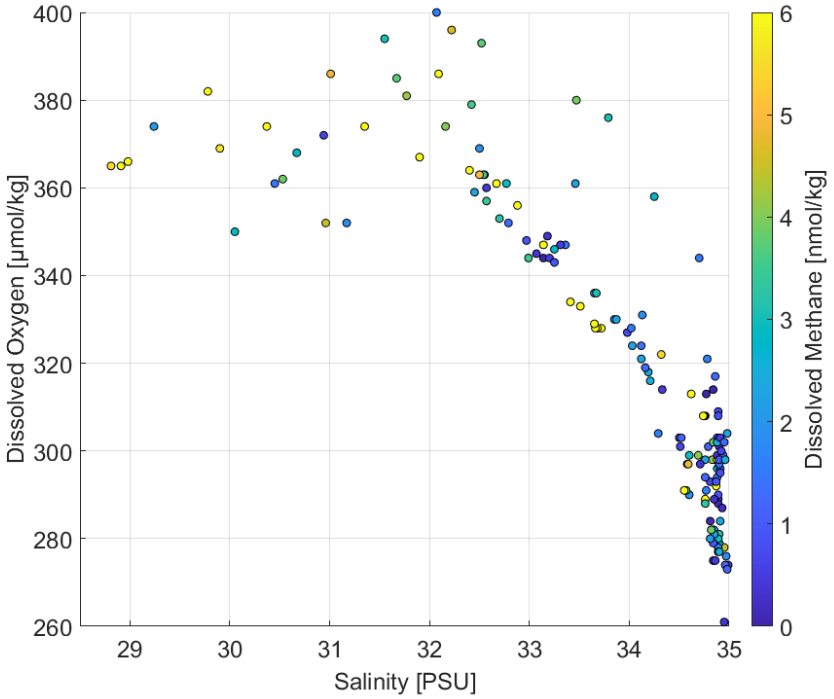

Figure 21: Scatterplot of salinity, dissolved oxygen [µmol/kg], and dissolved methane [nmol/kg] in the water column of the EGS.

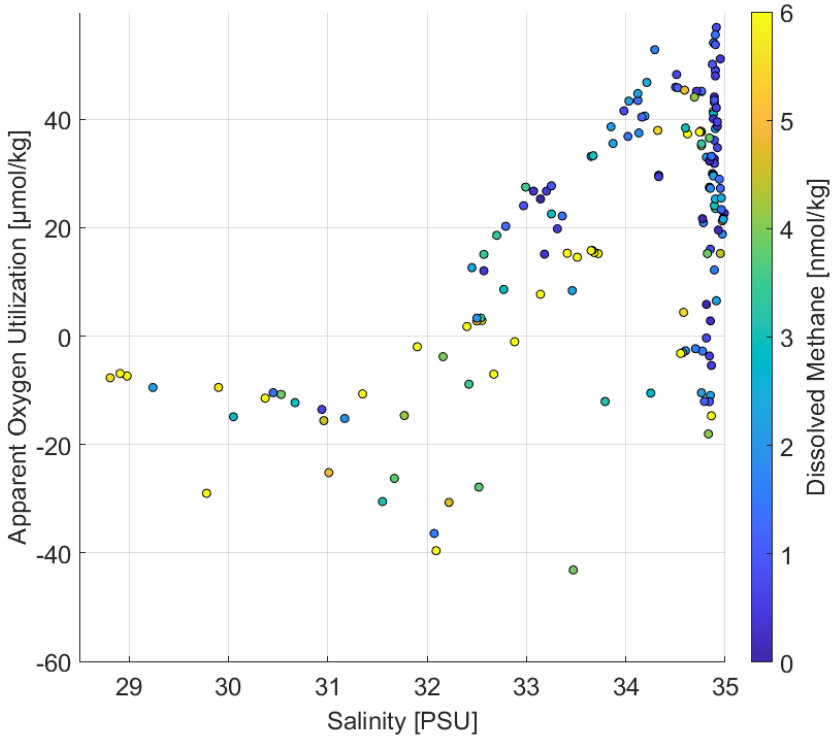

Figure 22: Scatterplot of salinity, apparent oxygen utilization [µmol/kg], and dissolved methane [nmol/kg] in the water column of the EGS.

6.4.3 Nutrients and Nutrient Ratios

Regarding the distribution of nutrients in the surface layer of the study site, nitrate (NO_3^-) displayed the highest values at the southernmost station (6.56 µM) at 63.1 °N and the lowest values at the northernmost station (0.05 µM) at 77.5 °N. Additionally, a strong increasing surface gradient from coast to open ocean could be observed. The lowest values at the coast were 0.32 µM while the values in the open ocean at the same latitude were at 4.73 µM. Generally, the NO_3^- concentrations ranged between 0.047 and 7.299 µM with an average value of 1.9 µM for the entire study site. The low-ranging coastal values correlate with low-density water (MWI), especially at the outlet of the Scoresbysund as well as south of it, indicating low nitrate associated meltwater. Phosphate (PO_4^{3-}) ranged between 0.049 and 0.577 µM with an average of 0.27 µM for the entire study site. Even though the northernmost station depicts the lowest PO_4^{3-} values of 0.05 µM, no clear regional gradients could be observed. Furthermore, no correlation patterns were found between PO_4^{3-} and meltwater. However, notably high NO_3^- (4.07 µM), and PO_4^{3-} (0.44 µM) were measured at the stations of the outlets of the King Christian X. Land glaciers.

Universally, while HSW generally displayed NO_3^- average values of 10.8 µM, the MIW was significantly more depleted in NO_3^- with an average of 4.5 µM. The difference is not as pronounced for PO_4^{3-}, however, regional differences could still be observed with values of 0.74 µM for the HSW and 0.52 µM for the MIW in the water column. Generally, nutrients were not as depleted compared to the surface. However, nutrient depletion was overall much more pronounced on the shelf compared to the open ocean and was strongest near the coast.

Low N:P ratios which here are used as an indicator for nutrient limitation, indicate a clear correlation with meltwater influence ($r^2 = 0.83$). Surface water masses with densities below $\sigma_T = 26.5$ kg/m³ (MIW) showed an average ratio of 2.2:1 (mol N/mol P) and point towards N-limitation. On the other hand, the HSW surface layer of the study site generally displayed a trend towards the Redfield ratio (16:1) with N:P being 10:1, indicating that N-limitation is not as strict and is comparable to Arctic source water which displays typical N:P ratios from 11-16:1 (Sakshaug, 2004). The lesser limitation of nitrate in the HSW was also coinciding with lowered levels of DO, indicating that respiration with regards to primary production may have been higher in these water masses. This also coincides with a strong relationship between negative AOU and low N:P ratios. For N:P < 6:1, AOU averaged -14.66 µmol/kg, indicating that in-situ respiration could influence N-limitation.

At depth, the strict correlation between N:P, MIW, and CH_4 is even more pronounced compared to the surface (see fig. 23). Saline water clustered around the Redfield ratio of 16:1 (N:P) with 14.2:1 (N:P) while the HIW in the water column displayed a Redfield ratio of 7.87:1 (N:P). By extension, CH_4 correlates with the N:P ratios where the HSW and MIW displayed average CH_4 of 2.3 nmol/kg and 5.72 nmol/kg, respectively.

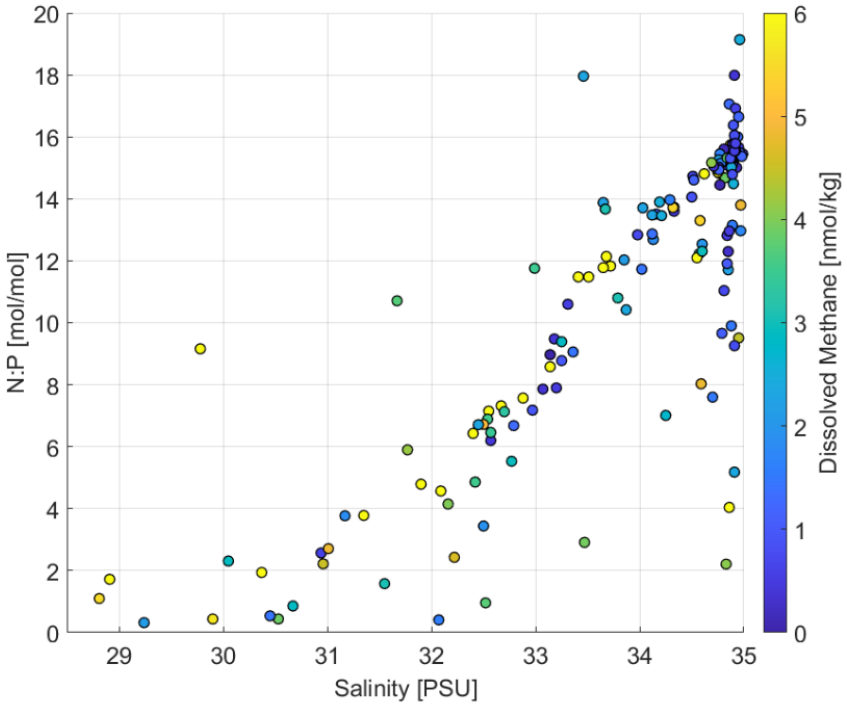

Figure 23: Scatterplot of salinity, N:P ratio [mol/mol], and dissolved CH_4 [nmol/kg] in the water column of the EGS.

6.4.4 Dissolved and Particulate Organic Carbon

Dissolved Organic Carbon (DOC) averaged 78.47 ±10.61 µM (range: 59.18 – 116.66 µM) at depth on the stations where CH_4 was also sampled (see fig. 24). The saline water masses averaged 68.41 ±5.5 µM compared to 84.41 ±8.12 µM which could indicate that C uptake might be higher or C release lower in the SEAS compared to the NEAS. However, carbon cycling is a complex process and thus further studies would need to be undertaken in order to confirm this suggestion. A depth-related comparison was not feasible due to the sparsity of data points.

Particulate Organic Carbon (POC) averaged 51.09 ±50.49 µM (range: 7 – 366.8 µM) at the profiles where CH_4 was also measured. The saline water masses averaged 50.83 ±72 µM compared to 51.09 ±33.2 µM under meltwater influence, showing that no major disparities of POC could be observed regarding the more and less saline water masses. A depth-related comparison was not feasible due to the sparsity of data points.

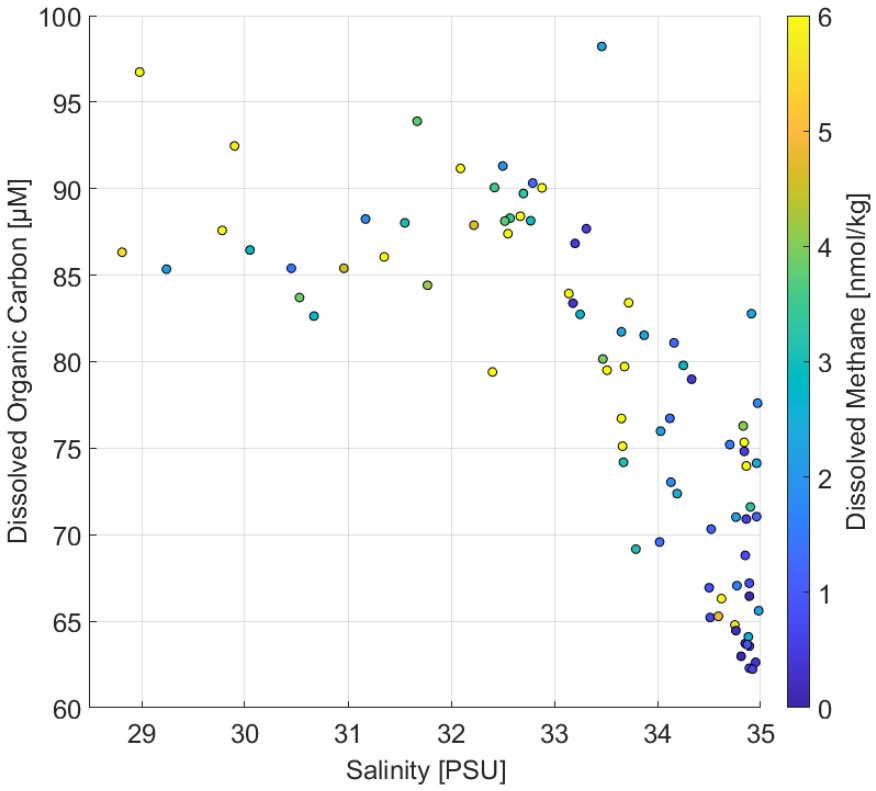

Figure 24: Scatterplot of salinity, dissolved organic carbon [µM], and dissolved CH_4 [nmol/kg] in the water column of the EGS.

6.4.5 Chl-α and Turbidity

Chl-α does not show great variability towards meltwater influence at depth. While water column MIW on the shelf averaged 0.52 ±0.51 µg/L, the HSW was at 0.438 ±0.809 µg/L which is in a similar magnitude. Overall, Chl-α averaged 0.447 ±0.713 µg/L (range: 0.02 – 5.69 µg/L) for the entire study site. However, the light-flooded mixed layer (< 70 m) naturally displayed increased values of 1 ±0.713 µg/L which is also a common range for the Arctic and Subarctic (Sakshaug, 2004). A comparison of the mixed layer on the NEAS (average Chl-α: 0.632 ±0.414 µg/L) to the SEAS (average Chl-α: 1.521 ±0.921 µg/L) illuminates great disparities between these regions and reflects significantly higher productivity in the surface mixed layer in the South. The outlier station 30 is associated with slightly increased amounts of Chl-α (1.81 µg/L).

Overall, turbidity averaged 0.865 ±1.347 NTU (range: 0.15 – 7.99 NTU). The difference in both regions is again reflected in this parameter. The HIW averaged about 1.285 ±1.809 NTU while the HSW was at 0.486 ±0.471 NTU. This situation is expected as meltwater is often associated with entrainment of detritus in suspension either by convective processes in calving glacier fronts or by transport via ice floes as ice-rafted debris (IRD; Andrews et al., 2014; Kuijpers et al., 2013; Vermassen et al., 2019). However, it must be noted that turbidity is influenced by other factors, e.g., the amount of POC in suspension, as well.

6.4.6 Biogeochemical Implications

In the previously undertaken analysis of biogeochemical parameters of the EGS water masses, great disparities could be illuminated between meltwater-influenced seawater mainly found in the NEAS and saline seawater in the SEAS.

The MIW was typically associated with enhanced CH_4 compared to the HSW. Even though the study site was well-oxygenated, DO was more restricted in the saline water whereas AOU displayed higher oxygen consumption compared to lower consumption and even partial oxygen production under the influence of meltwater. Regions with MIW displayed strong N-limitation compared to no observed nutrient restrictions in the HSW. This nutrient limitation is a common feature for ice-melt-influenced waters during summer (Henley et al., 2020; Ko et al., 2020; Mills et al., 2018). Adjacent to Greenland this is further amplified by the melt of the GrIS because surface run-off induces N-depleted meltwater into the oceanic water column. However, N-enriched subglacial discharge partially balances the local marine N budget. Marine-terminating glaciers that are producing these plumes are experiencing strong rates of landward retreat and might vanish in the future which potentially amplifies N-limitation near the Greenland coast (Hopwood et al., 2018).

These correlations are indicative for the NEAS displaying water masses in a post-bloom stage which is a typical setting for a water column after the retreat of sea ice. Generally, sea ice cover during winter accompanied by the winter darkness inhibits photosynthesis and shifts phytoplankton into a resting stage where growth and respiration rates are at their lowest (Sakshaug and Andresen, 1986) while nutrients become enriched relative to the number of consumers. Spring marks the onset of the melting season. When the overlaying sea ice melts, irradiance to the sea surface increases, enabling photosynthesis as sea ice can attenuate irradiance down to 0.25 – 3.5 % of the surface PAR (Sakshaug, 2004). PAR describes the **p**hotosynthetically **a**vailable **r**adiation which is the total irradiance at a wavelength of 400 – 700 nm. The sudden exposure to light during spring melt causes intense but short-lived phytoplankton blooms, especially at the ice edge where they can form a 20 – 100 km wide belt (Niebauer et al., 1995). Meanwhile, melting ice establishes a strongly stratified layer in the upper 15 – 35 m (Sakshaug, 2004). These two factors cause a post-bloom phase characterized by strong nutrient depletion in the surface layer during summer as observed in this work. Additionally, upward replenishment of nutrients is inhibited by the pronounced pycnocline. In the Icelandic Sea and the Irminger Sea, the bloom peaks in late May to early June; in the subarctic waters north of Iceland the spring bloom culminates in late March to late April (Sakshaug, 2004). The post-bloom situation is further implied by the availability of DO and the smaller oxygen consumption as well as strongly decreased Chl-α in the mixed layer on the NEAS compared to the SEAS surface waters indicate

that productivity at the time of sampling was reduced to a minimum possibly due to the N-limitation. This is further reflected in the greater availability of a substrate (DOC) compared to the SEAS, indicating, that carbon (C) is not the factor limiting productivity and that C uptake might be lower in the NEAS. However, no measurements concerning C uptake rates were available for this work. Arctic-derived surface water is characterized by two modes (Jones et al., 1998). Water originated in the Atlantic (Håvik et al., n.d.) is typically nitrate and phosphate co-limited while water of Pacific origin is typically nitrate-limited (Damm et al., 2010; Yamamoto-Kawai et al., 2006). The latter is caused by water masses passing through the Bering and Chukchi Sea for several months (Woodgate et al., 2005) which are sites of pronounced denitrification (Tanaka et al., 2004; Taylor et al., 2003). Associating this fact with the data of this work, it is likely that the EGS Arctic-derived water had its origin in the Pacific. However, this can only be viewed as a vague indicator as further investigation would need to be undertaken, such as tracer experiments. The fact that already N-deficient water may have entered the shelf area which was then mixed with depleted post-bloom meltwater may explain the strong N-limitation in the NEAS.

6.5 Synthesis

While it may be considered contradicting to find high amounts of dissolved CH_4 in a well-oxygenated water column, it is a common occurrence (Bange et al., 1994; Forster et al., 2009; Li et al., 2020a; Repeta et al., 2016; Scranton and Brewer, 1977) and has even been reported for the Arctic Seas (Damm et al., 2015b). This phenomenon, commonly called "the methane paradox", is yet not fully understood. Several approaches to explain this process have been proposed and eventually, a combination of all of them likely contribute to the budget of aerobic methanogenesis (Weber et al., 2019).

A frequent approach is to explain it by micro-niches. The intestinal tracts of zooplankton and other marine animals (Schmale et al., 2018), as well as fecal pellets and other types of particular organic matter suspended in the water column act as a reducing micro-environment enabling a pathway for anaerobic methanogenesis in oxygen-rich waters (Tilbrook and Karl, 1995).

Additionally, CH_4 may be produced under aerobic conditions as a byproduct during the decomposition of methyl-phosphonate (MPn) (Carini et al., 2014; Karl et al., 2008; Taenzer et al., 2020). While P is incorporated into essential compounds such as proteins and nucleic acids according to the needs of the primary producers (Sakshaug, 2004), CH_4 is released (Kamat et al., 2013) during MPn utilization (Kamat et al., 2013). However, during this study, no P-limitation was observed, and at stations indicating possible N and P co-limitation, no trend regarding the concentration of dissolved CH_4 could be identified. Thus, this mechanism is unlikely to contribute to CH_4 production in the surface waters of the study site.

Li et al. (2020) argue that the photoproduction of CH_4 could be a significant contributor to enhanced CH_4 in oxygenated waters. Colored dissolved organic matter (CDOM) is a byproduct of decaying detritus which may produce CH_4 during photochemical transformation. No CDOM data was available for this study. However, comparisons between DOC and CH_4 generally show vague trends, making this a possible but questionable pathway.

In this study, enhanced values of dissolved CH_4 were correlated with meltwater in a situation where the hydrographic setting displayed a post-bloom seasonal stage under N-limitation. This observation is at par with observations from the Arctic Ocean where enhanced CH_4 was also linked to aerobic N-limited surface waters (Damm et al., 2010). The authors propose a new metabolic pathway for CH_4 production in oligotrophic conditions that are characterized by sufficient P-supply. During this pathway, primary producers may compensate N-depletion by N_2 fixation which is depicted in an amplification of the *nifH* gene. In such an environment where hydrogen is produced by nitrogenases, CH_4 may be formed through the utilization of methylated compounds by *Eubacteria*. Furthermore, it is postulated, that DMSP may serve as a C source for

growth during demethylation and thus may act as a precursor for CH_4 formation in nitrate-stressed environments.

Ubiquitously, CH_4 profiles commonly display a bimodal behavior showing high values at the surface mixed layer with the highest values mostly between 0 – 70 m water depth as well as at the bottom layer and decreased values in the intermediate water column.

CH_4 enhancement in the surface most likely (partially) originates from processes associated with meltwater from sea ice (as described in *6.4 Analysis with Biogeochemical Parameters*). In the mixed layer, the highest values of dissolved CH_4 are often found at 18 – 30 m. Slightly lowered values above that suggest a CH_4 loss to the atmosphere as well as to CH_4 oxidation. Below this, the CH_4 values depict a sharp drop. Damm et al. (2015a) present a model for the seasonality in CH_4 cycling between sea ice, the surface layer, and the atmosphere which could explain this situation (see fig. 25). During winter, CH_4 may be incorporated into sea ice and inherent brine channels. At this time, the interaction between the air and the sea is largely inhibited by a thick ice cap and deep convection in the mixed layer may entrain CH_4 saturated brine into the deeper part of the mixed layer. During summer, meltwater causes a pronounced haline stratification, inhibiting convection with the deeper mixed layer from winter, isolating and effectively storing the dissolved CH_4 in these parts. The breakup of the ice cap and exposure to the sea-air interface then allows the CH_4 excess in the top of the surface layer to equilibrate to atmospheric values. These findings are similar to the CH_4 values of surface waters being near-equilibrium with the atmosphere and enhanced CH_4 in the mixed layer in this study during summer, which is why I

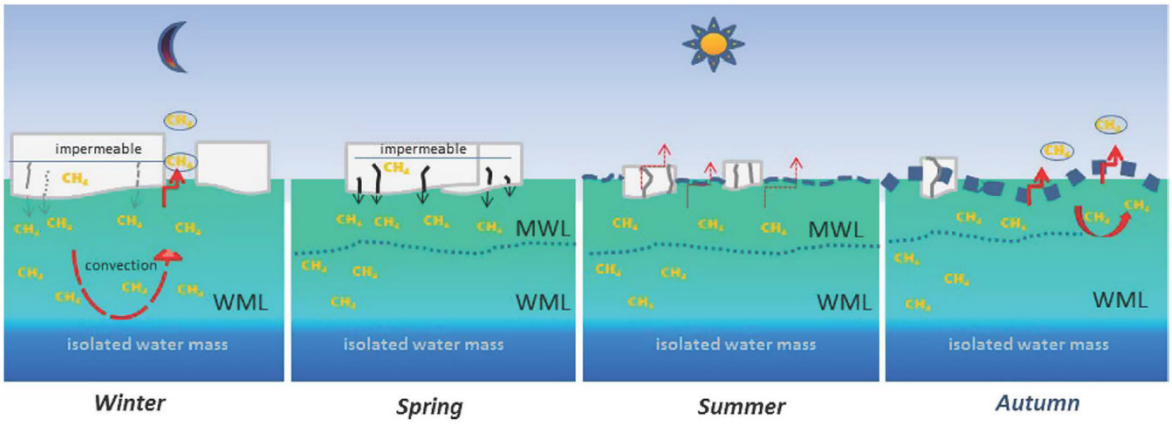

Figure 25: **Seasonal differences in methane cycling between sea ice, surface water, and atmosphere**. In **winter** deep convection transports brine, charged with methane, into the winter mixed layer. Methane efflux may occur by convection in leads, while efflux through impermeable sea ice is restricted. In **spring**, basal melting starts and transports methane (dissolved or re-dissolved gas bubbles) into the shallower meltwater layer. In **summer**, stabilized by thermal stratification and less turbulence, methane remains entrained in both layers. In **autumn**, sea surface temperatures drop, enabling methane efflux by surface water convection. Water masses below the winter mixed layer are not affected by this methane cycling, thus potentially storing them for a longer period (Damm et al., 2015a).

propose an analogous process. However, no time series data is available for this work and thus this should only serve as a suggestion. Further research needs to be conducted to confirm this.

Due to this pronounced density-driven stratification associated with meltwater, the mixed layer and the deeper water column are effectively decoupled and could be considered as two separate systems as vertical mixing must be decreased to a minimum and only occurs in the upper light-flooded 50 m. Below this, biological activity is reduced to a minimum, which is indicated by a change from negative to positive AOU in the upper 30 – 70 m throughout the study site. Negative AOU hereby reflects a situation where oxygen is being produced by photoautotrophs and where it outweighs the consumption of oxygen. Positive AOU on the other hand reflects a situation where aerobic cellular respiration or oxidation of organic matter outweighs the production of oxygen by photosynthesis. This situation is accompanied by a release of nutrients through the degradation of organic matter which is also displayed by the nutrient distribution for the EGS water column (see *appendix A fig. 27 & 28*).

In general, primary productivity is either limited by the availability of carbon, light, nutrients, and/or the temperature distribution. In this study, the limiting factor for the low productivity in the deeper water column most likely stems from low availability of carbon, as stratification most likely enhances remineralization in the mixed layer and reduces export production of organic matter to deeper parts. Furthermore, light limitation at depth might have been influenced by the partial sea ice cover, turbid seas during storm events or arctic sea fog which was a common occurrence in sea ice influenced waters during the sampling campaign - especially near the coast. Hence, due to these conditions, aerobic biological CH_4 production is also unfavored throughout the water column and anaerobic CH_4 production can also be excluded due to the well-oxygenated water column throughout the entire study site. This leads to the conclusion, that locally enhanced CH_4 in the intermediate water column was probably not produced in-situ but was rather advected from other sources. These may be sedimentary sources either by diffusive fluxes from CH_4 saturated porewater or by ebullition of bubbles which then get redissolved in the water column. Methane seeps have been extensively documented for the Arctic region (Åström et al., 2018; Ferré et al., 2020; Hong et al., 2018; Jansson et al., 2019; Westbrook et al., 2009).

The increasing CH_4 surface gradient towards the coast as well as the relationship between CH_4 and meltwater is indicative for a partial land-derived influence on the CH_4 budget of the surface layer. These land-derived sources could either be glacial run-off by subglacial discharge of marine-terminating glaciers, or surface run-off from land-terminating glaciers with short discharge distances to the ocean and respective river-discharge, shallow groundwater discharge, or processes regarding land-fast sea ice. Ultimately, it is a process influenced or induced by the GrIS melt, and confirmatory, the lowest salinities were recorded throughout the coast in this study.

Glacial run-off may have a significant influence on enhanced CH_4 at coastal stations and would lead to pronounced local effects of CH_4. Indeed, there are two reports on elevated CH_4 in subglacial meltwater discharge during melting season in land-terminating systems and the authors argue that this process is applicable for the entirety of the Arctic (Dieser et al., 2014; Lamarche-Gagnon et al., 2019; Meire et al., 2017). Microbial methanogenesis may occur in anoxic subglacial sediments (Boyd et al., 2010). If CH_4 saturated meltwater is present, it is obvious that CH_4 export and meltwater discharge is highly dependent on the hydrological setting, e.g., rate, spatial and temporal variations of discharge, and would be highest during summer melt (Alexander et al., 2013; Davison et al., 2019; Wadham et al., 2010). Subglacial meltwater streams may be supplied by basal melt (Alexander et al., 2013) and/or down migrating meltwater from surface run-off or perennial fern aquifers through crevasses and cracks (Miller et al., 2020). They are occasionally amplified by outburst events induced by rapid supraglacial lake drainage to the glacier bed due to hydrofracturing (Bartholomew et al., 2011; Davison et al., 2019). However, CH_4 fluxes are not a pervasive feature of Arctic glaciers as shown for several field sites in southwest Greenland (Webster et al., 2015) which is why further investigations are vital for the contribution assessment of Arctic glaciers to the global CH_4 budget.

Additionally, it is plausible that submarine groundwater discharge, which was identified as a major global contributor to the coastal input of nutrients and solvents (Luijendijk et al., 2020), may alter the coastal CH_4 distribution. Glacial meltwater has been reported to feed local proglacial aquifers (Levy et al., 2015; Ó Dochartaigh et al., 2019; Vincent et al., 2019) which in turn is connected to submarine groundwater discharge on Greenland's continental shelf (DeFoor et al., 2011). While CH_4 transport through submarine groundwater discharge has not been reported for Greenland, it has been observed at two sites in the North Pacific and the Arctic Ocean, respectively (Lecher et al., 2016).

Near the bottom, three distinct features can be observed:

(1) No enhanced CH_4 near the bottom,

(2) enhanced CH_4 on the deepest stations in near vicinity to the seafloor,

(3) enhanced CH_4 above bottom depth surrounded by decreased CH_4 above and below it.

While the first case (1) displays a situation with no CH_4 in-situ production or advection from other sources, (2) enhanced CH_4 on the seafloor indicates a sedimentary source of CH_4. The third scenario (3) includes advection of water masses and will be further discussed in the following chapter. Causes for the second case (2) can be anoxic sediments characterized by prominent methanogenesis. CH_4 reaches the water column by diffusion and then disperses and migrates by

lateral as well as horizontal mixing and is being reduced by AOM. Rysgaard et al. (1998) report on sedimentary anaerobic respiration in a high-arctic fjord system (average depth of 100 m) on the EGS with an oxygen penetration depth of just 1 cm into the seafloor. Here, respiration rates displayed a seasonality pattern dependent on ice coverage and were highest during the break-up and retreat of sea ice due to enhanced microbial activity. While methanogenesis was not reported, significant rates of Fe-, SO_4-reduction and denitrification were observed. The authors state that roughly 48 % of deposited carbon was preserved during burial due to high sedimentation rates of 0.09 g dry weight sediment/cm² yr. This carbon could serve as a substrate for anoxic respiration (e.g., methanogenesis) in seafloor sediments. Along with the reported sedimentary anoxia and anaerobic respiration proposed by the authors, I propose a similar possible pathway for CH_4 in coastal areas on the EGS with similar depths either by in-situ microbial methanogenesis or by providing a passage for deeper formed CH_4 either by microbial or thermogenic sources. Smith et al. (2002) state that sediment mass accumulation rates on the EGS for the last 100 yrs were in the same order at 0.09 g/cm² yr and additionally observed rates in selected Greenlandic fjord systems to be as high as 0.43 g/cm² yr near the outlet of the fjords where sediment transport distances are short. Therefore, carbon burial as a source for substrate during methanogenesis is also plausible for the shelf in similar depths. However, remineralization of carbon could hamper its supply and subsequent burial in deeper water. Additionally, sediment cores from the outer EGS display relatively low organic carbon between 0.1 – 0.8 % contrary to other sediments related to glacial advances in the eastern Arctic (Nam et al., 1995; Stein et al., 1994), suggesting that sediments in the deeper water column might not be a suitable location for in-situ methanogenesis. Another possible source for enhanced bottom CH_4 may be thawing permafrost (Shakhova et al., 2015; Steinbach et al., 2021) as indicated by enhanced bottom temperatures in the SEAS in this study. Subsea permafrost is defined as seafloor material that remains at or below 0 °C for two or more consecutive years (Angelopoulos et al., 2019; van Everdingen and (USA), 1998) and thus higher average temperatures, as well as higher temperature variabilities in the SEAS as observed in this study, would favor increased subsea permafrost thaw and inherent release of CH_4 to the water column. The current global permafrost map reported on marginal amounts of permafrost in the SEAS with low fractions of permafrost in the overburden and small areas of continuous permafrost with low fractions of permafrost in the NEAS (Brown et al., 2002). This situation arises from the fact that the EGS was mostly not exposed during the Last Glacial Maximum which is considered preliminary for permafrost deposit accumulation (Lindgren et al., 2016; Overduin et al., 2019a). However, mappings of subsea permafrost are usually created via calculations and models by means of bathymetry, global sea-level rise, and geothermal boundary conditions and commonly not by in-situ measurements (Heginbottom, 2002; Overduin et al., 2019b; Sherman et al., 2017). Thus, permafrost maps might show great disparities to the actual conditions encountered in the Arctic and are subject to error. Overduin et al. (2019b) estimate the submarine

permafrost extent in the Greenland Sea to 3,000 km² and state that the 0 °C isotherm which is required for permafrost to persist, lies at an average depth of 53 m (range: 1 – 299 m) which is within the range of depth on the SEAS.

7 Conclusion

To answer the two leading questions which are mentioned in *4 Objectives*, four objectives were set in this work. The following findings were revealed regarding these objectives:

(1) Overall, the CH_4 concentration in the water column of the EGS was 3.74 ±2.35 nmol/kg which is unexpected as the entire environment was well-oxygenated at the time of sampling. The highest surface CH_4 concentrations were observed near the coast which was inherent with the presence of meltwater as observed in the salinity and density distribution. The surface water on the shelf break exhibited intermediate CH_4 concentrations and the open ocean the lowest values, respectively. At depth, the average CH_4 concentration was nearly uniform for the shelf area compared to low concentrations in the Greenland, Iceland, and Irminger Sea as well as the Iceland shelf. However, the CH_4 distribution displayed a bimodal behavior throughout the water column with higher CH_4 in the surface mixed layer as well as the bottom waters and low CH_4 in intermediate water. The shallow maximum originates either from in-situ production, amplification by seasonal carryover through storage with regards to ice-formation, or by advective processes from other sources. Loss occurs through oxidation and escape at the sea-air-boundary as well as removal by southbound transport through the EGC. The deep maximum on the other hand arises from sedimentary processes or advection from other sources.

(2) Great disparities in several biogeochemical parameters were revealed with regards to their influence of meltwater. Enhanced CH_4 concentrations were linked to the influence of meltwater which was characterized by nitrogen-limitation, minimal oxygen uptake, low Chl-α, and enhanced DOC indicating low-local production and reflecting a post-bloom situation typical for the time of sampling in sea ice influenced regions. The presented situation is conformable to the findings of Damm et al. (2010) who suggested that N-limitation might be compensated by N_2-fixation of *Eubacteria* under the utilization of methylated compounds and CH_4 release as a byproduct.

(3) The high coastal CH_4 concentrations could be indicative for a terrigenous source or input of a parameter that amplifies coastal CH_4 production, or it could display advection of CH_4-enhanced waters by the EGCC, even though the EGCC could not be distinguished from the EGC in this work. Meltwater which influences CH_4 on the EGS originates from three endmembers and likely resembles a mixture between them, but however, is subject to spatial and temporal variability. These endmembers are in-situ sea ice melt, glacial run-off, or supply by meltwater from the Arctic source water. However, these endmembers and their amount of influence could not be differentiated.

(4) During the 2019 melt season (July – August) the surface layer of the EGS was largely in equilibrium with the atmosphere (101.18 %) and thus sea-air fluxes were in a minor magnitude with overall -0.11 ±1.52 µmol/m²/s, proving that the region was neither a source nor sink for atmospheric CH_4.

In conclusion, the leading questions were successfully answered. The distribution was thoroughly elaborated in the frame of the available resources for this study. A significant link between enhanced CH_4 concentrations and meltwater was identified which lays the foundation for further investigations in the polar and subpolar regions under the aspect of ice melt with regards to CH_4 cycling in the water column.

8 Outlook

The link between enhanced CH_4 in meltwater identified in this work poses potential future implications under the aspect of a projected increase in melting rate of the GrIS as well as the retreating Arctic sea ice extent. At the time of sampling, the EGS represented neither a source nor sink. However, with increased future meltwater volumes which displayed enhanced CH_4 compared to open ocean water, this suggests that the EGS contingently could turn into a source for atmospheric CH_4. Nonetheless, this sampling campaign represents a single timeframe and the lack of knowledge about the CH_4 distribution on the subpolar EGS prior to this work complicates implications regarding future developments. Furthermore, the distribution of CH_4 is influenced by many other factors which need to be assessed and knowledge about oceanic CH_4 cycling in polar and subpolar regions needs to be consolidated in order to support this claim.

The most crucial aspect to predict the future development of oceanic CH_4 concentrations in the Arctic and its impact on the global climate is to increase sampling in these regions: the spatial regional resolution needs to be increased to identify large scale processes from local anomalies and an increased temporal sampling resolution (e.g., installations of time-series stations) can reveal seasonal variations. Special attention should be put on distinguishing the magnitude of influence between sea- and land-derived meltwater (e.g., $\delta^{18}O$ or ^{228}Ra-fluxes) to identify possible sources for CH_4. I suggest using more sensitive and less error-prone measurement techniques which can help to produce more reliable high-frequent data, such as off-axis integrated cavity output spectroscopy (OA-ICOS) and non-dispersive infrared detection (NDIR) coupled to a Weiss-type equilibrator for concentration measurements or novel eddy covariance techniques to quantify sea-air fluxes (Arévalo-Martínez et al., 2013; Kroon et al., 2007; Mahesh et al., 2015).

A higher vertical and horizontal sampling resolution is important as it impeded identifying CH_4 pathways in the water column in this work. Additionally to this, sedimentary porewater measurements of dissolved CH_4 could help to identify sedimentary sources and isotopic measurements of ^{14}C-CH_4 would help to distinguish between biogenic and geogenic CH_4 sources. Another essential aspect is the identification and classification of biogenic producers by molecular genetics and biomarker analysis in the water column and the sediments to attribute CH_4 production and consumption to specific communities. Concomitant with this is the quantification of oxidation rates (e.g., through incubation experiments with ^{14}C-labeled compounds) to differentiate between sources and sinks for in-situ production and gauge travel distances of dissolved CH_4 in the water column.

This study should serve as a foundation of knowledge about CH_4 cycling on the subpolar EGS to improve future work on the impact of oceanic CH_4 on a local and to some extent on a global level and ameliorate implementations of actions aimed at preserving the already fragile Arctic.

9 Acknowledgments

I would like to thank the captain and crew of RV MARIA S. MERIAN for their work under various challenging conditions. Furthermore, I want to thank Christian Mertens, Insa Rapp, and Alba Filella for providing CTD, nutrient, and carbon data. A special thanks goes to Hermann Bange and Damian Arévalo-Martínez for their supervision and extensive support and trust in my work as well as giving me the opportunity to conduct research in such an interesting field. I highly appreciate that I could use the laboratory as well as the onboard equipment of WG Bange for my work.

I want to cordially thank you, Linda, Lina, Isa, and Martin, for proofreading this work and for your numerous suggestions and help with the use of programs as well as scientific discussions.

Lastly, I want to thank my family as well as my partner Frederike, and all of my friends for all the support. I really appreciate that I can always rely on you - no matter what!

10 References

Aagaard, K. and Carmack, E. C.: The role of sea ice and other fresh water in the Arctic circulation, J. Geophys. Res. Ocean., 94(C10), 14485–14498, doi:https://doi.org/10.1029/JC094iC10p14485, 1989.

Aagaard, K. and Coachman, L. K.: The East Greenland Current North of Denmark Strait: Part I, Arctic, 21(3), 181–200 [online] Available from: http://www.jstor.org/stable/40507537, 1968.

Alexander, D. J., Davies, T. R. H. and Shulmeister, J.: Basal melting beneath a fast-flowing temperate tidewater glacier, Ann. Glaciol., 54(63), 265–271, doi:DOI: 10.3189/2013AoG63A259, 2013.

Andrews, J. T., Bigg, G. R. and Wilton, D. J.: Holocene ice-rafting and sediment transport from the glaciated margin of East Greenland (67–70°N) to the N Iceland shelves: detecting and modelling changing sediment sources, Quat. Sci. Rev., 91, 204–217, doi:https://doi.org/10.1016/j.quascirev.2013.08.019, 2014.

de Angelis, M. A. and Lee, C.: Methane production during zooplankton grazing on marine phytoplankton, Limnol. Oceanogr., 39(6), 1298–1308, doi:https://doi.org/10.4319/lo.1994.39.6.1298, 1994.

Angelopoulos, M., Westermann, S., Overduin, P., Faguet, A., Olenchenko, V., Grosse, G. and Grigoriev, M. N.: Heat and Salt Flow in Subsea Permafrost Modeled with CryoGRID2, J. Geophys. Res. Earth Surf., 124(4), 920–937, doi:https://doi.org/10.1029/2018JF004823, 2019.

von Appen, W.-J., Koszalka, I. M., Pickart, R. S., Haine, T. W. N., Mastropole, D., Magaldi, M. G., Valdimarsson, H., Girton, J., Jochumsen, K. and Krahmann, G.: The East Greenland Spill Jet as an important component of the Atlantic Meridional Overturning Circulation, Deep Sea Res. Part I Oceanogr. Res. Pap., 92, 75–84, doi:https://doi.org/10.1016/j.dsr.2014.06.002, 2014.

Arévalo-Martínez, D. L., Beyer, M., Krumbholz, M., Piller, I., Kock, A., Steinhoff, T., Körtzinger, A. and Bange, H. W.: A new method for continuous measurements of oceanic and atmospheric N_2O, CO and CO_2: performance of off-axis integrated cavity output spectroscopy (OA-ICOS) coupled to non-dispersive infrared detection (NDIR), Ocean Sci., 9(6), 1071–1087, doi:10.5194/os-9-1071-2013, 2013.

Åström, E. K. L., Carroll, M. L., Ambrose Jr., W. G., Sen, A., Silyakova, A. and Carroll, J.: Methane cold seeps as biological oases in the high-Arctic deep sea, Limnol. Oceanogr., 63(S1), S209–S231, doi:https://doi.org/10.1002/lno.10732, 2018.

Bacon, S., Reverdin, G., Rigor, I. G. and Snaith, H. M.: A freshwater jet on the east Greenland

shelf, J. Geophys. Res. Ocean., 107(C7), 5–16, doi:https://doi.org/10.1029/2001JC000935, 2002.

Bamber, J., van den Broeke, M., Ettema, J., Lenaerts, J. and Rignot, E.: Recent large increases in freshwater fluxes from Greenland into the North Atlantic, Geophys. Res. Lett., 39(19), doi:https://doi.org/10.1029/2012GL052552, 2012.

Bange, H. W., Bartell, U. H., Rapsomanikis, S. and Andreae, M. O.: Methane in the Baltic and North Seas and a reassessment of the marine emissions of methane, Global Biogeochem. Cycles, 8(4), 465–480, doi:https://doi.org/10.1029/94GB02181, 1994.

Bange, H. W., Arévalo-Martínez, D. L., de la Paz, M., Farías, L., Kaiser, J., Kock, A., Law, C. S., Rees, A. P., Rehder, G., Tortell, P. D., Upstill-Goddard, R. C. and Wilson, S. T.: A Harmonized Nitrous Oxide (N2O) Ocean Observation Network for the 21st Century , Front. Mar. Sci. , 6, 157 [online] Available from: https://www.frontiersin.org/article/10.3389/fmars.2019.00157, 2019.

Barnes, R. O. and Goldberg, E. D.: Methane production and consumption in anoxic marine sediments, Geology, 4(5), 297–300, doi:10.1130/0091-7613(1976)4<297:MPACIA>2.0.CO;2, 1976.

Bartholomew, I., Nienow, P., Sole, A., Mair, D., Cowton, T., Palmer, S. and Wadham, J.: Supraglacial forcing of subglacial drainage in the ablation zone of the Greenland Ice Sheet, Geophys. Res. Lett., 38, doi:10.1029/2011GL047063, 2011.

Battaglia, G. and Joos, F.: Marine N2O Emissions From Nitrification and Denitrification Constrained by Modern Observations and Projected in Multimillennial Global Warming Simulations, Global Biogeochem. Cycles, 32(1), 92–121, doi:https://doi.org/10.1002/2017GB005671, 2018.

Boyd, E. S., Skidmore, M., Mitchell, A. C., Bakermans, C. and Peters, J. W.: Methanogenesis in subglacial sediments, Environ. Microbiol. Rep., 2(5), 685–692, doi:https://doi.org/10.1111/j.1758-2229.2010.00162.x, 2010.

Brown, J., Ferrians Jr., O. J., Heginbottom, J. A. and Melnikov, E. S.: Circum-Arctic map of permafrost and ground-ice conditions, 2nd ed., 2002.

Carini, P., White, A. E., Campbell, E. O. and Giovannoni, S. J.: Methane production by phosphate-starved SAR11 chemoheterotrophic marine bacteria, Nat. Commun., 5(1), 4346, doi:10.1038/ncomms5346, 2014.

Cavalieri, D. J. and Parkinson, C. L.: Arctic sea ice variability and trends, 1979–2010, Cryosph., 6(4), 881–889, doi:10.5194/tc-6-881-2012, 2012.

Charlou, J. L., Fouquet, Y., Bougault, H., Donval, J. P., Etoubleau, J., Jean-Baptiste, P., Dapoigny, A., Appriou, P. and Rona, P. A.: Intense CH4 plumes generated by serpentinization of ultramafic rocks at the intersection of the 15°20′N fracture zone and the Mid-Atlantic Ridge, Geochim. Cosmochim. Acta, 62(13), 2323–2333, doi:https://doi.org/10.1016/S0016-7037(98)00138-0, 1998.

Chen, J. L., Wilson, C. R. and Tapley, B. D.: Satellite Gravity Measurements Confirm Accelerated Melting of Greenland Ice Sheet, Science (80-.)., 313(5795), 1958 LP – 1960, doi:10.1126/science.1129007, 2006.

Chen, Y.-H. and Prinn, R. G.: Estimation of atmospheric methane emissions between 1996 and 2001 using a three-dimensional global chemical transport model, J. Geophys. Res. Atmos., 111(D10), doi:https://doi.org/10.1029/2005JD006058, 2006.

Chylek, P., Folland, C. K., Lesins, G., Dubey, M. K. and Wang, M.-Y.: Arctic air temperature change amplification and the Atlantic multidecadal oscillation, Geophys. Res. Lett., 36, 2009.

Chylek, P., Folland, C. K., Lesins, G. and Dubey, M. K.: Twentieth century bipolar seesaw of the Arctic and Antarctic surface air temperatures, Geophys. Res. Lett., 37(8), doi:https://doi.org/10.1029/2010GL042793, 2010.

Comiso, J. C.: Large Decadal Decline of the Arctic Multiyear Ice Cover, J. Clim., 25(4), 1176–1193, doi:10.1175/JCLI-D-11-00113.1, 2012.

Cox, D. R., Huuse, M., Newton, A. M. W., Sarkar, A. D. and Knutz, P. C.: Shallow gas and gas hydrate occurrences on the northwest Greenland shelf margin, Mar. Geol., 432, 106382, doi:https://doi.org/10.1016/j.margeo.2020.106382, 2021.

Crabeck, O., Delille, B., Thomas, D., Geilfus, N.-X., Rysgaard, S. and Tison, J.-L.: CO2 and CH4 in sea ice from a subarctic fjord under influence of riverine input, Biogeosciences, 11, 6525–6538, doi:10.5194/bg-11-6525-2014, 2014.

Dai, A., Luo, D., Song, M. and Liu, J.: Arctic amplification is caused by sea-ice loss under increasing CO2, Nat. Commun., 10(1), 121, doi:10.1038/s41467-018-07954-9, 2019.

Damm, E., Kiene, R. P., Schwarz, J., Falck, E. and Dieckmann, G.: Methane cycling in Arctic shelf water and its relationship with phytoplankton biomass and DMSP, Mar. Chem., 109(1), 45–59, doi:https://doi.org/10.1016/j.marchem.2007.12.003, 2008.

Damm, E., Helmke, E., Thoms, S., Schauer, U., Nöthig, E., Bakker, K. and Kiene, R. P.: Methane production in aerobic oligotrophic surface water in the central Arctic Ocean, Biogeosciences, 7(3), 1099–1108, doi:10.5194/bg-7-1099-2010, 2010.

Damm, E., Thoms, S., Kattner, G., Beszczynska-Möller, A., Nöthig, E. M. and Stimac, I.:

Coexisting methane and oxygen excesses in nitrate-limited polar water (Fram Strait) during ongoing sea ice melting, Biogeosciences Discuss., 2011, 5179–5195, doi:10.5194/bgd-8-5179-2011, 2011.

Damm, E., Rudels, B., Schauer, U., Mau, S. and Dieckmann, G.: Methane excess in Arctic surface water- triggered by sea ice formation and melting, Sci. Rep., 5(1), 16179, doi:10.1038/srep16179, 2015a.

Damm, E., Thoms, S., Beszczynska-Möller, A., Nöthig, E. M. and Kattner, G.: Methane excess production in oxygen-rich polar water and a model of cellular conditions for this paradox, Polar Sci., 9(3), 327–334, doi:https://doi.org/10.1016/j.polar.2015.05.001, 2015b.

Davison, B. J., Sole, A. J., Livingstone, S. J., Cowton, T. R. and Nienow, P. W.: The Influence of Hydrology on the Dynamics of Land-Terminating Sectors of the Greenland Ice Sheet , Front. Earth Sci. , 7, 10, 2019.

DeFoor, W., Person, M., Larsen, H., Lizarralde, D., Cohen, D. and Dugan, B.: Ice sheet-derived submarine groundwater discharge on Greenland's continental shelf, Water Resour. Res., 47, doi:10.1029/2011WR010536, 2011.

DelSontro, T., McGinnis, D. F., Wehrli, B. and Ostrovsky, I.: Size Does Matter: Importance of Large Bubbles and Small-Scale Hot Spots for Methane Transport, Environ. Sci. Technol., 49(3), 1268–1276, doi:10.1021/es5054286, 2015.

Dickson, R., Rudels, B., Dye, S., Karcher, M., Meincke, J. and Yashayaev, I.: Current estimates of freshwater flux through Arctic and subarctic seas, Prog. Oceanogr., 73(3), 210–230, doi:https://doi.org/10.1016/j.pocean.2006.12.003, 2007.

Dieser, M., Broemsen, E. L. J. E., Cameron, K. A., King, G. M., Achberger, A., Choquette, K., Hagedorn, B., Sletten, R., Junge, K. and Christner, B. C.: Molecular and biogeochemical evidence for methane cycling beneath the western margin of the Greenland Ice Sheet, ISME J., 8(11), 2305–2316, doi:10.1038/ismej.2014.59, 2014.

Dlugokencky, E.: Trends in Atmospheric Methane - Global CH4 Monthly Means, NOAA/GML, 2021.

Dlugokencky, E. J., Houweling, S., Bruhwiler, L., Masarie, K. A., Lang, P. M., Miller, J. B. and Tans, P. P.: Atmospheric methane levels off: Temporary pause or a new steady-state?, Geophys. Res. Lett., 30(19), doi:https://doi.org/10.1029/2003GL018126, 2003.

Dodd, P. A., Heywood, K. J., Meredith, M. P., Naveira-Garabato, A. C., Marca, A. D. and Falkner, K. K.: Sources and fate of freshwater exported in the East Greenland Current, Geophys. Res. Lett., 36(19), doi:https://doi.org/10.1029/2009GL039663, 2009.

Dorsey, N. E.: Properties of Ordinary Water-Substance in all its phases: water-vapor, water, and all the ices. Compiled by N.E. Dorsey., Reinhold Publishing Corporation, New York., 1940.

Drewry, D.: Remote Sensing for Polar Regions - Remote Sensing Ice and Snow. D. K. Hall and J. Martinec 1985. London, New York, Chapman and Hall. 189 p, illustrated, hard cover. ISBN 0 412 25910 9., Polar Rec. (Gr. Brit)., 23(143), 213–214, doi:DOI: 10.1017/S0032247400028503, 1986.

Etiope, G., Fridriksson, T., Winiwarter, W. and Theloke, J.: Natural emissions of methane from geothermal and volcanic sources in Europe, J. Volcanol. Geotherm. Res., 165, 76–86, doi:10.1016/j.jvolgeores.2007.04.014, 2007.

Etminan, M., Myhre, G., Highwood, E. J. and Shine, K. P.: Radiative forcing of carbon dioxide, methane, and nitrous oxide: A significant revision of the methane radiative forcing, Geophys. Res. Lett., 43(24), 12,612-614,623, doi:https://doi.org/10.1002/2016GL071930, 2016.

van Everdingen, R. O. and (USA), I. P. A.: Multi-language Glossary of Permafrost and Related Ground-ice Terms in Chinese, English, French, German ..., Arctic Inst. of North America University of Calgary. [online] Available from: https://books.google.de/books?id=ZaLPXwAACAAJ, 1998.

Fenwick, L., Capelle, D., Damm, E., Zimmermann, S., Williams, W. J., Vagle, S. and Tortell, P. D.: Methane and nitrous oxide distributions across the North American Arctic Ocean during summer, 2015, J. Geophys. Res. Ocean., 122(1), 390–412, doi:https://doi.org/10.1002/2016JC012493, 2017.

Ferré, B., Jansson, P. G., Moser, M., Serov, P., Portnov, A., Graves, C. A., Panieri, G., Gründger, F., Berndt, C., Lehmann, M. F. and Niemann, H.: Reduced methane seepage from Arctic sediments during cold bottom-water conditions, Nat. Geosci., 13(2), 144–148, doi:10.1038/s41561-019-0515-3, 2020.

Feseker, T., Boetius, A., Wenzhöfer, F., Blandin, J., Olu, K., Yoerger, D. R., Camilli, R., German, C. R. and de Beer, D.: Eruption of a deep-sea mud volcano triggers rapid sediment movement, Nat. Commun., 5(1), 5385, doi:10.1038/ncomms6385, 2014.

Florez-Leiva, L., Damm, E. and Farías, L.: Methane production induced by dimethylsulfide in surface water of an upwelling ecosystem, Prog. Oceanogr., 112–113, 38–48, doi:https://doi.org/10.1016/j.pocean.2013.03.005, 2013.

Foldvik, A., Aagaard, K. and Tørresen, T.: On the velocity field of the East Greenland Current, Deep Sea Res. Part A. Oceanogr. Res. Pap., 35(8), 1335–1354, doi:https://doi.org/10.1016/0198-0149(88)90086-6, 1988.

Forster, G., Upstill-Goddard, R., Gist, N., Robinson, C., Uher, G. and Woodward, E.: Nitrous oxide and methane in the Atlantic Ocean between 50°N and 52°S: Latitudinal distribution and sea-to-air flux, Deep Sea Res. Part II Top. Stud. Oceanogr., 964–976, doi:10.1016/j.dsr2.2008.12.002, 2009.

Foukal, N. P., Gelderloos, R. and Pickart, R. S.: A continuous pathway for fresh water along the East Greenland shelf, Sci. Adv., 6(43), eabc4254, doi:10.1126/sciadv.abc4254, 2020.

Geissler, W. H., Pulm, P. V, Jokat, W. and Gebhardt, A. C.: Indications for the Occurrence of Gas Hydrates in the Fram Strait from Heat Flow and Multichannel Seismic Reflection Data, edited by M. Giustiniani, J. Geol. Res., 2014, 582424, doi:10.1155/2014/582424, 2014.

GISTEMP-Team: GISS Surface Temperature Analysis (GISTEMP), version 4. NASA Goddard Institute for Space Studies., [online] Available from: https://data.giss.nasa.gov/gistemp/, 2021.

Gülzow, W., Gräwe, U., Kedzior, S., Schmale, O. and Rehder, G.: Seasonal variation of methane in the water column of Arkona and Bornholm Basin, western Baltic Sea, J. Mar. Syst., 139, 332–347, doi:https://doi.org/10.1016/j.jmarsys.2014.07.013, 2014.

Hansen, J., Sato, M. and Ruedy, R.: Radiative forcing and climate response, J. Geophys. Res. Atmos., 102(D6), 6831–6864, doi:https://doi.org/10.1029/96JD03436, 1997.

Hanson, R. S. and Hanson, T. E.: Methanotrophic bacteria, Microbiol. Rev., 60(2), 439–471 [online] Available from: https://pubmed.ncbi.nlm.nih.gov/8801441, 1996.

Haroon, M. F., Hu, S., Shi, Y., Imelfort, M., Keller, J., Hugenholtz, P., Yuan, Z. and Tyson, G. W.: Anaerobic oxidation of methane coupled to nitrate reduction in a novel archaeal lineage, Nature, 500(7464), 567–570, doi:10.1038/nature12375, 2013.

Håvik, L., Pickart, R. S., Våge, K., Torres, D., Thurnherr, A. M., Beszczynska-Möller, A., Walczowski, W. and von Appen, W.-J.: Evolution of the East Greenland Current from Fram Strait to Denmark Strait: Synoptic measurements from summer 2012, J. Geophys. Res. Ocean., 122(3), 1974–1994, doi:https://doi.org/10.1002/2016JC012228, 2017.

Håvik, L., Almansi, M., Våge, K. and Haine, T. W. N.: Atlantic-Origin Overflow Water in the East Greenland Current, J. Phys. Oceanogr., 49(9), 2255–2269, doi:10.1175/JPO-D-18-0216.1, n.d.

Heginbottom, J. A.: Permafrost mapping: a review, Prog. Phys. Geogr. Earth Environ., 26(4), 623–642, doi:10.1191/0309133302pp355ra, 2002.

Hendry, K. R., Huvenne, V. A. I., Robinson, L. F., Annett, A., Badger, M., Jacobel, A. W., Ng, H. C., Opher, J., Pickering, R. A., Taylor, M. L., Bates, S. L., Cooper, A., Cushman, G. G., Goodwin, C., Hoy, S., Rowland, G., Samperiz, A., Williams, J. A., Achterberg, E. P.,

Arrowsmith, C., Alexander Brearley, J., Henley, S. F., Krause, J. W., Leng, M. J., Li, T., McManus, J. F., Meredith, M. P., Perkins, R. and Woodward, E. M. S.: The biogeochemical impact of glacial meltwater from Southwest Greenland, Prog. Oceanogr., 176, 102126, doi:https://doi.org/10.1016/j.pocean.2019.102126, 2019.

Henley, S. F., Porter, M., Hobbs, L., Braun, J., Guillaume-Castel, R., Venables, E. J., Dumont, E. and Cottier, F.: Nitrate supply and uptake in the Atlantic Arctic sea ice zone: seasonal cycle, mechanisms and drivers, Philos. Trans. R. Soc. A Math. Phys. Eng. Sci., 378(2181), 20190361, doi:10.1098/rsta.2019.0361, 2020.

Henry, W. and Banks, J.: III. Experiments on the quantity of gases absorbed by water, at different temperatures, and under different pressures, Philos. Trans. R. Soc. London, 93, 29–274, doi:10.1098/rstl.1803.0004, 1803.

Holm, N. G., Oze, C., Mousis, O., Waite, J. H. and Guilbert-Lepoutre, A.: Serpentinization and the Formation of H2 and CH4 on Celestial Bodies (Planets, Moons, Comets), Astrobiology, 15(7), 587–600, doi:10.1089/ast.2014.1188, 2015.

Hong, W.-L., Torres, M. E., Portnov, A., Waage, M., Haley, B. and Lepland, A.: Variations in Gas and Water Pulses at an Arctic Seep: Fluid Sources and Methane Transport, Geophys. Res. Lett., 45(9), 4153–4162, doi:https://doi.org/10.1029/2018GL077309, 2018.

Hopcroft, P. O., Valdes, P. J., O'Connor, F. M., Kaplan, J. O. and Beerling, D. J.: Understanding the glacial methane cycle, Nat. Commun., 8(1), 14383, doi:10.1038/ncomms14383, 2017.

Hopwood, M. J., Carroll, D., Browning, T. J., Meire, L., Mortensen, J., Krisch, S. and Achterberg, E. P.: Non-linear response of summertime marine productivity to increased meltwater discharge around Greenland, Nat. Commun., 9(1), 3256, doi:10.1038/s41467-018-05488-8, 2018.

Huang, R., Sun, W., Liu, J., Ding, X., Peng, S. and Zhan, W.: The H2/CH4 ratio during serpentinization cannot reliably identify biological signatures, Sci. Rep., 6(1), 33821, doi:10.1038/srep33821, 2016.

Intergovernmental Panel on Climate Change, Ed.: Carbon and Other Biogeochemical Cycles, in Climate Change 2013 – The Physical Science Basis: Working Group I Contribution to the Fifth Assessment Report of the Intergovernmental Panel on Climate Change, pp. 465–570, Cambridge University Press, Cambridge., 2014a.

Intergovernmental Panel on Climate Change: Climate Change 2013 – The Physical Science Basis: Working Group I Contribution to the Fifth Assessment Report of the Intergovernmental

Panel on Climate Change, Cambridge University Press, Cambridge., 2014b.

Intergovernmental Panel on Climate Change, Ed.: Observations: Atmosphere and Surface, in Climate Change 2013 – The Physical Science Basis: Working Group I Contribution to the Fifth Assessment Report of the Intergovernmental Panel on Climate Change, pp. 159–254, Cambridge University Press, Cambridge., 2014c.

Jähne, B., Heinz, G. and Dietrich, W.: Measurement of the diffusion coefficients of sparingly soluble gases in water, J. Geophys. Res. Ocean., 92(C10), 10767–10776, doi:https://doi.org/10.1029/JC092iC10p10767, 1987.

Jansson, P., Triest, J., Grilli, R., Ferré, B., Silyakova, A., Mienert, J. and Chappellaz, J.: High-resolution underwater laser spectrometer sensing provides new insights into methane distribution at an Arctic seepage site, Ocean Sci., 15(4), 1055–1069, doi:10.5194/os-15-1055-2019, 2019.

Jarrell, K. F.: Extreme Oxygen Sensitivity in Methanogenic Archaebacteria, Bioscience, 35(5), 298–302, doi:10.2307/1309929, 1985.

Johnson, J., Mienert, J., Plaza, A., Vadakkepuliyambatta, S., Knies, J., Bünz, S., Andreassen, K. and Ferre, B.: Abiotic methane from ultraslow-spreading ridges can charge Arctic gas hydrates, Geology, 43, 371–374, doi:10.1130/G36440.1, 2015.

Jones, E. P., Anderson, L. G. and Swift, J. H.: Distribution of Atlantic and Pacific waters in the upper Arctic Ocean: Implications for circulation, Geophys. Res. Lett., 25, 765–768, doi:10.1029/98GL00464, 1998.

Justus, C. G. and Mikhail, A.: Height variation of wind speed and wind distributions statistics, Geophys. Res. Lett., 3(5), 261–264, doi:https://doi.org/10.1029/GL003i005p00261, 1976.

Kamat, S. S., Williams, H. J., Dangott, L. J., Chakrabarti, M. and Raushel, F. M.: The catalytic mechanism for aerobic formation of methane by bacteria, Nature, 497(7447), 132–136, doi:10.1038/nature12061, 2013.

Karl, D. M., Beversdorf, L., Björkman, K. M., Church, M. J., Martinez, A. and Delong, E. F.: Aerobic production of methane in the sea, Nat. Geosci., 1(7), 473–478, doi:10.1038/ngeo234, 2008.

Killops, S. and Killops, V.: Long-Term Fate of Organic Matter in the Geosphere, Introd. to Org. Geochemistry, 117–165, doi:https://doi.org/10.1002/9781118697214.ch4, 2004.

Klein, F., Grozeva, N. G. and Seewald, J. S.: Abiotic methane synthesis and serpentinization in olivine-hosted fluid inclusions, Proc. Natl. Acad. Sci., 116(36), 17666 LP – 17672, doi:10.1073/pnas.1907871116, 2019.

Klitzke, P., Luzi-Helbing, M., Schicks, J. M., Cacace, M., Jacquey, A. B., Sippel, J., Scheck-Wenderoth, M. and Faleide, J. I.: Gas Hydrate Stability Zone of the Barents Sea and Kara Sea Region, Energy Procedia, 97, 302–309, doi:https://doi.org/10.1016/j.egypro.2016.10.005, 2016.

Ko, E., Gorbunov, M. Y., Jung, J., Joo, H. M., Lee, Y., Cho, K.-H., Yang, E. J., Kang, S.-H. and Park, J.: Effects of Nitrogen Limitation on Phytoplankton Physiology in the Western Arctic Ocean in Summer, J. Geophys. Res. Ocean., 125(11), e2020JC016501, doi:https://doi.org/10.1029/2020JC016501, 2020.

Kock, A.: Methane measurements in selected ocean areas: Eastern tropical North Atlantic Ocean and southwestern Labrador Sea (Diplomarbeit), Christian-Albrechts-Universität Kiel., 2007.

Kock, A. and Bange, H. W.: Counting the ocean's greenhouse gas emissions, Eos (Washington. DC)., 96, 10–13, doi:10.1029/2015EO023665, 2015.

Kroon, P. S., Hensen, A., Jonker, H. J. J., Zahniser, M. S., van 't Veen, W. H. and Vermeulen, A. T.: Suitability of quantum cascade laser spectroscopy for CH4 and N2O eddy covariance flux measurements, Biogeosciences, 4(5), 715–728, doi:10.5194/bg-4-715-2007, 2007.

Kudo, K., Yamada, K., Toyoda, S., Yoshida, N., Sasano, D., Kosugi, N., Ishii, M., Yoshikawa-Inoue, H., Murata, A., Uchida, H. and Nishino, S.: Spatial distribution of dissolved methane and its source in the western Arctic Ocean, J. Oceanogr., 74, doi:10.1007/s10872-017-0460-y, 2018.

Kuijpers, A., Knutz, P. and Moros, M.: Ice-Rafted Debris (IRD) BT - Encyclopedia of Marine Geosciences, edited by J. Harff, M. Meschede, S. Petersen, and J. Thiede, pp. 1–7, Springer Netherlands, Dordrecht., 2013.

Kwok, R., Cunningham, G. F. and Pang, S. S.: Fram Strait sea ice outflow, J. Geophys. Res. Ocean., 109(C1), doi:https://doi.org/10.1029/2003JC001785, 2004.

Lamarche-Gagnon, G., Wadham, J. L., Sherwood Lollar, B., Arndt, S., Fietzek, P., Beaton, A. D., Tedstone, A. J., Telling, J., Bagshaw, E. A., Hawkings, J. R., Kohler, T. J., Zarsky, J. D., Mowlem, M. C., Anesio, A. M. and Stibal, M.: Greenland melt drives continuous export of methane from the ice-sheet bed, Nature, 565(7737), 73–77, doi:10.1038/s41586-018-0800-0, 2019.

Lecher, A. L., Kessler, J., Sparrow, K., Garcia-Tigreros Kodovska, F., Dimova, N., Murray, J., Tulaczyk, S. and Paytan, A.: Methane transport through submarine groundwater discharge to the North Pacific and Arctic Ocean at two Alaskan sites, Limnol. Oceanogr., 61(S1), S344–S355, doi:https://doi.org/10.1002/lno.10118, 2016.

Lee, S.-Y. and Holder, G. D.: Methane hydrates potential as a future energy source, Fuel

Process. Technol., 71(1), 181–186, doi:https://doi.org/10.1016/S0378-3820(01)00145-X, 2001.

Lee, S.: A theory for polar amplification from a general circulation perspective, Asia-Pacific J. Atmos. Sci., 50(1), 31–43, doi:10.1007/s13143-014-0024-7, 2014.

Lee, S., Gong, T., Johnson, N., Feldstein, S. B. and Pollard, D.: On the Possible Link between Tropical Convection and the Northern Hemisphere Arctic Surface Air Temperature Change between 1958 and 2001, J. Clim., 24(16), 4350–4367, doi:10.1175/2011JCLI4003.1, 2011.

Lenssen, N. J. L., Schmidt, G. A., Hansen, J. E., Menne, M. J., Persin, A., Ruedy, R. and Zyss, D.: Improvements in the GISTEMP Uncertainty Model, J. Geophys. Res. Atmos., 124(12), 6307–6326, doi:https://doi.org/10.1029/2018JD029522, 2019.

Levasseur, M., Gosselin, M. and Michaud, S.: A new source of dimethylsulfide (DMS) for the arctic atmosphere: ice diatoms, Mar. Biol., 121(2), 381–387, doi:10.1007/BF00346748, 1994.

Levy, A., Robinson, Z., Krause, S., Waller, R. and Weatherill, J.: Long-term variability of proglacial groundwater-fed hydrological systems in an area of glacier retreat, Skeiðarársandur, Iceland, Earth Surf. Process. Landforms, 40(7), 981–994, doi:https://doi.org/10.1002/esp.3696, 2015.

Li, W., Dore, J. E., Steigmeyer, A. J., Cho, Y.-J., Kim, O.-S., Liu, Y., Morgan-Kiss, R. M., Skidmore, M. L. and Priscu, J. C.: Methane production in the oxygenated water column of a perennially ice-covered Antarctic lake, Limnol. Oceanogr., 65(1), 143–156, doi:https://doi.org/10.1002/lno.11257, 2020a.

Li, Y., Fichot, C. G., Geng, L., Scarratt, M. G. and Xie, H.: The Contribution of Methane Photoproduction to the Oceanic Methane Paradox, Geophys. Res. Lett., 47(14), e2020GL088362, doi:https://doi.org/10.1029/2020GL088362, 2020b.

Lindgren, A., Hugelius, G., Kuhry, P., Christensen, T. R. and Vandenberghe, J.: GIS-based Maps and Area Estimates of Northern Hemisphere Permafrost Extent during the Last Glacial Maximum, Permafr. Periglac. Process., 27(1), 6–16, doi:https://doi.org/10.1002/ppp.1851, 2016.

Liu, J., Chen, Z., Francis, J., Song, M., Mote, T. and Hu, Y.: Has Arctic Sea Ice Loss Contributed to Increased Surface Melting of the Greenland Ice Sheet?, J. Clim., 29(9), 3373–3386, doi:10.1175/JCLI-D-15-0391.1, 2016.

Lomans, B. P., Op den Camp, H. J. M., Pol, A., van der Drift, C. and Vogels, G. D.: Role of Methanogens and Other Bacteria in Degradation of Dimethyl Sulfide and Methanethiol in Anoxic Freshwater Sediments, Appl. Environ. Microbiol., 65(5), 2116 LP – 2121, doi:10.1128/AEM.65.5.2116-2121.1999, 1999.

Lorenson, T. D., Greinert, J. and Coffin, R. B.: Dissolved methane in the Beaufort Sea and the

Arctic Ocean, 1992–2009; sources and atmospheric flux, Limnol. Oceanogr., 61(S1), S300–S323, doi:https://doi.org/10.1002/lno.10457, 2016.

Loulergue, L., Schilt, A., Spahni, R., Masson-Delmotte, V., Blunier, T., Lemieux, B., Barnola, J.-M., Raynaud, D., Stocker, T. F. and Chappellaz, J.: Orbital and millennial-scale features of atmospheric CH4 over the past 800,000 years, Nature, 453(7193), 383–386, doi:10.1038/nature06950, 2008.

Lovley, D. R., Dwyer, D. F. and Klug, M. J.: Kinetic Analysis of Competition Between Sulfate Reducers and Methanogens for Hydrogen in Sediments, Appl. Environ. Microbiol., 43(6), 1373–1379 [online] Available from: https://aem.asm.org/content/43/6/1373, 1982.

Luijendijk, E., Gleeson, T. and Moosdorf, N.: Fresh groundwater discharge insignificant for the world's oceans but important for coastal ecosystems, Nat. Commun., 11(1), 1260, doi:10.1038/s41467-020-15064-8, 2020.

MacDonald, I. R., Sager, W. W. and Peccini, M. B.: Gas hydrate and chemosynthetic biota in mounded bathymetry at mid-slope hydrocarbon seeps: Northern Gulf of Mexico, Mar. Geol., 198(1), 133–158, doi:https://doi.org/10.1016/S0025-3227(03)00098-7, 2003.

MacFarling Meure, C., Etheridge, D., Trudinger, C., Steele, P., Langenfelds, R., van Ommen, T., Smith, A. and Elkins, J.: Law Dome CO2, CH4 and N2O ice core records extended to 2000 years BP, Geophys. Res. Lett., 33(14), doi:https://doi.org/10.1029/2006GL026152, 2006.

Magen, C., Lapham, L. L., Pohlman, J. W., Marshall, K., Bosman, S., Casso, M. and Chanton, J. P.: A simple headspace equilibration method for measuring dissolved methane, Limnol. Oceanogr. Methods, 12(9), 637–650, doi:https://doi.org/10.4319/lom.2014.12.637, 2014.

Mahesh, P., Sreenivas, G., Rao, P. V. N., Dadhwal, V. K., Sai Krishna, S. V. S. and Mallikarjun, K.: High-precision surface-level CO2 and CH4 using off-axis integrated cavity output spectroscopy (OA-ICOS) over Shadnagar, India, Int. J. Remote Sens., 36(22), 5754–5765, doi:10.1080/01431161.2015.1104744, 2015.

Majorowicz, J. A. and Hannigan, P. K.: Stability Zone of Natural Gas Hydrates in a Permafrost-Bearing Region of the Beaufort—Mackenzie Basin: Study of a Feasible Energy Source1 (Geological Survey of Canada Contribution No.1999275), Nat. Resour. Res., 9(1), 3–26, doi:10.1023/A:1010105628952, 2000.

Malhi, Y., Franklin, J., Seddon, N., Solan, M., Turner, M. G., Field, C. B. and Knowlton, N.: Climate change and ecosystems: threats, opportunities and solutions, Philos. Trans. R. Soc. B Biol. Sci., 375(1794), 20190104, doi:10.1098/rstb.2019.0104, 2020.

Mau, S., Tu, T.-H., Becker, M., dos Santos Ferreira, C., Chen, J.-N., Lin, L.-H., Wang, P.-L.,

Lin, S. and Bohrmann, G.: Methane Seeps and Independent Methane Plumes in the South China Sea Offshore Taiwan, Front. Mar. Sci., 7, 543, doi:10.3389/fmars.2020.00543, 2020.

Mayer, E. W., Blake, D. R., Tyler, S. C., Makide, Y., Montague, D. C. and Rowland, F. S.: Methane: Interhemispheric concentration gradient and atmospheric residence time, Proc. Natl. Acad. Sci. U. S. A., 79(4), 1366–1370, doi:10.1073/pnas.79.4.1366, 1982.

McCollom, T. M. and Donaldson, C.: Generation of Hydrogen and Methane during Experimental Low-Temperature Reaction of Ultramafic Rocks with Water, Astrobiology, 16(6), 389–406, doi:10.1089/ast.2015.1382, 2016.

Meinshausen, M., Smith, S. J., Calvin, K., Daniel, J. S., Kainuma, M. L. T., Lamarque, J.-F., Matsumoto, K., Montzka, S. A., Raper, S. C. B., Riahi, K., Thomson, A., Velders, G. J. M. and van Vuuren, D. P. P.: The RCP greenhouse gas concentrations and their extensions from 1765 to 2300, Clim. Change, 109(1), 213, doi:10.1007/s10584-011-0156-z, 2011.

Meire, L., Mortensen, J., Meire, P., Juul-Pedersen, T., Sejr, M., Rysgaard, S., Nygaard, R., Huybrechts, P. and Meysman, F.: Marine-terminating glaciers sustain high productivity in Greenland fjords, Glob. Chang. Biol., 23, doi:10.1111/gcb.13801, 2017.

Meredith, M., Heywood, K., Dennis, P., Goldson, L., White, R., Fahrbach, E., Schauer, U. and Østerhus, S.: Freshwater fluxes through the Western Fram Strait, Geophys. Res. Lett., 28(8), 1615–1618, doi:https://doi.org/10.1029/2000GL011992, 2001.

Mikkelsen, N., Laier, T., Nielsen, T., Kuijpers, A. and Nørgaard-Pedersen, N.: Methane and possible gas hydrates in the Disko Bugt region, central West Greenland, Geol. Surv. Denmark Greenl. Bull., 26, 69–72, doi:10.34194/geusb.v26.4764, 2012.

Miller, O., Solomon, D. K., Miège, C., Koenig, L., Forster, R., Schmerr, N., Ligtenberg, S. R. M., Legchenko, A., Voss, C. I., Montgomery, L. and McConnell, J. R.: Hydrology of a Perennial Firn Aquifer in Southeast Greenland: An Overview Driven by Field Data, Water Resour. Res., 56(8), e2019WR026348, doi:https://doi.org/10.1029/2019WR026348, 2020.

Mills, M. M., Brown, Z. W., Laney, S. R., Ortega-Retuerta, E., Lowry, K. E., van Dijken, G. L. and Arrigo, K. R.: Nitrogen Limitation of the Summer Phytoplankton and Heterotrophic Prokaryote Communities in the Chukchi Sea , Front. Mar. Sci. , 5, 362 [online] Available from: https://www.frontiersin.org/article/10.3389/fmars.2018.00362, 2018.

Moline, M. A., Karnovsky, N. J., Brown, Z., Divoky, G. J., Frazer, T. K., Jacoby, C. A., Torres, J. J. and Fraser, W. R.: High Latitude Changes in Ice Dynamics and Their Impact on Polar Marine Ecosystems, Ann. N. Y. Acad. Sci., 1134(1), 267–319, doi:https://doi.org/10.1196/annals.1439.010, 2008.

Murrell, J. C.: The Aerobic Methane Oxidizing Bacteria (Methanotrophs) BT - Handbook of Hydrocarbon and Lipid Microbiology, edited by K. N. Timmis, pp. 1953–1966, Springer Berlin Heidelberg, Berlin, Heidelberg., 2010.

Nam, S.-I., Stein, R., Grobe, H. and Hubberten, H.: Late Quaternary glacial-interglacial changes in sediment composition at the East Greenland continental margin and their paleoceanographic implications, Mar. Geol., 122(3), 243–262, doi:https://doi.org/10.1016/0025-3227(94)00070-2, 1995.

Niebauer, H. J., Alexander, V. and Henrichs, S. M.: A time-series study of the spring bloom at the Bering Sea ice edge I. Physical processes, chlorophyll and nutrient chemistry, Cont. Shelf Res., 15(15), 1859–1877, doi:https://doi.org/10.1016/0278-4343(94)00097-7, 1995.

Nisbet, E. G., Manning, M. R., Dlugokencky, E. J., Fisher, R. E., Lowry, D., Michel, S. E., Myhre, C. L., Platt, S. M., Allen, G., Bousquet, P., Brownlow, R., Cain, M., France, J. L., Hermansen, O., Hossaini, R., Jones, A. E., Levin, I., Manning, A. C., Myhre, G., Pyle, J. A., Vaughn, B. H., Warwick, N. J. and White, J. W. C.: Very Strong Atmospheric Methane Growth in the 4 Years 2014–2017: Implications for the Paris Agreement, Global Biogeochem. Cycles, 33(3), 318–342, doi:https://doi.org/10.1029/2018GB006009, 2019.

Ó Dochartaigh, B. É., MacDonald, A. M., Black, A. R., Everest, J., Wilson, P., Darling, W. G., Jones, L. and Raines, M.: Groundwater–glacier meltwater interaction in proglacial aquifers, Hydrol. Earth Syst. Sci., 23(11), 4527–4539, doi:10.5194/hess-23-4527-2019, 2019.

Oliver, H., Luo, H., Castelao, R. M., van Dijken, G. L., Mattingly, K. S., Rosen, J. J., Mote, T. L., Arrigo, K. R., Rennermalm, Å. K., Tedesco, M. and Yager, P. L.: Exploring the Potential Impact of Greenland Meltwater on Stratification, Photosynthetically Active Radiation, and Primary Production in the Labrador Sea, J. Geophys. Res. Ocean., 123(4), 2570–2591, doi:https://doi.org/10.1002/2018JC013802, 2018.

Overduin, P. P., Schneider von Deimling, T., Miesner, F., Grigoriev, M. N., Ruppel, C., Vasiliev, A., Lantuit, H., Juhls, B. and Westermann, S.: Submarine Permafrost Map in the Arctic Modeled Using 1-D Transient Heat Flux (SuPerMAP), J. Geophys. Res. Ocean., 124(6), 3490–3507, doi:https://doi.org/10.1029/2018JC014675, 2019a.

Overduin, P. P., Deimling, T., Miesner, F., Grigoriev, M., Ruppel, C., Alexander, V., Lantuit, H., Juhls, B. and Westermann, S.: Submarine Permafrost Map in the Arctic Modelled Using 1D Transient Heat Flux (SuPerMAP), J. Geophys. Res. Ocean., 124, doi:10.1029/2018JC014675, 2019b.

Pálsson, Ó. K., Gislason, A., Guðfinnsson, H. G., Gunnarsson, B., Ólafsdóttir, S. R., Petursdottir, H., Sveinbjörnsson, S., Thorisson, K. and Valdimarsson, H.: Ecosystem structure

in the Iceland Sea and recent changes to the capelin (Mallotus villosus) population, ICES J. Mar. Sci., 69(7), 1242–1254, doi:10.1093/icesjms/fss071, 2012.

Pape, T., Feseker, T., Kasten, S., Fischer, D. and Bohrmann, G.: Distribution and abundance of gas hydrates in near-surface deposits of the Håkon Mosby Mud Volcano, SW Barents Sea, Geochemistry Geophys. Geosystems - GEOCHEM Geophys GEOSYST, 12, doi:10.1029/2011GC003575, 2011.

Parmentier, F.-J. W., Christensen, T. R., Sørensen, L. L., Rysgaard, S., McGuire, A. D., Miller, P. A. and Walker, D. A.: The impact of lower sea-ice extent on Arctic greenhouse-gas exchange, Nat. Clim. Chang., 3(3), 195–202, doi:10.1038/nclimate1784, 2013.

Pisso, I., Myhre, C. L., Platt, S. M., Eckhardt, S., Hermansen, O., Schmidbauer, N., Mienert, J., Vadakkepuliyambatta, S., Bauguitte, S., Pitt, J., Allen, G., Bower, K. N., O'Shea, S., Gallagher, M. W., Percival, C. J., Pyle, J., Cain, M. and Stohl, A.: Constraints on oceanic methane emissions west of Svalbard from atmospheric in situ measurements and Lagrangian transport modeling, J. Geophys. Res. Atmos., 121(23), 14,114-188,200, doi:https://doi.org/10.1002/2016JD025590, 2016.

Pistone, K., Eisenman, I. and Ramanathan, V.: Radiative Heating of an Ice-Free Arctic Ocean, Geophys. Res. Lett., 46(13), 7474–7480, doi:https://doi.org/10.1029/2019GL082914, 2019.

Platt, S. M., Eckhardt, S., Ferré, B., Fisher, R. E., Hermansen, O., Jansson, P., Lowry, D., Nisbet, E. G., Pisso, I., Schmidbauer, N., Silyakova, A., Stohl, A., Svendby, T. M., Vadakkepuliyambatta, S., Mienert, J. and Lund Myhre, C.: Methane at Svalbard and over the European Arctic Ocean, Atmos. Chem. Phys., 18(23), 17207–17224, doi:10.5194/acp-18-17207-2018, 2018.

Prather, M. J., Holmes, C. D. and Hsu, J.: Reactive greenhouse gas scenarios: Systematic exploration of uncertainties and the role of atmospheric chemistry, Geophys. Res. Lett., 39(9), doi:https://doi.org/10.1029/2012GL051440, 2012.

Punshon, S., Azetsu-Scott, K. and Lee, C. M.: On the distribution of dissolved methane in Davis Strait, North Atlantic Ocean, Mar. Chem., 161, 20–25, doi:https://doi.org/10.1016/j.marchem.2014.02.004, 2014.

Qu, B.: The Impact of Melting Ice on the Ecosystems in Greenland Sea, 1st ed., Springer Berlin Heidelberg., 2015.

Quadfasel, D. and Meincke, J.: Note on the thermal structure of the Greenland Sea gyres, Deep Sea Res. Part A. Oceanogr. Res. Pap., 34(11), 1883–1888, doi:https://doi.org/10.1016/0198-0149(87)90061-6, 1987.

Rahmstorf, S., Box, J. E., Feulner, G., Mann, M. E., Robinson, A., Rutherford, S. and Schaffernicht, E. J.: Exceptional twentieth-century slowdown in Atlantic Ocean overturning circulation, Nat. Clim. Chang., 5(5), 475–480, doi:10.1038/nclimate2554, 2015.

Reeburgh, W. S.: Oceanic methane biogeochemistry, Chem. Rev., 107(2), 486–513, doi:10.1021/cr050362v, 2007.

Rehder, G., Keir, R. S., Suess, E. and Rhein, M.: Methane in the northern Atlantic controlled by microbial oxidation and atmospheric history, Geophys. Res. Lett., 26(5), 587–590, doi:https://doi.org/10.1029/1999GL900049, 1999.

Repeta, D. J., Ferrón, S., Sosa, O. A., Johnson, C. G., Repeta, L. D., Acker, M., DeLong, E. F. and Karl, D. M.: Marine methane paradox explained by bacterial degradation of dissolved organic matter, Nat. Geosci., 9(12), 884–887, doi:10.1038/ngeo2837, 2016.

Rother, M.: Methanogenesis, in Handbook of Hydrocarbon and Lipid Microbiology, vol. 4, p. 447, Springer, Berlin, Heidelberg., 2010.

Rubino, M., Etheridge, D. M., Thornton, D. P., Howden, R., Allison, C. E., Francey, R. J., Langenfelds, R. L., Steele, L. P., Trudinger, C. M., Spencer, D. A., Curran, M. A. J., van Ommen, T. D. and Smith, A. M.: Revised records of atmospheric trace gases CO2, CH4, N2O, and δ13C-CO2 over the last 2000 years from Law Dome, Antarctica, Earth Syst. Sci. Data, 11(2), 473–492, doi:10.5194/essd-11-473-2019, 2019.

Ruddiman, W. F.: The Anthropogenic Greenhouse Era Began Thousands of Years Ago, Clim. Change, 61(3), 261–293, doi:10.1023/B:CLIM.0000004577.17928.fa, 2003.

Rudels, B., Fahrbach, E., Meincke, J., Budéus, G. and Eriksson, P.: The East Greenland Current and its contribution to the Denmark Strait overflow, ICES J. Mar. Sci., 59(6), 1133–1154, doi:10.1006/jmsc.2002.1284, 2002.

Rutgers van der Loeff, M. M., Cassar, N., Nicolaus, M., Rabe, B. and Stimac, I.: The influence of sea ice cover on air-sea gas exchange estimated with radon-222 profiles, J. Geophys. Res. Ocean., 119(5), 2735–2751, doi:https://doi.org/10.1002/2013JC009321, 2014.

Rysgaard, S., Thamdrup, B., Risgaard-Petersen, N., Fossing, H., Berg, P., Christensen, P. B. and Dalsgaard, T.: Seasonal carbon and nutrient mineralization in a high-Arctic coastal marine sediment, Young Sound, Northeast Greenland, Mar. Ecol. Prog. Ser., 175, 261–276 [online] Available from: http://www.jstor.org/stable/24831859, 1998.

Sakshaug, E.: Primary and Secondary Production in the Arctic Seas BT - The Organic Carbon Cycle in the Arctic Ocean, edited by R. Stein and R. W. MacDonald, pp. 57–81, Springer Berlin Heidelberg, Berlin, Heidelberg., 2004.

Sakshaug, E. and Andresen, K.: Effect of light regime upon growth rate and chemical composition of a clone of Skeletonema costatum from the Trondheimsfjord, Norway , J. Plankton Res., 8(4), 619–637, doi:10.1093/plankt/8.4.619, 1986.

Sasakawa, M., Tsunogai, U., Kameyama, S., Nakagawa, F., Nojiri, Y. and Tsuda, A.: Carbon isotopic characterization for the origin of excess methane in subsurface seawater, J. Geophys. Res. Ocean., 113(C3), doi:https://doi.org/10.1029/2007JC004217, 2008.

Sasgen, I., van den Broeke, M., Bamber, J. L., Rignot, E., Sørensen, L. S., Wouters, B., Martinec, Z., Velicogna, I. and Simonsen, S. B.: Timing and origin of recent regional ice-mass loss in Greenland, Earth Planet. Sci. Lett., 333–334, 293–303, doi:https://doi.org/10.1016/j.epsl.2012.03.033, 2012.

Saunois, M., Stavert, A. R., Poulter, B., Bousquet, P., Canadell, J. G., Jackson, R. B., Raymond, P. A., Dlugokencky, E. J., Houweling, S., Patra, P. K., Ciais, P., Arora, V. K., Bastviken, D., Bergamaschi, P., Blake, D. R., Brailsford, G., Bruhwiler, L., Carlson, K. M., Carrol, M., Castaldi, S., Chandra, N., Crevoisier, C., Crill, P. M., Covey, K., Curry, C. L., Etiope, G., Frankenberg, C., Gedney, N., Hegglin, M. I., Höglund-Isaksson, L., Hugelius, G., Ishizawa, M., Ito, A., Janssens-Maenhout, G., Jensen, K. M., Joos, F., Kleinen, T., Krummel, P. B., Langenfelds, R. L., Laruelle, G. G., Liu, L., Machida, T., Maksyutov, S., McDonald, K. C., McNorton, J., Miller, P. A., Melton, J. R., Morino, I., Müller, J., Murguia-Flores, F., Naik, V., Niwa, Y., Noce, S., O'Doherty, S., Parker, R. J., Peng, C., Peng, S., Peters, G. P., Prigent, C., Prinn, R., Ramonet, M., Regnier, P., Riley, W. J., Rosentreter, J. A., Segers, A., Simpson, I. J., Shi, H., Smith, S. J., Steele, L. P., Thornton, B. F., Tian, H., Tohjima, Y., Tubiello, F. N., Tsuruta, A., Viovy, N., Voulgarakis, A., Weber, T. S., van Weele, M., van der Werf, G. R., Weiss, R. F., Worthy, D., Wunch, D., Yin, Y., Yoshida, Y., Zhang, W., Zhang, Z., Zhao, Y., Zheng, B., Zhu, Q., Zhu, Q. and Zhuang, Q.: The Global Methane Budget 2000--2017, Earth Syst. Sci. Data, 12(3), 1561–1623, doi:10.5194/essd-12-1561-2020, 2020.

Savolainen, I., Monni, S. and Syri, S.: THE MITIGATION OF METHANE EMISSIONS FROM INDUSTRIALIZED COUNTRIES CAN EXPLAIN THE ATMOSPHERIC CONCENTRATION LEVEL-OFF, Int. J. Energy a Clean Environ., 10, 193–201, 2009.

Schlichtholz, P. and Houssais, M.-N.: An Investigation of the Dynamics of the East Greenland Current in Fram Strait Based on a Simple Analytical Model, J. Phys. Oceanogr., 29(9), 2240–2265, doi:10.1175/1520-0485(1999)029<2240:AIOTDO>2.0.CO;2, 1999.

Schmale, O., Wäge, J., Mohrholz, V., Wasmund, N., Gräwe, U., Rehder, G., Labrenz, M. and Loick-Wilde, N.: The contribution of zooplankton to methane supersaturation in the oxygenated upper waters of the central Baltic Sea, Limnol. Oceanogr., 63(1), 412–430, doi:https://doi.org/10.1002/lno.10640, 2018.

Scranton, M. I. and Brewer, P. G.: Occurrence of methane in the near-surface waters of the western subtropical North-Atlantic, Deep Sea Res., 24(2), 127–138, doi:https://doi.org/10.1016/0146-6291(77)90548-3, 1977.

Sela-Adler, M., Ronen, Z., Herut, B., Antler, G., Vigderovich, H., Eckert, W. and Sivan, O.: Co-existence of Methanogenesis and Sulfate Reduction with Common Substrates in Sulfate-Rich Estuarine Sediments, Front. Microbiol., 8, 766, doi:10.3389/fmicb.2017.00766, 2017.

Serreze, M. C. and Stroeve, J.: Arctic sea ice trends, variability and implications for seasonal ice forecasting, Philos. Trans. R. Soc. A Math. Phys. Eng. Sci., 373(2045), 20140159, doi:10.1098/rsta.2014.0159, 2015.

Serreze, M. C., Barrett, A. P., Slater, A. G., Woodgate, R. A., Aagaard, K., Lammers, R. B., Steele, M., Moritz, R., Meredith, M. and Lee, C. M.: The large-scale freshwater cycle of the Arctic, J. Geophys. Res. Ocean., 111(C11), doi:https://doi.org/10.1029/2005JC003424, 2006.

Shakhova, N., Semiletov, I. and Panteleev, G.: The distribution of methane on the Siberian Arctic shelves: Implications for the marine methane cycle, Geophys. Res. Lett., 32(9), doi:https://doi.org/10.1029/2005GL022751, 2005.

Shakhova, N., Semiletov, I., Sergienko, V., Lobkovsky, L., Yusupov, V., Salyuk, A., Salomatin, A., Chernykh, D., Kosmach, D., Panteleev, G., Nicolsky, D., Samarkin, V., Joye, S., Charkin, A., Dudarev, O., Meluzov, A. and Gustafsson, O.: The East Siberian Arctic Shelf: towards further assessment of permafrost-related methane fluxes and role of sea ice, Philos. Trans. R. Soc. A Math. Phys. Eng. Sci., 373(2052), 20140451, doi:10.1098/rsta.2014.0451, 2015.

Sharqawy, M. H., Lienhard, J. H. and Zubair, S. M.: Thermophysical properties of seawater: a review of existing correlations and data, Desalin. Water Treat., 16(1–3), 354–380, doi:10.5004/dwt.2010.1079, 2010.

Sherman, D., Kannberg, P. and Constable, S.: Surface towed electromagnetic system for mapping of subsea Arctic permafrost, Earth Planet. Sci. Lett., 460, 97–104, doi:https://doi.org/10.1016/j.epsl.2016.12.002, 2017.

Simpson, I. J., Sulbaek Andersen, M. P., Meinardi, S., Bruhwiler, L., Blake, N. J., Helmig, D., Rowland, F. S. and Blake, D. R.: Long-term decline of global atmospheric ethane concentrations and implications for methane, Nature, 488(7412), 490–494, doi:10.1038/nature11342, 2012.

Singarayer, J., Valdes, P., Friedlingstein, P., Nelson, S. and Beerling, D.: Late Holocene methane rise caused by orbitally controlled increase in tropical sources, Nature, 470, 82–85, doi:10.1038/nature09739, 2011.

Singh, V. P., Singh, P. and Haritashya, U. K., Eds.: Encyclopedia of Snow, Ice and Glaciers, 1st ed., Springer Netherlands., 2011.

Smetacek, V. and Nicol, S.: Polar ocean ecosystems in a changing world, Nature, 437(7057), 362–368, doi:10.1038/nature04161, 2005.

Smith, L., Alexander Clark, J. and Jennings, A.: Accumulation in East Greenland Fjords and on the Continental Shelves Adjacent to the Denmark Strait over the Last Century Based on 210Pb Geochronology, ARCTIC, 55, doi:10.14430/arctic695, 2002.

Solomon, S., Qin, D., Manning, M., Chen, Z., Marquis, M., Averyt, K., Miller, H. L. J. and Tignor, M. M. B.: IPCC, Climate Change 2007: The Physical Science Basis. Contribution of Working Group I to the Fourth Assessment Report of the Intergovernmental Panel on Climate Change, Cambridge, United Kingdom and New York, USA., 2007.

Sowers, T.: Atmospheric methane isotope records covering the Holocene period, Quat. Sci. Rev., 29(1), 213–221, doi:https://doi.org/10.1016/j.quascirev.2009.05.023, 2010.

Spahni, R., Chappellaz, J., Stocker, T. F., Loulergue, L., Hausammann, G., Kawamura, K., Flückiger, J., Schwander, J., Raynaud, D., Masson-Delmotte, V. and Jouzel, J.: Atmospheric Methane and Nitrous Oxide of the Late Pleistocene from Antarctic Ice Cores, Science (80-.)., 310(5752), 1317 LP – 1321, doi:10.1126/science.1120132, 2005.

Stein, R., Grobe, H. and Wahsner, M.: Organic carbon, carbonate, and clay mineral distributions in eastern central Arctic Ocean surface sediments, Mar. Geol., 119(3), 269–285, doi:https://doi.org/10.1016/0025-3227(94)90185-6, 1994.

Steinbach, J., Holmstrand, H., Shcherbakova, K., Kosmach, D., Brüchert, V., Shakhova, N., Salyuk, A., Sapart, C. J., Chernykh, D., Noormets, R., Semiletov, I. and Gustafsson, Ö.: Source apportionment of methane escaping the subsea permafrost system in the outer Eurasian Arctic Shelf, Proc. Natl. Acad. Sci., 118(10), e2019672118, doi:10.1073/pnas.2019672118, 2021.

de Steur, L., Hansen, E., Gerdes, R., Karcher, M., Fahrbach, E. and Holfort, J.: Freshwater fluxes in the East Greenland Current: A decade of observations, Geophys. Res. Lett., 36(23), doi:https://doi.org/10.1029/2009GL041278, 2009.

Stouffer, R. J., Yin, J., Gregory, J. M., Dixon, K. W., Spelman, M. J., Hurlin, W., Weaver, A. J., Eby, M., Flato, G. M., Hasumi, H., Hu, A., Jungclaus, J. H., Kamenkovich, I. V, Levermann, A., Montoya, M., Murakami, S., Nawrath, S., Oka, A., Peltier, W. R., Robitaille, D. Y., Sokolov, A., Vettoretti, G. and Weber, S. L.: Investigating the Causes of the Response of the Thermohaline Circulation to Past and Future Climate Changes, J. Clim., 19(8), 1365–1387, doi:10.1175/JCLI3689.1, 2006.

Sutherland, D. A. and Pickart, R. S.: The East Greenland Coastal Current: Structure, variability, and forcing, Prog. Oceanogr., 78(1), 58–77, doi:https://doi.org/10.1016/j.pocean.2007.09.006, 2008.

Swingedouw, D., Rodehacke, C. B., Behrens, E., Menary, M., Olsen, S. M., Gao, Y., Mikolajewicz, U., Mignot, J. and Biastoch, A.: Decadal fingerprints of freshwater discharge around Greenland in a multi-model ensemble, Clim. Dyn., 41(3), 695–720, doi:10.1007/s00382-012-1479-9, 2013.

Taenzer, L., Carini, P. C., Masterson, A. M., Bourque, B., Gaube, J. H. and Leavitt, W. D.: Microbial Methane From Methylphosphonate Isotopically Records Source, Geophys. Res. Lett., 47(1), e2019GL085872, doi:https://doi.org/10.1029/2019GL085872, 2020.

Tanaka, T., Guo, L., Deal, C., Tanaka, N., Whitledge, T. and Murata, A.: N deficiency in a well-oxygenated cold bottom water over the Bering Sea shelf: Influence of sedimentary denitrification, Cont. Shelf Res., 24, 1271–1283, doi:10.1016/j.csr.2004.04.004, 2004.

Taylor, J., Falkner, K., Schauer, U. and Meredith, M.: Quantitative Considerations of Dissolved Barium as a Tracer in the Arctic Ocean, J. Geophys. Res., 108, doi:10.1029/2002JC001635, 2003.

Tilbrook, B. D. and Karl, D. M.: Methane sources, distributions and sinks from California coastal waters to the oligotrophic North Pacific gyre, Mar. Chem., 49(1), 51–64, doi:https://doi.org/10.1016/0304-4203(94)00058-L, 1995.

Tison, J.-L., Brabant, F., Dumont, I. and Stefels, J.: High-resolution dimethyl sulfide and dimethylsulfoniopropionate time series profiles in decaying summer first-year sea ice at Ice Station Polarstern, western Weddell Sea, Antarctica, J. Geophys. Res. Biogeosciences, 115(G4), doi:https://doi.org/10.1029/2010JG001427, 2010.

Trevena, A. J. and Jones, G. B.: Dimethylsulphide and dimethylsulphoniopropionate in Antarctic sea ice and their release during sea ice melting, Mar. Chem., 98(2), 210–222, doi:https://doi.org/10.1016/j.marchem.2005.09.005, 2006.

Tyson, R. V and Pearson, T. H.: Modern and ancient continental shelf anoxia: an overview, Geol. Soc. London, Spec. Publ., 58(1), 1 LP – 24, doi:10.1144/GSL.SP.1991.058.01.01, 1991.

Våge, K., Pickart, R. S., Sarafanov, A., Knutsen, Ø., Mercier, H., Lherminier, P., van Aken, H. M., Meincke, J., Quadfasel, D. and Bacon, S.: The Irminger Gyre: Circulation, convection, and interannual variability, Deep Sea Res. Part I Oceanogr. Res. Pap., 58(5), 590–614, doi:https://doi.org/10.1016/j.dsr.2011.03.001, 2011.

Vermassen, F., Wangner, D. J., Dyke, L. M., Schmidt, S., Cordua, A. E., Kjær, K. H., Haubner,

K. and Andresen, C. S.: Evaluating ice-rafted debris as a proxy for glacier calving in Upernavik Isfjord, NW Greenland, J. Quat. Sci., 34(3), 258–267, doi:https://doi.org/10.1002/jqs.3095, 2019.

Vincent, A., Violette, S. and Aðalgeirsdóttir, G.: Groundwater in catchments headed by temperate glaciers: A review, Earth-Science Rev., 188, 59–76, doi:https://doi.org/10.1016/j.earscirev.2018.10.017, 2019.

Vitale Brovarone, A., Sverjensky, D. A., Piccoli, F., Ressico, F., Giovannelli, D. and Daniel, I.: Subduction hides high-pressure sources of energy that may feed the deep subsurface biosphere, Nat. Commun., 11(1), 3880, doi:10.1038/s41467-020-17342-x, 2020.

Wadham, J. L., Tranter, M., Skidmore, M., Hodson, A. J., Priscu, J., Lyons, W. B., Sharp, M., Wynn, P. and Jackson, M.: Biogeochemical weathering under ice: Size matters, Global Biogeochem. Cycles, 24(3), doi:https://doi.org/10.1029/2009GB003688, 2010.

Wadham, J. L., Hawkings, J. R., Tarasov, L., Gregoire, L. J., Spencer, R. G. M., Gutjahr, M., Ridgwell, A. and Kohfeld, K. E.: Ice sheets matter for the global carbon cycle, Nat. Commun., 10(1), 3567, doi:10.1038/s41467-019-11394-4, 2019.

Wallmann, K., Pinero, E., Burwicz, E., Haeckel, M., Hensen, C., Dale, A. and Ruepke, L.: The Global Inventory of Methane Hydrate in Marine Sediments: A Theoretical Approach, Energies , 5(7), doi:10.3390/en5072449, 2012.

Wallmann, K., Riedel, M., Hong, W. L., Patton, H., Hubbard, A., Pape, T., Hsu, C. W., Schmidt, C., Johnson, J. E., Torres, M. E., Andreassen, K., Berndt, C. and Bohrmann, G.: Gas hydrate dissociation off Svalbard induced by isostatic rebound rather than global warming, Nat. Commun., 9(1), 83, doi:10.1038/s41467-017-02550-9, 2018.

Walter Anthony, K. M., Anthony, P., Grosse, G. and Chanton, J.: Geologic methane seeps along boundaries of Arctic permafrost thaw and melting glaciers, Nat. Geosci., 5(6), 419–426, doi:10.1038/ngeo1480, 2012.

Wanninkhof, R.: Relationship between wind speed and gas exchange over the ocean revisited, Limnol. Oceanogr. Methods, 12(6), 351–362, doi:https://doi.org/10.4319/lom.2014.12.351, 2014.

Weber, T., Wiseman, N. A. and Kock, A.: Global ocean methane emissions dominated by shallow coastal waters, Nat. Commun., 10(1), 4584, doi:10.1038/s41467-019-12541-7, 2019.

Webster, K. D., White, J. R. and Pratt, L. M.: Ground-Level Concentrations of Atmospheric Methane in Southwest Greenland Evaluated Using Open-Path Laser Spectroscopy and Cavity-Enhanced Absorption Spectroscopy, Arctic, Antarct. Alp. Res., 47(4), 599–609,

doi:10.1657/AAAR0014-051, 2015.

Westbrook, G. K., Thatcher, K. E., Rohling, E. J., Piotrowski, A. M., Pälike, H., Osborne, A. H., Nisbet, E. G., Minshull, T. A., Lanoisellé, M., James, R. H., Hühnerbach, V., Green, D., Fisher, R. E., Crocker, A. J., Chabert, A., Bolton, C., Beszczynska-Möller, A., Berndt, C. and Aquilina, A.: Escape of methane gas from the seabed along the West Spitsbergen continental margin, Geophys. Res. Lett., 36(15), doi:https://doi.org/10.1029/2009GL039191, 2009.

Wiesenburg, D. A. and Guinasso, N. L.: Equilibrium solubilities of methane, carbon monoxide, and hydrogen in water and sea water, J. Chem. Eng. Data, 24(4), 356–360, doi:10.1021/je60083a006, 1979.

Wilbanks, Parry, Canziani, Palutikof, Lankao, Romero, Bao, Berkhout, Cairncross, Ceron, Kapshe, Zapata-Marti and Muir-Wood: Industry, settlement and society. Climate Change 2007: Impacts, Adaptation and Vulnerability. Contribution of Working Group II to the Fourth Assessment Report of the Intergovernmental Panel on Climate Change, M.L. Parry, O.F. Canziani, J.P. Palutikof, P.J, Cambridge, United Kingdom., 2007.

Wilson, S. T., Bange, H. W., Arévalo-Mart\'\inez, D. L., Barnes, J., Borges, A. V, Brown, I., Bullister, J. L., Burgos, M., Capelle, D. W., Casso, M., de la Paz, M., Far\'\ias, L., Fenwick, L., Ferrón, S., Garcia, G., Glockzin, M., Karl, D. M., Kock, A., Laperriere, S., Law, C. S., Manning, C. C., Marriner, A., Myllykangas, J.-P., Pohlman, J. W., Rees, A. P., Santoro, A. E., Tortell, P. D., Upstill-Goddard, R. C., Wisegarver, D. P., Zhang, G.-L. and Rehder, G.: An intercomparison of oceanic methane and nitrous oxide measurements, Biogeosciences, 15(19), 5891–5907, doi:10.5194/bg-15-5891-2018, 2018.

Wood, W. T. and Jung, W. Y.: Modeling the extent of Earth's marine methane hydrate cryosphere, Venue West Conference Services Ltd., Vancouver, BC (Canada), Canada., 2008.

Woodgate, R. A., Aagaard, K. and Weingartner, T. J.: A year in the physical oceanography of the Chukchi Sea: Moored measurements from autumn 1990–1991, Deep Sea Res. Part II Top. Stud. Oceanogr., 52(24), 3116–3149, doi:https://doi.org/10.1016/j.dsr2.2005.10.016, 2005.

Worthy, D., Taylor, C., Dlugokencky, E., Chan, E., Nisbet, E., Laurila, T., Fisher, R., France, J., Lowry, D., Karion, A., Miller, J., Sweeney, C. and White, J.: AMAP Assessment: Methane as an Arctic climate forcer: Chapter 6 : Long-term monitoring of atmospheric methane., Oslo., 2015.

Yamamoto-Kawai, M., Carmack, E. and McLaughlin, F.: Nitrogen balance and Arctic throughflow, Nature, 443(7107), 43, doi:10.1038/443043a, 2006.

Yang, S., Chang, B., Warner, M., Weber, T., Bourbonnais, A., Santoro, A., Kock, A., Sonnerup,

R., Bullister, J., Wilson, S. and Bianchi, D.: Global reconstruction reduces the uncertainty of oceanic nitrous oxide emissions and reveals a vigorous seasonal cycle, Proc. Natl. Acad. Sci., 117, 201921914, doi:10.1073/pnas.1921914117, 2020.

Zitomer, D. H. and Shrout, J. D.: Feasibility and benefits of methanogenesis under oxygen-limited conditions, Waste Manag., 18(2), 107–116, doi:https://doi.org/10.1016/S0956-053X(98)00008-7, 1998.

A) Appendix

Table 3: Concentration of dissolved CH_4 [nmol/kg] with respective standard deviation [nmol/kg], coefficient of variation, station no., coordinates [DD], date of sampling, depth [m].

Station [#]	Latitude [DD]	Longitude [DD]	Date	Depth [m]	Dissolved CH_4 [nmol/kg]	Standard Deviation $CH_{4\_diss.}$ [nmol/kg]	Coefficient of Variation
2	63.36660	-40.81712	27.07.2019	161.66	9.30	1.83	0.20
2	63.36660	-40.81712	27.07.2019	154.6	66.85	0.43	0.01
2	63.36660	-40.81712	27.07.2019	138.83	26.82	0.04	0.00
2	63.36660	-40.81712	27.07.2019	130.29	11.39	1.92	0.17
2	63.36660	-40.81712	27.07.2019	107.26	36.08	32.09	0.89
2	63.36660	-40.81712	27.07.2019	88.25	25.09	8.60	0.34
2	63.36660	-40.81712	27.07.2019	68.21	21.69	4.68	0.22
2	63.36660	-40.81712	27.07.2019	47.67	12.05	6.33	0.53
2	63.36660	-40.81712	27.07.2019	38.74	13.05	1.71	0.13
2	63.36660	-40.81712	27.07.2019	24.87	12.43	2.24	0.18
6	63.14960	-40.12627	27.07.2019	379.63	6.59	1.15	0.17
6	63.14960	-40.12627	27.07.2019	352.19	7.38	1.74	0.24
6	63.14960	-40.12627	27.07.2019	293.77	1.84	NaN	NaN
6	63.14960	-40.12627	27.07.2019	193.98	3.24	0.32	0.10
6	63.14960	-40.12627	27.07.2019	126.12	4.83	0.28	0.06
6	63.14960	-40.12627	27.07.2019	96.96	1.77	0.82	0.46
6	63.14960	-40.12627	27.07.2019	66.51	4.45	1.22	0.27
6	63.14960	-40.12627	27.07.2019	37.03	2.37	0.88	0.37
6	63.14960	-40.12627	27.07.2019	16.97	11.86	0.37	0.03
6	63.14960	-40.12627	27.07.2019	10.68	4.07	0.50	0.12
19	61.41638	-34.59985	29.07.2019	2944.31	5.98	5.22	0.87
19	61.41638	-34.59985	29.07.2019	2908.98	2.69	2.17	0.80
19	61.41638	-34.59985	29.07.2019	1381.52	6.39	1.68	0.26
19	61.41638	-34.59985	29.07.2019	690.46	2.73	2.73	1.00
19	61.41638	-34.59985	29.07.2019	195.25	3.02	0.20	0.07
19	61.41638	-34.59985	29.07.2019	97.07	0.46	0.38	0.83
19	61.41638	-34.59985	29.07.2019	41.57	1.56	0.33	0.21
19	61.41638	-34.59985	29.07.2019	18.14	2.22	0.48	0.22
19	61.41638	-34.59985	29.07.2019	9.94	1.02	0.64	0.62
21	63.83288	-31.00025	29.07.2019	2687.03	0.58	NaN	NaN
21	63.83288	-31.00025	29.07.2019	2678.21	0.93	NaN	NaN
21	63.83288	-31.00025	29.07.2019	1183.28	0.14	NaN	NaN
21	63.83288	-31.00025	29.07.2019	439.29	0.42	NaN	NaN
21	63.83288	-31.00025	29.07.2019	195.81	0.59	NaN	NaN
21	63.83288	-31.00025	29.07.2019	97.3	0.76	NaN	NaN
21	63.83288	-31.00025	29.07.2019	46.69	0.30	0.25	0.84
21	63.83288	-31.00025	29.07.2019	26.78	0.54	0.04	0.08
21	63.83288	-31.00025	29.07.2019	12.25	0.51	0.33	0.65

30	65.34942	-33.12427	30.07.2019	608.16	1.30	NaN	NaN
30	65.34942	-33.12427	30.07.2019	589.27	8.38	1.31	0.16
30	65.34942	-33.12427	30.07.2019	413.72	3.35	0.86	0.26
30	65.34942	-33.12427	30.07.2019	296.04	2.09	1.68	0.81
30	65.34942	-33.12427	30.07.2019	196.41	2.55	1.47	0.58
30	65.34942	-33.12427	30.07.2019	97.77	3.89	1.23	0.32
30	65.34942	-33.12427	30.07.2019	70.61	5.41	3.06	0.57
30	65.34942	-33.12427	30.07.2019	43.32	2.01	0.86	0.43
30	65.34942	-33.12427	30.07.2019	23.04	3.48	0.15	0.04
30	65.34942	-33.12427	30.07.2019	8.15	12.34	3.40	0.28
39	66.33338	-34.50218	31.07.2019	284.1	4.30	NaN	NaN
39	66.33338	-34.50218	31.07.2019	266.84	0.83	NaN	NaN
39	66.33338	-34.50218	31.07.2019	244.75	0.48	NaN	NaN
39	66.33338	-34.50218	31.07.2019	96.56	0.38	NaN	NaN
39	66.33338	-34.50218	31.07.2019	42.06	1.84	NaN	NaN
39	66.33338	-34.50218	31.07.2019	23.83	4.52	0.76	0.17
39	66.33338	-34.50218	31.07.2019	6.94	2.90	0.18	0.06
41	68.68307	-26.29225	01.08.2019	88.84	6.31	4.54	0.72
41	68.68307	-26.29225	01.08.2019	78.36	3.52	0.29	0.08
41	68.68307	-26.29225	01.08.2019	68.64	4.98	0.84	0.17
41	68.68307	-26.29225	01.08.2019	58.92	7.70	2.20	0.29
41	68.68307	-26.29225	01.08.2019	48.52	11.10	1.20	0.11
41	68.68307	-26.29225	01.08.2019	38.3	10.96	1.30	0.12
41	68.68307	-26.29225	01.08.2019	28.75	10.06	0.15	0.02
41	68.68307	-26.29225	01.08.2019	21.68	6.64	1.03	0.15
41	68.68307	-26.29225	01.08.2019	18.04	6.66	0.79	0.12
41	68.68307	-26.29225	01.08.2019	8.1	5.50	0.72	0.13
48	68.26213	-25.36137	01.08.2019	333.97	5.33	0.71	0.13
48	68.26213	-25.36137	01.08.2019	324.58	5.69	0.50	0.09
48	68.26213	-25.36137	01.08.2019	295.32	6.17	0.74	0.12
48	68.26213	-25.36137	01.08.2019	217.24	6.52	0.47	0.07
48	68.26213	-25.36137	01.08.2019	146.07	5.43	0.51	0.09
48	68.26213	-25.36137	01.08.2019	108.46	1.86	0.28	0.15
48	68.26213	-25.36137	01.08.2019	67.14	1.44	0.00	0.00
48	68.26213	-25.36137	01.08.2019	46.91	4.62	0.50	0.11
48	68.26213	-25.36137	01.08.2019	17.97	3.87	0.45	0.12
48	68.26213	-25.36137	01.08.2019	11.12	1.45	0.20	0.13
63	66.87493	-23.28378	02.08.2019	97.34	1.18	1.64	1.39
63	66.87493	-23.28378	02.08.2019	68.05	1.19	1.06	0.89
63	66.87493	-23.28378	02.08.2019	37.66	0.14	0.09	0.61
63	66.87493	-23.28378	02.08.2019	17.61	1.60	0.25	0.16
63	66.87493	-23.28378	02.08.2019	8.77	2.23	0.50	0.23
64	68.20003	-18.16568	03.08.2019	575.66	0.64	0.14	0.22
64	68.20003	-18.16568	03.08.2019	563.19	0.82	NaN	NaN
64	68.20003	-18.16568	03.08.2019	491.72	0.45	NaN	NaN

64	68.20003	-18.16568	03.08.2019	392.85	0.09	NaN	NaN
64	68.20003	-18.16568	03.08.2019	294.39	0.01	NaN	NaN
64	68.20003	-18.16568	03.08.2019	194.55	1.68	NaN	NaN
64	68.20003	-18.16568	03.08.2019	123.98	0.08	NaN	NaN
64	68.20003	-18.16568	03.08.2019	46.95	0.22	NaN	NaN
64	68.20003	-18.16568	03.08.2019	26.76	0.73	0.63	0.86
64	68.20003	-18.16568	03.08.2019	11.95	1.09	0.92	0.85
75	69.21927	-20.45188	03.08.2019	294.09	0.66	NaN	NaN
75	69.21927	-20.45188	03.08.2019	175.8	0.37	NaN	NaN
75	69.21927	-20.45188	03.08.2019	106.49	0.32	NaN	NaN
87	69.99987	-22.21727	04.08.2019	143.8	2.50	NaN	NaN
87	69.99987	-22.21727	04.08.2019	133.88	1.23	NaN	NaN
87	69.99987	-22.21727	04.08.2019	73.04	0.01	NaN	NaN
87	69.99987	-22.21727	04.08.2019	54.75	2.94	NaN	NaN
87	69.99987	-22.21727	04.08.2019	17.97	2.87	0.81	0.28
87	69.99987	-22.21727	04.08.2019	8.14	5.69	0.78	0.14
90	70.33328	-21.29758	04.08.2019	275.02	3.82	NaN	NaN
90	70.33328	-21.29758	04.08.2019	116.29	0.72	0.03	0.04
90	70.33328	-21.29758	04.08.2019	35.99	0.44	0.15	0.35
90	70.33328	-21.29758	04.08.2019	11.73	0.59	0.28	0.48
91	71.14968	-21.60460	04.08.2019	74.39	0.47	0.21	0.45
91	71.14968	-21.60460	04.08.2019	67.94	0.37	0.10	0.27
91	71.14968	-21.60460	04.08.2019	58.93	0.95	0.19	0.20
91	71.14968	-21.60460	04.08.2019	48.3	1.28	0.34	0.27
91	71.14968	-21.60460	04.08.2019	34.5	1.94	1.42	0.73
91	71.14968	-21.60460	04.08.2019	18.33	1.58	0.31	0.20
91	71.14968	-21.60460	04.08.2019	11.37	2.13	0.18	0.09
99	71.12763	-19.35463	05.08.2019	195.44	2.43	NaN	NaN
99	71.12763	-19.35463	05.08.2019	93.38	1.36	0.29	0.21
99	71.12763	-19.35463	05.08.2019	39.16	0.53	0.21	0.39
99	71.12763	-19.35463	05.08.2019	18.25	3.29	0.79	0.24
99	71.12763	-19.35463	05.08.2019	8.27	4.16	1.38	0.33
114	71.06918	-13.43353	06.08.2019	541	0.85	NaN	NaN
114	71.06918	-13.43353	06.08.2019	195.39	1.29	NaN	NaN
114	71.06918	-13.43353	06.08.2019	38.11	1.52	NaN	NaN
128	72.33140	-17.80087	07.08.2019	441.17	0.24	NaN	NaN
128	72.33140	-17.80087	07.08.2019	313.86	0.61	0.56	0.92
128	72.33140	-17.80087	07.08.2019	194.38	1.32	0.49	0.37
128	72.33140	-17.80087	07.08.2019	97.13	0.89	0.29	0.32
128	72.33140	-17.80087	07.08.2019	47.92	1.45	0.12	0.08
128	72.33140	-17.80087	07.08.2019	29.56	3.08	1.53	0.50
128	72.33140	-17.80087	07.08.2019	11.65	3.72	3.64	0.98
140	72.81520	-21.28740	08.08.2019	272.79	0.22	0.15	0.68
140	72.81520	-21.28740	08.08.2019	263.14	1.22	0.10	0.08
140	72.81520	-21.28740	08.08.2019	246.24	0.37	0.04	0.12

140	72.81520	-21.28740	08.08.2019	197	0.68	0.02	0.03
140	72.81520	-21.28740	08.08.2019	146.66	2.29	0.12	0.05
140	72.81520	-21.28740	08.08.2019	97.38	2.23	0.26	0.12
140	72.81520	-21.28740	08.08.2019	67.24	3.50	0.12	0.03
140	72.81520	-21.28740	08.08.2019	47.84	3.44	0.17	0.05
140	72.81520	-21.28740	08.08.2019	28.92	3.52	0.13	0.04
140	72.81520	-21.28740	08.08.2019	8.69	6.17	0.01	0.00
143	74.18317	-19.25118	08.08.2019	197.65	4.08	NaN	NaN
143	74.18317	-19.25118	08.08.2019	67.11	0.97	0.52	0.54
143	74.18317	-19.25118	08.08.2019	47.69	2.31	0.48	0.21
143	74.18317	-19.25118	08.08.2019	28.53	3.99	0.16	0.04
143	74.18317	-19.25118	08.08.2019	11.12	4.83	0.40	0.08
154	73.84978	-15.91790	09.08.2019	155.82	1.15	0.17	0.14
154	73.84978	-15.91790	09.08.2019	127.21	1.64	0.02	0.01
154	73.84978	-15.91790	09.08.2019	96.99	2.25	0.22	0.10
154	73.84978	-15.91790	09.08.2019	72.42	2.15	0.55	0.26
154	73.84978	-15.91790	09.08.2019	52.31	3.08	0.40	0.13
154	73.84978	-15.91790	09.08.2019	34.57	2.83	0.37	0.13
154	73.84978	-15.91790	09.08.2019	11.72	3.07	0.27	0.09
166	77.49848	-5.02977	11.08.2019	1139.61	0.80	0.20	0.26
166	77.49848	-5.02977	11.08.2019	1127.32	1.40	0.29	0.21
166	77.49848	-5.02977	11.08.2019	737.48	1.49	0.33	0.22
166	77.49848	-5.02977	11.08.2019	488.94	0.95	1.06	1.11
166	77.49848	-5.02977	11.08.2019	243.9	2.23	2.71	1.22
166	77.49848	-5.02977	11.08.2019	97.31	4.79	NaN	NaN
166	77.49848	-5.02977	11.08.2019	67.71	2.48	0.64	0.26
166	77.49848	-5.02977	11.08.2019	38.03	2.38	0.42	0.18
166	77.49848	-5.02977	11.08.2019	18.3	2.31	0.51	0.22
166	77.49848	-5.02977	11.08.2019	7.38	3.74	0.28	0.07
168	77.49950	-4.64570	11.08.2019	1436.73	0.38	NaN	NaN
168	77.49950	-4.64570	11.08.2019	1423.52	0.83	0.85	1.02
168	77.49950	-4.64570	11.08.2019	983.51	0.94	0.87	0.92
168	77.49950	-4.64570	11.08.2019	687.88	0.55	0.16	0.30
168	77.49950	-4.64570	11.08.2019	490.13	0.62	0.20	0.32
168	77.49950	-4.64570	11.08.2019	292.98	1.23	0.05	0.04
168	77.49950	-4.64570	11.08.2019	97.22	2.47	NaN	NaN
168	77.49950	-4.64570	11.08.2019	52.26	2.97	0.02	0.01
168	77.49950	-4.64570	11.08.2019	33.37	2.73	0.83	0.30
168	77.49950	-4.64570	11.08.2019	12.14	3.93	1.35	0.34

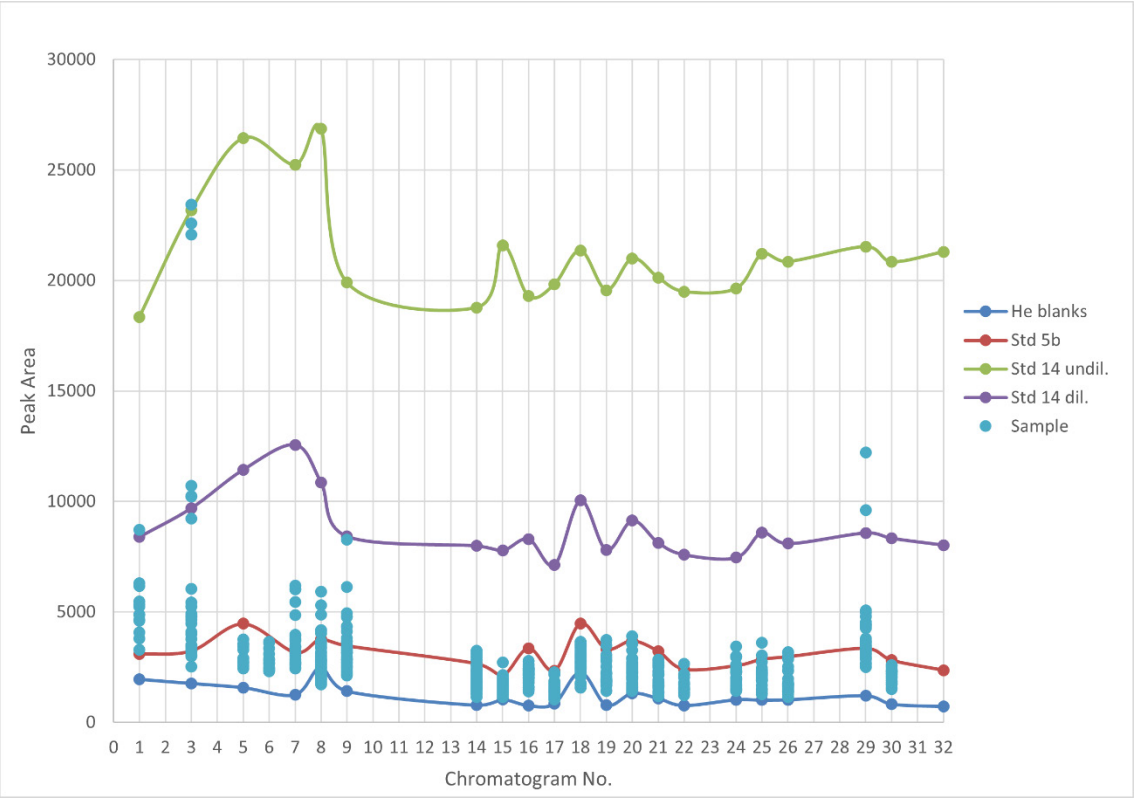

Figure 26: Peak area of helium blanks, internal standard 5b, standard 14 undiluted, standard 14 diluted as well as the measured samples, respectively, for each chromatogram. This displays the variability between each measurement day.

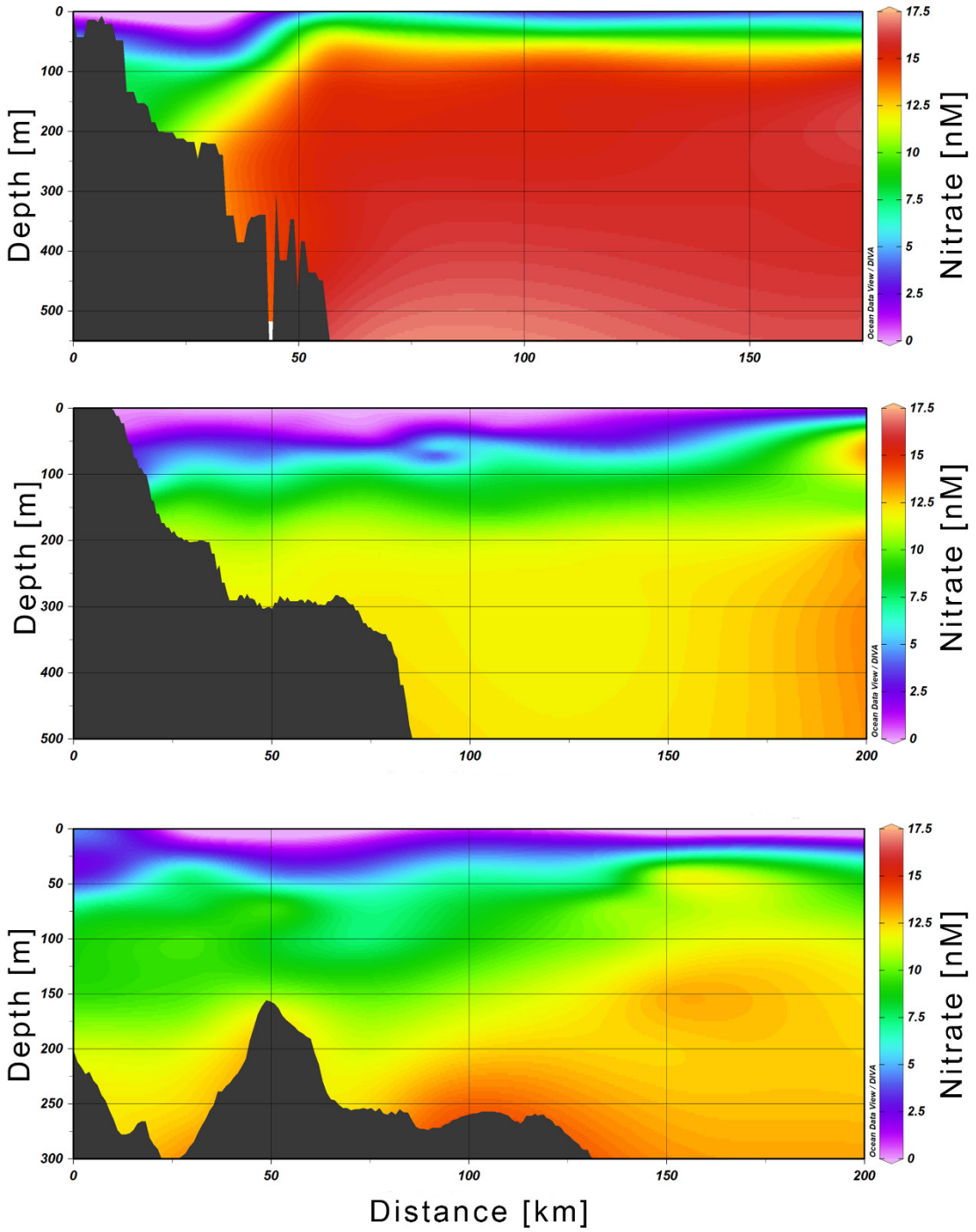

Figure 27: Distribution of nitrate [nM] on the EGS. Order from south to north. **Top**: transect A, **middle**: transect C, **bottom**: transect F.

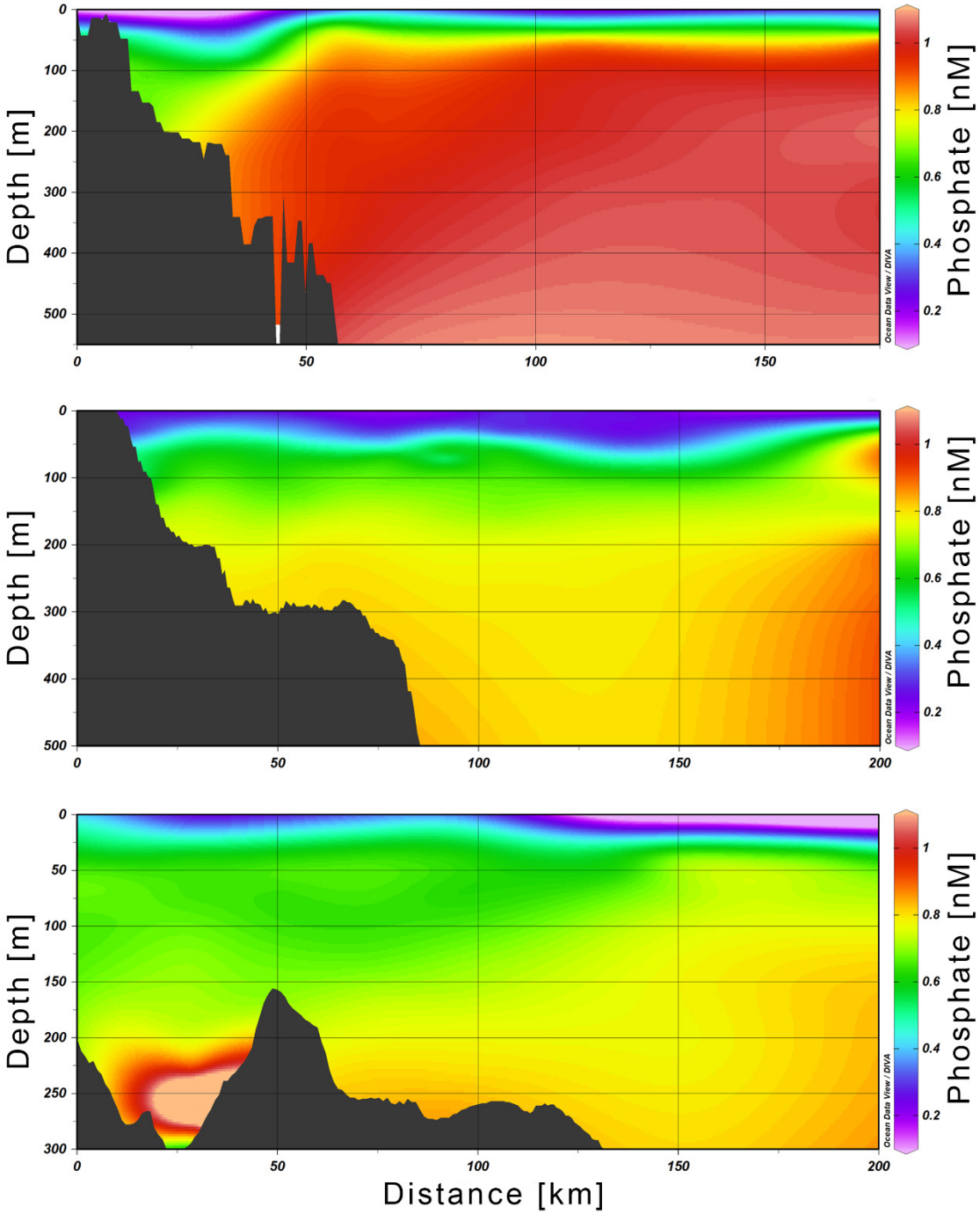

Figure 28: Distribution of phosphate [nM] on the EGS. Order from south to north. **Top**: transect A, **middle**: transect C, **bottom**: transect F.

Declaration/ Erklärung

Hiermit erkläre ich, Daniel Bastian, dass ich die vorliegende Arbeit selbständig und ohne fremde Hilfe angefertigt und keine anderen als die angegebenen Quellen und Hilfsmittel verwendet habe. Die eingereichte schriftliche Fassung der Arbeit entspricht der auf dem elektronischen Speichermedium. (Name der Datei: Bastian_1018959_MScGeow)

Weiterhin versichere ich, dass diese Arbeit noch nicht als Abschlussarbeit an anderer Stelle vorgelegen hat.

Kiel, den 21.05.2021